ADVERTIMENT. La consulta d'aquesta tesi queda condicionada a l'acceptació de les següents condicions d'ús: La difusió d'aquesta tesi per mitjà del servei TDX (www.tesisenxarxa.net) ha estat autoritzada pels titulars dels drets de propietat intel·lectual únicament per a usos privats emmarcats en activitats d'investigació i docència. No s'autoritza la seva reproducció amb finalitats de lucre ni la seva difusió i posada a disposició des d'un lloc aliè al servei TDX. No s'autoritza la presentació del seu contingut en una finestra o marc aliè a TDX (framing). Aquesta reserva de drets afecta tant al resum de presentació de la tesi com als seus continguts. En la utilització o cita de parts de la tesi és obligat indicar el nom de la persona autora.

ADVERTENCIA. La consulta de esta tesis queda condicionada a la aceptación de las siguientes condiciones de uso: La difusión de esta tesis por medio del servicio TDR (www.tesisenred.net) ha sido autorizada por los titulares de los derechos de propiedad intelectual únicamente para usos privados enmarcados en actividades de investigación y docencia. No se autoriza su reproducción con finalidades de lucro ni su difusión y puesta a disposición desde un sitio ajeno al servicio TDR. No se autoriza la presentación de su contenido en una ventana o marco ajeno a TDR (framing). Esta reserva de derechos afecta tanto al resumen de presentación de la tesis como a sus contenidos. En la utilización o cita de partes de la tesis es obligado indicar el nombre de la persona autora.

WARNING. On having consulted this thesis you're accepting the following use conditions: Spreading this thesis by the TDX (www.tesisenxarxa.net) service has been authorized by the titular of the intellectual property rights only for private uses placed in investigation and teaching activities. Reproduction with lucrative aims is not authorized neither its spreading and availability from a site foreign to the TDX service. Introducing its content in a window or frame foreign to the TDX service is not authorized (framing). This rights affect to the presentation summary of the thesis as well as to its contents. In the using or citation of parts of the thesis it's obliged to indicate the name of the author

Three-dimensional numerical simulation of fluid flow and heat transfer in fin-and-tube heat exchangers at different flow regimes

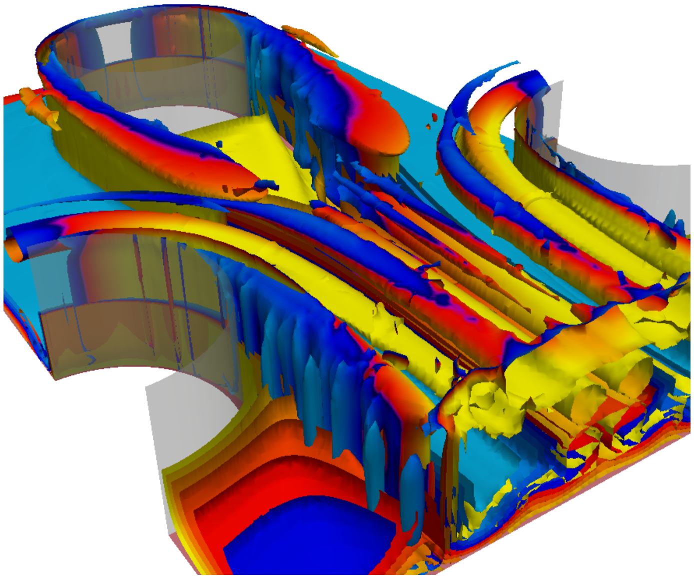

Centre Tecnològic de Transferència de Calor
Departament de Màquines i Motors Tèrmics
Universitat Politècnica de Catalunya

Leslye Paniagua Sánchez
Doctoral Thesis

Three-dimensional numerical simulation of fluid flow and heat transfer in fin-and-tube heat exchangers at different flow regimes

Leslye Paniagua Sánchez

TESIS DOCTORAL

presentada al

Departament de Màquines i Motors Tèrmics
E.T.S.E.I.A.T.
Universitat Politècnica de Catalunya

para la obtención del grado de

Doctor por la Universitat Politècnica de Catalunya

Terrassa, July, 2014

Three-dimensional numerical simulation of fluid flow and heat transfer in fin-and-tube heat exchangers at different flow regimes

Leslye Paniagua Sánchez

Directores de la Tesis

Dr. Assensi Oliva Llena
Dr. Carles Oliet Casasayas
Dr. Oriol Lehmkuhl Barba

Tribunal Calificador

Dr. José Manuel Pinazo Ojer
Universitat Politècnica de València
Dr. Joaquim Rigola Serrano
Universitat Politècnica de Catalunya
Dr. José Fernández Seara
Universidad de Vigo

A mis padres,

a mi hermana y

a mis sobrinos.

Acknowledgements

Quiero iniciar los agradecimientos de mi tesis por quienes son el motor de mi vida y a quienes he dedicado este trabajo: mi familia. A mis padres por su amor y apoyo en todo momento, sé que no fue fácil dejarme ir cuando tomé esta decisión. A pesar de ello, me impulsaron a creer en mí como lo hacen ellos. A mi hermana por ser mi gran amiga incondicional y mi ídolo desde pequeña. Tu cariño ha sido clave especialmente en estos seis años. Gracias familia, por la elasticidad del lazo que nos une, sin vosotros nada de esto habría sido posible.

Profesionalmente, quiero agradecer en primera instancia a Assensi, por brindarme la oportunidad de iniciar este proyecto en el laboratorio trabajando codo a codo con auténticos genios.

Agradezco de manera especial a Oriol, que ha tenido la paciencia suficiente para enseñarme y guiarme en los últimos años del doctorado. Admiro profundamente su capacidad de abstracción y análisis que utiliza para liderar muchos proyectos con ideas novedosas. Ha sido un honor haber tenido a este genio como asesor y maestro.

A Carles, que con su experiencia me ha impulsado a buscar el límite de las herramientas desarrolladas a lo largo de este tiempo para conseguir los mejores resultados. La ambición de este proyecto es en parte, mérito suyo.

Dentro del CTTC he tenido también la oportunidad de trabajar con gente muy talentosa. Agradecer a David por sus consejos y experiencia para el análisis de problemas. A Ivette quien me ha ayudado con el entendimiento de la turbulencia. Al Jordi Chiva que me enseñó a programar desde cero y cuyas lecciones son clave en este proyecto. Joan López por su ayuda con las librerías Nest.

Desde hace poco más de un año (puede que el más duro para cerrar el doctorado) tuve la suerte de conocer de forma personal a mis nuevos compis de oficina. Joan y Xavi, gracias por aprender a entenderme y por animarme en los días más complicados.

Personalmente hice muy buenos amigos a lo largo del doctorado quienes me brindaron apoyo cuando la voluntad flaqueaba. Gracias a los latinos del laboratorio por los buenos momentos que hemos compartido juntos. Chamo, Pedro, Willy, Fede, Lalo y a las chicas: Nea, Sole, Mariana, Fátima por los buenos momentos y recuerdos.

Recientemente adquirí una afición por el deporte, y con ella conocí grandes personas que sin saberlo (o tal vez sí) me ayudaron a desconectar cuando era necesario para retomar fuerza y seguir trabajando. A esos luchadores que me han enseñado con el ejemplo a no rendirse, mil gracias.

Finalmente, tengo la fortuna de contar con amigos y familia esparcidos por el mundo que se han mantenido al pendiente durante estos años aunque nos encontráramos físicamente en contadas ocasiones.

Acknowledgements

A todos vosotros gracias por hacer este viaje más sencillo y divertido. Lo hemos conseguido!

Leslye Paniagua Sánchez

Contents

Abstract

This thesis aims at unifying two distinct branches of work within the Heat Transfer Technological Center (CTTC). On one side, extensive experimental work has been done during the past years by the researchers of the laboratory. This experimental work has been complemented with numerical models for the calculation of fin and tube heat exchangers thermal and fluid dynamic behavior (CHESS and MULTI-CHESS). Such numerical models can be referred to as fast numerical tool which can be used for industrial rating and design purposes. On the other hand, the scientists working at the research center have successfully developed a general purpose multi-physics Computational Fluid Dynamics (CFD) code (TermoFluids). This high performance CFD solver has been extensively used by the co-workers of the group mainly to predict complex flows of great academic interest.

The idea of bringing together this two branches, comes from the necessity of a reliable numerical platform with detailed local data of the flow and heat transfer on diverse heat exchanger applications. Being able to use local heat transfer coefficients as an input on the rating and design tool will lead to affordable and accurate prediction of industrial devices performance, by which the center can propose enhanced alternatives to its industrial partners.

To accomplish these goals, several contributions have been made to the existing TermoFluids software which is in continuous evolution in order to meet the competitive requirements. The most significant problematics to adequately attack this problem are analyzed and quite interesting recommendations are given. Some of the challenging arising issues involve the generation of suitable and affordable meshes, the implementation and validation of three dimensional periodic boundary condition and coupling of different domains (fluid and solid) with important adjustments for the study of cases with different flow physics like time steps and thermal development.

Turbulence is present in most of engineering flows, and fin-and-tube heat exchangers are not an exception. The presence of many tubes (acting like bluff bodies for the flow) arranged in different possible configurations and the fact that the flow is also confined by fins, create complex three dimensional flow features that have usually turbulent or transition to turbulent regime. Therefore, three dimensional turbulent forced convection in a matrix of wall-bounded pins is analyzed. Large Eddy Simulations (LES) are performed in order to assess the performance of three different subgrid-scale (SGS) models, namely WALE, QR and VMS. The Reynolds numbers (Re) of the study were set to 3000, 10000 and 30000. Some of the main results included are the pressure coefficient c_p around the cylinders, the averaged Nusselt number (Nu) at the endwalls and vorticity of the flow.

The final part of the thesis is devoted to study the three dimensional fluid flow and conjugated heat transfer parameters encountered in a flat plate fin and circular tube heat exchangers used in no-frost domestic refrigerators. The numerical code and post-processing tools are validated with a very similar but smaller case of a heat exchanger with two rows of cylindrical tubes at a low Reynolds for which experimental data is available. The next analysis presented is a typical configuration for no-frost evaporators with double fin spacing (for which very few numerical data is reported in the scientific literature). Convective heat transfer in the flow field and heat conduction in the fins are coupled and considered (conjugated approach). The influence of some geometrical and flow regime parameters is analyzed for design purposes. When the flow is considered to be turbulent, WALE SGS model is activated to predict the fluid behavior.

In conclusion, the implementations and general contributions of the present thesis together with the previous existent multi-physics computational code, has proved to be capable to perform successful top edge three dimensional simulations of the flow features and heat transfer mechanisms observed on heat exchanger devices.

Chapter 1

Introduction

1.1 Motivation

Improving thermal engineering devices with the purpose of achieving better performance, reducing the power consumption and in consequence the environmental impact, cutting down the global size and manufacturing costs, is a constant demand for the industry involved in compact heat exchangers applications with energy efficiency constraints.

One common strategy used by the scientists to study complex fluid-dynamics issues is experimentation with physical prototypes. Long time ago, this was actually the only available strategy for development of new devices. However, it requires a very expensive framework because many novel configurations need to be analyzed independently by a new prototype when the reduction of the data is not straightforward. Fortunately nowadays, experimental techniques can be supported by a wide range of effective numerical procedures are affordable and easily available. The increasing computational resources as well as the improvement of mathematical and numerical algorithms have revolutionized the research techniques on different fields, particularly the one we are interested in is the fluid dynamics and heat transfer problems. The continuous progress of the Computational Fluid Dynamics approach enables the study of many different configurations in a wide variety of opportunities.

Heat exchanger design, optimization and performance studies are essential for the heating, ventilation, air conditioning and refrigeration (HVAC&R) systems. Due to the growing concern in ecological matters, it is important that these devices meet the efficiency standards with low costs and environmental impact. In compact heat exchangers, the thermal resistance on the external side (when cooled/heated by a fluid in gaseous state, usually air) can take up to 80% of the total thermal resistance because of the poor thermal properties of gases like air. Attempting to increase the heat transfer on the external side of the heat exchanger, high efficiency extended surfaces (fins) are employed. Hence, the external side (or air side) heat transfer surface area can be as much as 10 times larger than the internal side (or water side). Due to the great surface used on the air side, any improvement on this region can significantly improve the overall performance of the heat exchanger.

Fin and tube heat exchangers are widely used in many commercial applications, namely vehicle radiators, air conditioning systems, air heaters, power stations, chemical and process industries, among others. Numerous experimental and numerical studies have been carried out to analyze the air side heat transfer performance, the strong interest on these equipments is partly due to their close relevance to industrial applications and partly from the enriched physics included in the flow pattern. The combination of such practical relevance and academic meaning of this kind of problems is one of the main motivations of the present doctoral thesis.

Many diverse geometrical parameters (fin length, fin pitch, tube pitch, tube diameter, etc.) can be modified when studying compact heat exchangers. Because of the large number of possible configurations, prototype experimental studies are costly and time consuming for design purposes. Therefore, numerical analysis are a good option to support the available experimental information to enhance the parametric, design or optimization studies.

Besides, taking into account the broad spectrum of uses that heat exchangers work with, the flow regime and flow features encountered on their study have also several possibilities. Some applications may be under laminar or turbulent conditions inside the entire channel formed on the external side of the heat exchanger. But also it is very frequent to find three different flow regimes on the same device, i.e. the entrance region may present laminar behavior while downstream of the heat exchanger the flow may be fully turbulent and in the middle zone with tubes acting like bluff bodies the moving flow may be under transition. For such a complex flow patterns, numerical studies are a powerful tool for providing relevant information that can be more difficult to quantify with physical experimentation.

1.2 Background

1.2.1 Analytical methods

Only a few decades ago, the computational resources were very limited. The high-end numerical simulations were focused only on theoretical problems, but for real industrial applications like heat exchangers some different modeling tools needed to be developed. We will call this kind of modeling *"low order simulation tools"*. Even in the present time, the total simulation of a real industrial problem is a huge challenge so many hypothesis have to be made.

Heat exchangers design can be based on analytical methods ($\varepsilon - NTU$, $F - \Delta T_{lm}$, etc.), but those methods are strongly restricted by important limitations in their analysis. Many hypothesis have to be assumed in order to simplify the problem, such as steady state flow, uniform heat transfer coefficients, constant thermo-physical properties among others [1]. Although this analytic methods are still frequently used by the thermal engineers for fast rating and design of heat exchangers, those methods are not completely realistic and the majority of applications do not fulfill the hypothesis assumed with the analytic approaches.

Nevertheless, such analytic approaches are a classic treatment for heat exchanger design and optimization analysis. There are two methods commonly adopted for rating and design calculations, namely, the $F - \Delta T_{lm}$ method and the $\varepsilon - NTU$ method [2]. The $F - \Delta T_{lm}$ *method* consists on the evaluation of the true temperature difference over the entire length of the exchanger (since the temperature difference between the fluids varies from section to section). It is usually determined by the logarithmic mean temperature difference for counter flow arrangements and it is corrected by a factor (F) for other arrangements. For a direct calculation of the logarithmic temperature difference and hence the heat transfer rate, a knowledge of the terminal temperatures of the fluids is required. If such data is not all known (rating case), it is necessary to rely on an iterative procedure to obtain a solution.

Manassaldi et al. [3] presented a disjunctive mathematical model for the optimal design of air cooled heat exchangers. They used the $F - \Delta T_{lm}$ method to accomplish the optimization criteria consisting in minimize the total annual cost and operating cost, minimize the heat transfer surface area and the fan power consumption.

The $\varepsilon - NTU$ *method* is more frequently used in heat exchanger rating. The concept of Number of Transfer Units (NTU) was introduced by Nusselt and subsequently developed by Kays and London [1]. The advantage of the $\varepsilon - NTU$ method lies in the fact that ε can be determined as an explicit function of NTU and the heat capacity rate ratio (R). Thus the calculation does not depend on the terminal temperatures. Nowadays, numerical effort on this topic is focused also on the correct consideration of $\varepsilon - NTU$ relations. Navarro and Cabezas-Gómez [4] presented a mathematical model for cross flow heat exchangers with complex flow arrangements for determining $\varepsilon - NTU$ relations. Their model is based on the tube element approach, according to which the heat exchanger outlet temperatures are obtained by discretizing the coil along the tube fluid path.

1.2.2 Distributed models and Macro discretization

Detailed or distributed models are based on the discretization of heat exchangers into macro control volumes (CV) composed by tube, fin and fluid regions. The governing equations are solved over this macro CV (see Fig. 1.1 [5]). Given the macro scale of the CVs, the modeling scale is much coarser than the physics scale, thus some empirical inputs are needed in order to describe the interaction between solid and

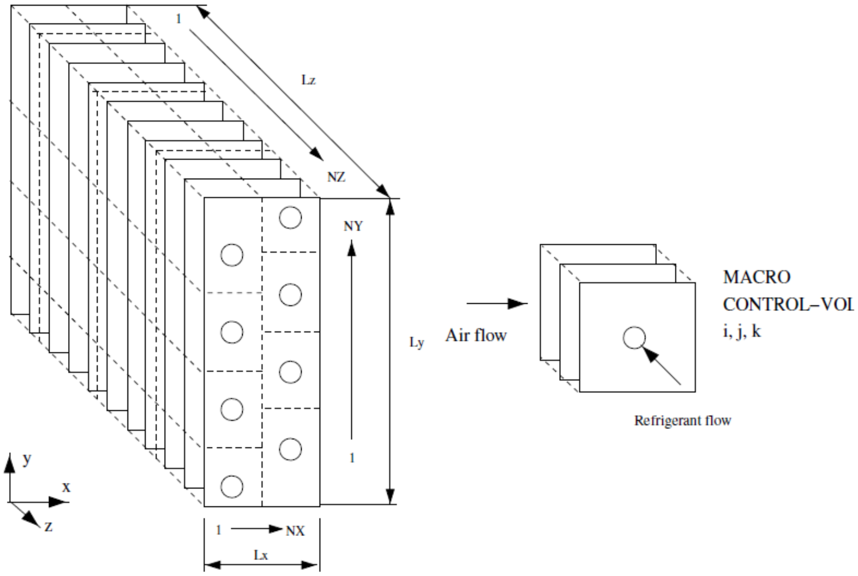

Figure 1.1: Macro discretization strategy for fin and tube heat exchangers [5].

fluid domains [6]. Despite the local hypothetical assumptions that need to be considered, these models are more general and flexible for rating and design purposes than the analytical methods.

An alternative approach to run CFD on heat exchangers is to consider the thermal equipment as a porous media with characteristic thermal and fluid dynamic parameters that summarize the heat exchanger behavior, thus avoiding the simulation of the small geometrical details found in the finned surfaces [5].

Teruel and Uddin [7] developed a new model to describe turbulent flows within the porous media approximation. They tied together and treated as a single quantity the spatial and time fluctuations. This novel treatment of the fluctuations leads according to them to a natural construction of the $k-\varepsilon$ type equations for rigid and isotropic porous media in which all the kinetic energy filtered in the averaging process is being modeled. Their model is closed by assuming the eddy viscosity approximation and using simple models to represent the interaction between the walls in the porous media and the fluid.

Extensive previous work has been done at the Heat Transfer Technological Center (CTTC) to provide the analysis of heat exchanger systems. Particularly, three numerical tools have been developed and carefully validated. The first one is the detailed heat exchanger design code, named by the acronym *CHESS* (Compact Heat Exchanger Simulation Software), conceived for the detailed analysis of fin and tube heat exchangers with the maximum level of detail in all the geometrical and phenomenological situations. This tool is specially appropriate where a heat exchanger is to be optimized and known in detail: a complete 3D map of the heat exchanger is provided in both fluids and the solid elements [8, 9].

For situations where quick rating and design code is needed, and for applications with almost uniform heat transfer coefficient throughout the heat exchanger, a second numerical code based on $\varepsilon - NTU$ procedures was developed. This numerical tool, named *quickCHESS*, was primarily designed for HVAC&R air-liquid applications with dry or wet finned surfaces [9].

Finally, for a simplified analysis of the coils interaction in multiple heat exchanger situations (engine cooling modules, air-handling units), a third numerical code (called *multiCHESS*) was developed. It is capable to model the main flow paths (air and refrigerant) through the thermal system and couple the *CHESS* simulation of the different heat exchangers [10].

1.2.3 CFD techniques

The majority of the flows found in nature and engineering applications are partly or fully turbulent. They are characterized by sudden fluctuations in space and do not present constant behavior with time. Some examples of such flows include the motion of the clouds, the flow over the wing of an aircraft or over a F1 car, the smoke from a cigarette, etc. It is the implicit randomness and complexity of turbulent flows which make it to be an intellectual challenge for many scientists and engineering researchers. In the present time, with the growing computational power capacity and advanced experimental techniques many effort has been focused on the understanding of turbulence.

Leonardo da Vinci on 1513, observed and illustrated turbulent flow in the famous sketch named *"Old Man with Water Studies"* (Fig. 1.2). But it was until 1883 when the first experiment for the visualization of a flow developing from laminar to turbulent motion was carried out by Osborne Reynolds.

Many years have passed and countless studies have been reported by using different methods to predict turbulent (and laminar) flows. Although the phenomena of turbulent flows vary from one to another, the governing equations that describe the motion of Newtonian fluids are the same. These equations are the so-called Navier-Stokes equations. The full differential equation system (together with the continuity equation) is non linear and time dependent. It is a very complex math-

Figure 1.2: Sketch of *"Old Man with Water Studies"* from Leonardo da Vinci.

ematical system which is usually solved by using approximate numerical solutions with the support of modern computers.

For solving turbulence, different alternatives can be included on the governing differential equation system. The most common approach used in commercial codes is the Reynolds-averaged Navier-Stokes (RANS) equations. This alternative gives time averaged solutions to the Navier-Stokes equations with different models, i.e. $k - \omega$, $k - \varepsilon$ or hybrid $k - \omega / k - \varepsilon$. One step forward, the next numerical alternative which usually increase the accuracy of the results respect to RANS is the so-called Large Eddy Simulation (LES) technique. This option, solves the transient equations averaging in space, hence, not all the turbulence scales are solved. The large scales that contain most of the energy of the flow and dominate the transport phenomena are simulated, while the smallest scales (much smaller than the order of the geometry under study) that are responsible of the energy dissipation will be modeled with a sub-grid scale (SGS) model. The general performance of a LES solution then depends on the chosen SGS model if the grid is good enough to resolve the relevant physics on the largest scales. Finally, the most accurate alternative to solve turbulence is the Direct Numerical Simulation (DNS) that provides three dimensional, time dependent numerical solutions to the Navier-Stokes equations. Since the equations are supposed to be solved directly by numerical approximations (without the necessity of using any turbulence model), the possible errors would come only from the domain truncation [11].

Of course, because of its inherent accuracy DNS would be the most desired alternative to predict turbulent flows. However, the main limitation of DNS is that it requires a huge amount of computational resources and this demand increases rapidly with Reynolds number (roughly proportional to $Re^{11/4}$ [12]). Whereas DNS is at the moment restricted to low-to-moderate Reynolds numbers and relatively simple geometries, LES becomes a good alternative to look for sufficiently accurate results in different kind of more complex flows [13] and it is one of the main objectives that the present thesis is intended to accomplish.

Inside the CTTC, researchers are focused on different aspects like mathematical formulation, numerical resolution and experimental validation of fluid dynamics and heat and mass transfer phenomena. The numerical background acquired by the group is very important and diverse, for example, numerical simulation of turbulent flow around bluff bodies using LES has been performed using the in-house TermoFluids software [14, 15].

1.3 High-end simulations for industrial applications

In general, the less demanding alternative for numerical simulation of turbulence i.e. RANS, has been mostly used for some industrial problems like condenser or evaporator heat exchangers, air conditioning, cooling systems for electronic equipment components, airfoil for aircraft engines, etc. But this numerical strategy has shown to present some problems in order to illustrate and resolve the complexity of the flow structure like horseshoe vortices, recirculation zones, wakes generated, flow separation and consequent reattachment, among others [16–21].

The three dimensional nature of separated flows in the case of a geometrical confinement generates a complex velocity field manifested by the formation of distinct vortex structures, which are mostly accounted when using LES [22]. Nowadays it is relatively affordable to use the middle level tool for solving turbulence, which is LES. This thesis aims at conjugating this high level simulation tool with industrial applications. The present work has showed acceptable average performance for the industrial objectives, although it has shown some visible limitations on the local measurements [23].

Deep methodical analysis has been needed in order to prevent numerical errors on the simulations. The author found some issues that induced inaccuracy on the results or extra computational costs for the simulations. Geometric definition of the problem, influence of boundary conditions imposed, choosing the adequate mesh strategy for complex geometries, or determining the convenience of dimensional or non dimensional problem approach are some of the most relevant that will be explained later on this thesis (Chapter 2).

1.4 Outline of the thesis

This thesis, aims at studying the fluid-thermal complex phenomena in composed geometries for industrial applications (particularly for refrigeration industry). At the same time, the deep analysis will generate the basis of a numerical platform capable to feed a data base for the CTTC research group and its partners, expanding the know-how of a flexible range of applications from the results obtained with high performance computations (three dimensional, unsteady simulations). The available heat exchanger simulation codes (with distributed and analytic models, i.e. CHESS, quickCHESS and multiCHESS) are dependent on empirical information that up to now was obtained from the literature. This need of external data added some uncertainties to the final result due to the hypothesis made by the authors of the correlations used. Thus, the modeling codes were limited by the availability of information suitable for each case of interest. The insertion of the possibility to perform numerical experiments in order to obtain reliable owned data for a wide range of applications, increases at the same time the capabilities of the previous existing detailed and analytic codes.

At the same time, another important outcome of this thesis is the upgrade implemented to the existing CFD tool, which is now able to simulate particular features of these cases with convoluted geometries and flows. Expanding the know-how of the group on the physical phenomenology of intricate fluxes and advanced heat transfer enhancements.

To accomplish these goals, much effort has been applied on the understanding of the particular suggested problem. The next Chapter (Chapter 2) is focused on presenting in detail the principal numerical issues that needed special attention. Whether because of the physics involved or because it needed new implementations on the used code for the simulations (TermoFluids software). On that Chapter, mesh strategies are defined, the implementation of a new periodic boundary condition is explained, and the algorithm for conjugated heat transfer problems is presented.

The contents of the following Chapter (Chapter 3) have been published on the Numerical Heat Transfer International Journal [23]. It is devoted to study the fluid flow and heat transfer of air passing through a pin fin matrix under turbulent regime. Three different SGS models for LES treatment were considered, and sufficiently good results were obtained even when coarse grids were used.

After, Chapter 4 is intended to study the selected geometry of an industrial evaporator used for no-frost applications. Conjugated heat transfer is studied between the working fluid and the solid fins of the heat exchanger. A very detailed validation analysis for the performance of a plate fin and tube heat exchanger at low Reynolds numbers is examined numerically and compared with available experimental data, showing a good agreement. Careful attention is to be paid on the adequate reduction of the final numerical data. Then, for a specific situation proposed by one industrial partner the more complex geometry for no-frost evaporators generally used on domestic refrigeration, the same numerical approach is applied. Given the intricated geometry and consequent flow physics, when the flow is considered to be turbulent, a selected SGS model was used for the correct simulation of the flow features.

References

[1] W. M. Kays and A. L. London. *Compact Heat Exchangers*. McGraw-Hill, 1984.

[2] H. Y. Wong. *Handbook of Essential Formulae and Data on Heat Transfer for Engineers*. Longman, 1977.

[3] J. I. Manassaldi, N. J. Scenna, and S. F. Mussati. Optimization mathematical model for the detailed design of air cooled heat exchangers. *Energy*, 64:734–746, 2014.

[4] H. A. Navarro and L. C. Cabezas-Gómez. Effectiveness-ntu computation with a mathematical model for cross-flow heat exchangers. *Brazilian Journal of Chemical Engineering*, 24(04):509–521, 2007.

[5] Carles Oliet Casasayas. *Numerical Simulation and Experimental Validation of Fin and Tube Heat Exchangers*. Ph.D. Thesis. Universitat Politécnica de Catalunya (UPC), Terrassa, Barcelona. Spain, 2006.

[6] F. Escanes, C. D. Pérez-Segarra, and A. Oliva. Thermal and fluid-dynamic behaviour of double-pipe condensers and evaporators. *International Journal for Numerical Methods for Heat and FLuid Flow*, 5(9):781–795, 1995.

[7] F. E. Teruel and Uddin R. Macroscopic modeling of turbulence in porous media flows. *Mecánica Computacional*, 27:265–280, 2008.

[8] C. Oliet, C. D. Pérez-Segarra, O. García-Valladares, and A. Oliva. Advanced numerical simulation of compact heat exchangers. Application to automotive, refrigeration and air conditioning industries. *In Proceedings of the Fifth European Congress on Computational Methods in Applied Sciences and Engineering (ECOMASS)*, 2000.

[9] C. Oliet, C. D. Pérez-Segarra, S. Danov, and A. Oliva. Numerical simulation of dehumidifying fin and tube heat exchangers. Model strategies and experimental comparisons. *In Proceedings of the 2002 International Refrigeration Engineering Conference at Purdue*, 2002.

[10] C. Oliet, C. D. Pérez-Segarra, and A. Oliva. Numerical simulation of complex thermal systems involving multiple fin and tube heat exchangers. *In Proceedings of the 2004 International Refrigeration and Air Conditioning Conference at Purdue*, 2004.

[11] Stephen B. Pope. *Turbulent Flows*. Cambridge University Press, 2000.

[12] Ricard Borrell Pol. *Parallel algorithms for Computational Fluid Dynamics on unstructured meshes*. Ph.D. Thesis. Universitat Politécnica de Catalunya (UPC), Terrassa, Barcelona. Spain, 2012.

[13] Oriol Lehmkuhl Barba. *Numerical resolution of turbulent flows on complex geometries*. Ph.D. Thesis. Universitat Politécnica de Catalunya (UPC), Terrassa, Barcelona. Spain, 2012.

[14] O. Lehmkuhl, R. Borrell, I. Rodríguez, C.D. Pérez-Segarra, and A. Oliva. Assessment of the symmetry-preserving regularization model on complex flows using unstructured grids. *Computers & Fluids*, 60:108–116, 2012.

[15] O. Lehmkuhl, R. Borrell, C. D. P'erez-Segarra, J. Chiva, and A. Oliva. Direct Numerical Simulations and Symmetry-Preserving Regularization Simulations of the flow around a circular cylinder at Reynolds number 3900. *Turbulence, Heat and Mass Transfer 6*, 2009.

[16] J. Jang, M. Wu, and W. Chang. Numerical and experimental studies of three-dimensional plate-fin and tube heat exchangers. *International Journal of Heat and Mass Transfer*, 39(14):3057–3066, 1996.

[17] K. Hajalić, M. Popovac, and M. Hadziabdić. A robust near-wall elliptic-relaxation eddy viscosity turbulence model for CFD. *Int. J. Heat Fluid Flow*, 25(6):1047–1051, 2004b.

[18] M. Mon and U. Gross. Numerical study of fin-spacing effects in annular-finned tube heat exchangers. *International Journal of Heat and Mass Transfer*, 47:1953–1964, 2004.

[19] Y. L. He, W. Q. Tao, F. Q. Song, and W. Zhang. Three-dimensional numerical study of heat transfer characteristics of plain fin and tube heat exchangers from view point of field synergy principle. *International Journal of Heat and Fluid Flow*, 26:459–473, 2005.

[20] K. Hanjalić, D. Laurence, M. Popovac, and J.C.M. Uribe. $v^2/k - f$ turbulence model and its application to forced and natural convection. *In: Sixth Int. Sympos. Engineering Turbulence Modelling and Measurements*, pages 493–496, 2005.

[21] G. Delibra, D. Borello, K. Hanjalić, and F. Rispoli. URANS of flow and endwall heat transfer in a pinned passage relevant to gas-turbine blade cooling. *Int. J. Heat Fluid Flow*, 30:549–560, 2009.

[22] I. K. Karathanassis, E. Papanicolaou, V. Belessiotis, and G. C. Bergeles. Three-dimensional flow effects on forced convection heat transfer in a channel with stepwise-varying width. *International Journal of Thermal Sciences*, 67:177–191, 2013.

[23] L. Paniagua, O. Lehmkuhl, C. Oliet, and C. D. Pérez-Segarra. Large Eddy Simulations (LES) on the Flow and Heat Transfer in a Wall-Bounded Pin Matrix. *Numerical Heat Transfer, Part B: Fundamentals: An International Journal of Computation and Methodology*, 65(2):103–128, 2014.

Chapter 2

Numerical background of the thesis

Part of the contents of this chapter have been published as:

Ivette Rodríguez, Oriol Lehmkuhl, Ricard Borrell, Leslye Paniagua, Carlos D. Pérez-Segarra. High Performance Computing of the flow past a circular cylinder at critical and supercritical Reynolds numbers. *Procedia Engineering*, 2013.

Abstract.
The recommended techniques for the most critical stages of the high-end numerical simulation of refrigeration industrial devices like evaporator heat exchangers are presented. Such a complex problem involves geometrical challenges for a typical CFD analysis (suitable mesh configuration, selection and design), as well as optimization requirements to minimize the computational costs of the simulation (reducing the domain using periodic boundary conditions) and finally it demands the simulation of different domains and physics (fluid and solid regions) at the same time. A detailed strategy to address this kind of problems is proposed.

2.1 Introduction

A part of the work done by the author during the past few years has been intended to apply high-end numerical simulations of the flow and heat transfer present in no-frost evaporators (fin and tube heat exchangers). Until now, the Heat Transfer Technological Center (CTTC) has had two major work approaches, i.e. experimentation and development of models to support industrial partners with real applications, and development of high order numerical tools that has been mostly used for academic purposes (or industrial applications of different nature than the one presented on this thesis). The author seeks to combine these two lines of work and assess the capabilities of high order simulation tools when working under less accurate conditions in order to make the simulations achievable for heat exchanger industrial problems.

Another application of the work done within the present thesis is the cooling of turbine blades which shares the main characteristics of geometry with fin and tube heat exchangers but it usually works at higher Reynolds numbers, forcing the approximate solution of the Navier Stokes equations to consider turbulence scales and intensity. Besides the difference in the flow regime, there is no fluid inside the tubes for blade cooling applications. But for the external part of fluid flow (usually in the gas state) and heat transfer mechanisms both usages of heat exchangers require similar approaches.

In no-frost refrigerators, the compartment cooling relies on forced convection heat transfer between the internal air (assisted by a fan) and a tube-fin evaporator, Fig. 2.1 represents an illustrative distribution of the air flow circulation in a household 'no-frost' refrigerator [1].

To exemplify one of the possible configurations that can be found on this kind of equipments, the geometrical and operation conditions of an evaporator are detailed in the following: external diameter of the tubes $D = 8\ mm$, transversal tube pitch $PT = 22.05\ mm$, longitudinal tube pitch $PL = 18.75\ mm$, fin size in the transversal direction $H = 50\ mm$, fin size in the longitudinal direction $W1 = 190.5\ mm$, fin thickness $FT = 0.15\ mm$, fin pitch of the first two rows of the evaporator $FP1 = 10\ mm$, fin pitch of the last eight rows of the evaporator $FP2 = 5\ mm$. The heat exchanger of this particular example is composed of 10 rows of cylindrical tubes in the longitudinal direction and 2 columns in the transversal direction of the flow. In the normal direction, (perpendicular to the fins) the depth of the heat exchanger is $L = 315\ mm$. For this particular application, the inlet velocity can be set in the range $0.25 \leq V_{in} \leq 1.0\ m/s$, the working fluid is usually air entering at an almost constant temperature $T_{in} = -20°C$. A schematic representation of the illustrated geometry is found in Fig. 2.2.

As can be seen in Fig. 2.2, the geometry is quite complex. Having multiple tubes acting like bluff bodies for the air flow, and adding a short fin on the normal direction

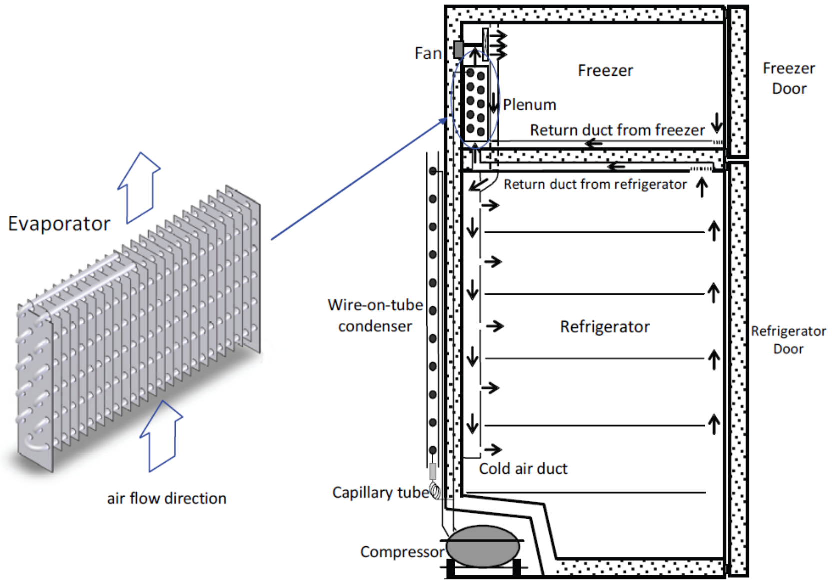

Figure 2.1: Air flow distribution in a household ’no-frost’ refrigerator [1].

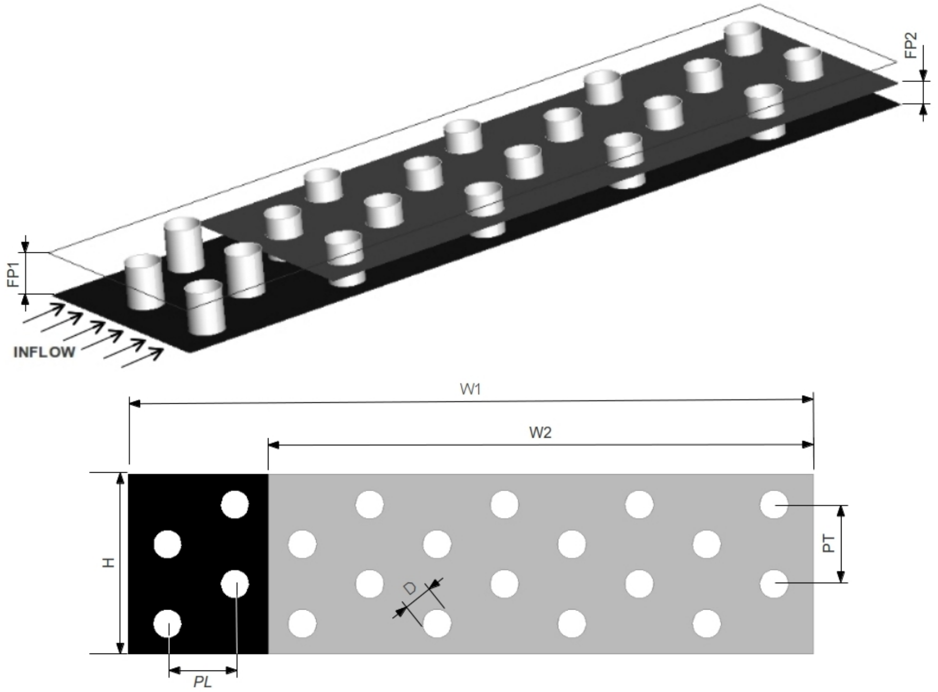

Figure 2.2: Geometry of the baseline evaporator that will be simulated.

to the long fin. The flow is expected to present complex three dimensional features, high mixing and possible laminar, turbulent or in transition regime. Such a complex flow would need high order numerical simulation tools to be adequately predicted.

Within the CTTC, an advanced in-house software called TermoFluids has been developed and improved over the last years [2]. It is a very complete software capable to perform Computational Fluid Dynamics (CFD) simulations for many different applications. Despite the many strengths of the in-house code, there were some particular issues that were taken into account for reaching the goal of the present thesis.

In order to accomplish the final study of a commercial no-frost refrigerator evaporator with a high efficiency numerical approach, some previous stages need to be defined. The problem is challenging and the correct selection of simulation parameters are crucial to identify critical issues and avoid inaccurate results. In the following, the previous numerical stages will be briefly defined and the incoming sections of this chapter will explain in detail the key issues of each stage.

- *MESH DEFINITION*. Different types of mesh can be applied to discretize the computational domain. Each mesh strategy will provide different levels of accuracy, will induce to different costs of time consumption, or will be optimal to better resolve different regions of the domain. For those reasons, it is important to analyze the problem and determine the mesh topology that best fits the needs of this application. Section 2.2 explains the different types of mesh that can be used for this kind of geometries, while Section 2.3 presents the detailed study of the flow between parallel plates and explains the boundary layer development on the most significant geometric characteristics. The conjunction of this two Sections leaded to the conclusion that the best mesh strategy for the final study of heat exchangers would be the multi-block structured type mesh (also known as body fitted mesh) with a special emphasis on the boundary layer mesh design.

- *PERIODIC DOMAIN*. Heat exchangers can be very big geometries and given the convoluted air flow passing through the fins and tubes, proper meshes can be extremely expensive (in computational costs). Based on previous experience and learning from available literature, the flow on the external zone of fin and tube heat exchangers can be considered periodic [3–5]. This is, the flow presents identical behavior on different geometrical regions. Such characteristic allow the computational domain to be significantly reduced to its minimum possible size where the flow is no longer periodic (see Fig. 2.3). Section 2.4 explains the implementations needed to treat periodic domains.

- *CONJUGATED HEAT TRANSFER*. Plate fin and tube heat exchangers are employed in varieties of engineering purposes such as air conditioning units, compressor inter-coolers, automotive radiators, evaporators of refrigerators,

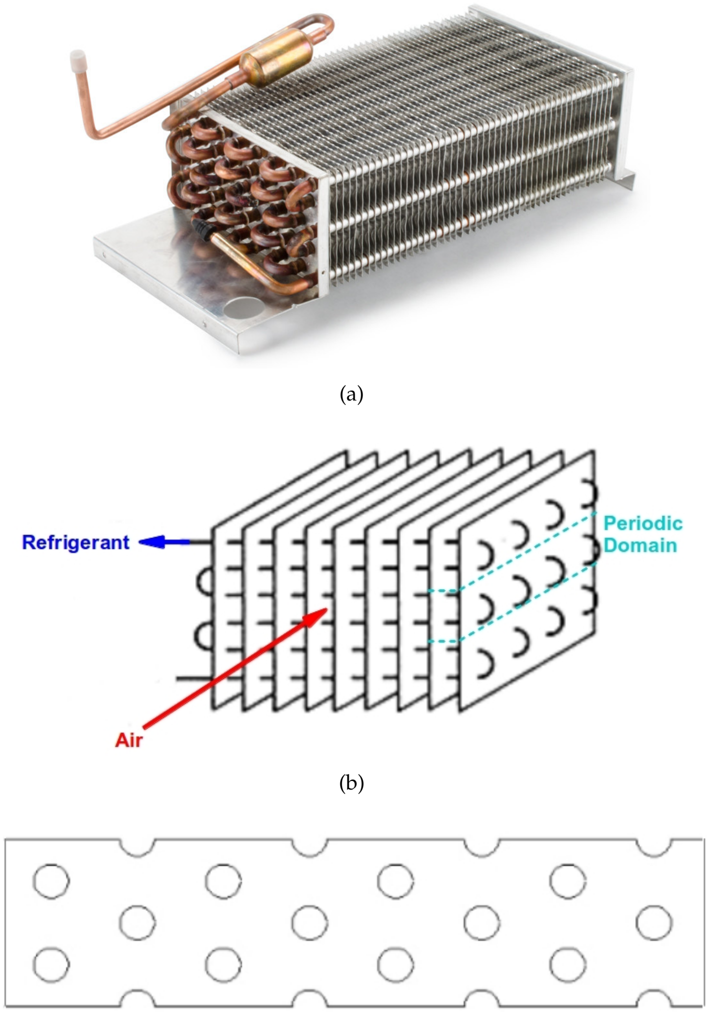

(a)

(b)

(c)

Figure 2.3: Example of a refrigeration heat exchanger (a,b), and the corresponding reduced periodic computational domain (c).

etc. The fin and tube heat exchangers usually consist on expanded round tubes in a set of parallel fins and it can be composed of one or more tube rows in the flow direction. The working fluid passing inside the tubes (refrigerant) exchange energy in the form of heat with the external working fluid (usually on gaseous state and for no-frost usage, air is the gas most frequently used). However, refrigerant and air are never in direct contact between each other, refrigerant is confined by the tubes and air is forced to pass through a fin array in order to increase the available heat transfer surface. In the end, the heat exchanger is composed in great part by solid regions despite the heat transfer is needed on the fluids. Hence, it is important to take into account the heat exchanged between fluid and solid regions. The numerical treatment of different domains needs to be coupled and work efficiently on parallel computers, the explanation of the recommended approach is detailed in Section 2.5.

2.2 Mesh strategies

TermoFluids software applies the Finite Volume Method (FVM) which uses a series of cells (referred to as CV), elements and nodes that conform all together the so called mesh. The fundamental equations of thermofluid dynamics are calculated at the location of each of these nodes. The shape of the cells impacts in great manner the accuracy of the solution of the equations due to discretization errors. Thus, in the first stage of the problem simulation, the design of the mesh and its computation is crucial for the complete process and consequent success of the simulation.

As CFD has developed, better algorithms and more computational power has become available to the fluid dynamics community. By adding new solvers to the disposable tools, the meshing process has increased its possibilities. The most common classification of the meshes are based upon connectivity of a mesh, namely structured and unstructured meshes.

The program used for the generation of the meshes needed for the simulations of this thesis is ANSYS-ICEM CFD which can generate both type of meshes (structured and unstructured). It is important to point out that designing and generating an accurate mesh for complex geometries and/or difficult problems can be quite challenging and time consuming as well. This is because several details must be taken into consideration, i.e. the selection of the appropriate shape of the CVs and its location, is important also to ensure a smooth grow of the CV sizes. Going from sufficiently small size and aspect ratio close to 1 at the boundary layer region to the less critical zones where the mesh should be able to transport energy with an optimal number of CVs. If the CVs are too big at this regions, the simulation will probably lead to divergence or to mistaken results. On the other hand, if the CVs are very small, extra unnecessary computational resources will be expended to obtain the final result.

2.2.1 Structured meshes

A structured mesh is characterized by uniform connectivity between cells that can be expressed as a two or three dimensional array. The elements present on this kind of meshes are quadrilaterals in bi dimensional problems and hexahedra in three dimensional applications. The uniformity of the connectivity of the cells allows the user to conserve space because neighborhood relationships are defined by the storage arrangement (see Fig. 2.4).

Using structured meshes has many advantages on the simulation process. It permits the user to keep high degree of control, i.e. the mesh can be accurately designed to the problem needs. Hexahedral cells are very efficient when the requirements force the domain to be carefully resolved in one unique direction. Also a good adjustment to the body shape can be obtained with this meshes (body fitted meshes, see Fig. 2.5). The grid is usually aligned with the flow which helps the solver to converge faster. Nevertheless, this structured technique has some disadvantages as well. The time consumed in order to generate a good quality mesh is much larger for structured than unstructured meshes. If the geometry is very intricated, structured meshes may not fulfill the requirements of accurate mesh computation.

Structured mesh uses hexahedra shaped elements to create the mesh used for the simulation. With the program ANSYS-ICEM CFD, the user can generate purely structured meshes by using hexahedra blocks and manipulate them by slicing them into a series of smaller blocks, Fig. 2.6 illustrates different splitting options with the multi block technique. Then the blocks allow for the edges of those blocks to be associated to the geometry curves. After wards, mesh parameters and node spacing are defined along the edges in order to define the mesh. Still, the main difficulty with a structured mesh comes from trying to adapt a hexagon shaped element to a curved or complex shape. This can result sometimes in poor quality mesh cells and inaccurate results in consequence.

2.2.2 Unstructured meshes

On the other hand, unstructured meshes are characterized by an irregular connectivity between cells. This mesh can use any kind of element that a solver might be able to use. Compared to structured meshes, the storage requirements for unstructured meshes can be much larger because the neighborhood connectivity needs to be explicitly stored (each node can have different number of neighbors and the geometrical relationship is not conserved, as can be seen in Fig. 2.7).

Of course, unstructured meshes are a good alternative to keep in mind when deciding the grid generation. Some of the many strengths that this strategy may have will be mentioned hereafter. The grid generation program, has automated options for unstructured grid generation which takes much less effort by the user to define

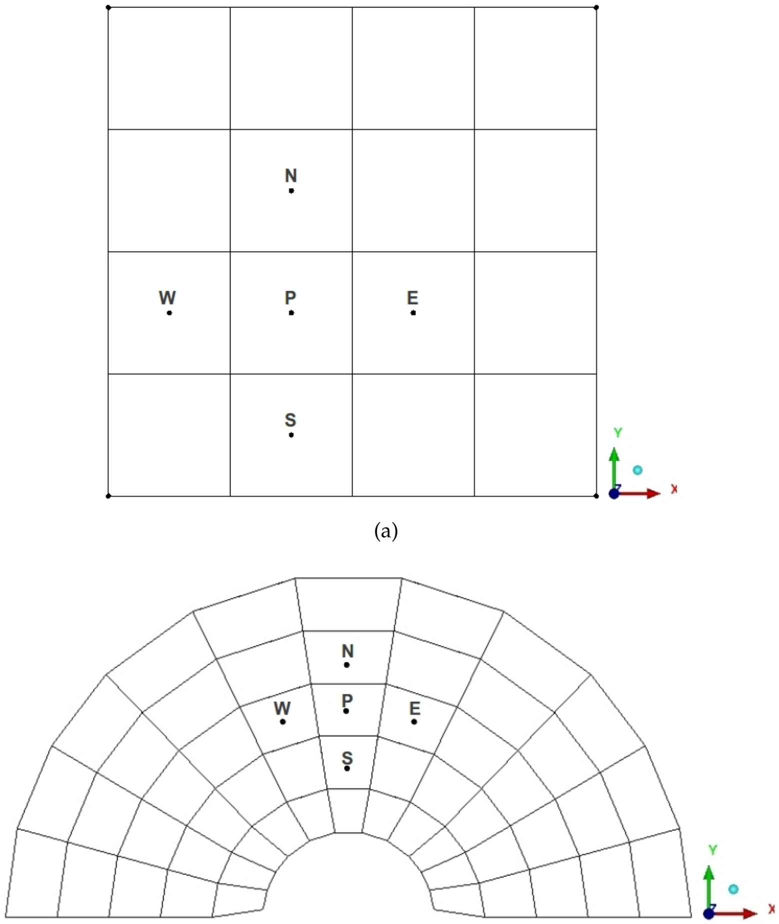

(a)

(b)

Figure 2.4: Known neighborhood relationship between nodes of structured meshes.

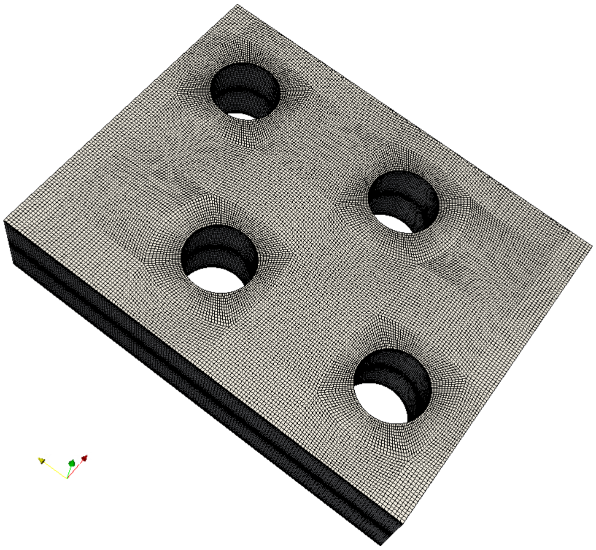

(a)

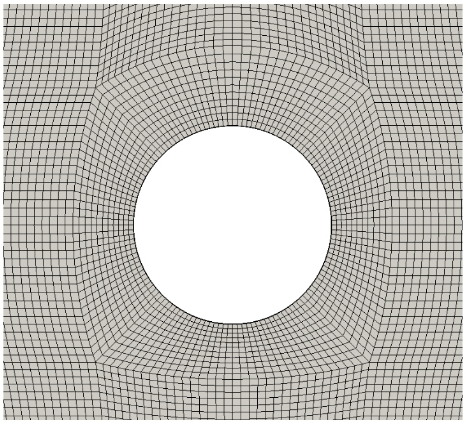

(b)

Figure 2.5: Structured mesh built with the body fitted technique. a) Mesh for a bank of cylinders, b) zoom of the CVs around one cylinder.

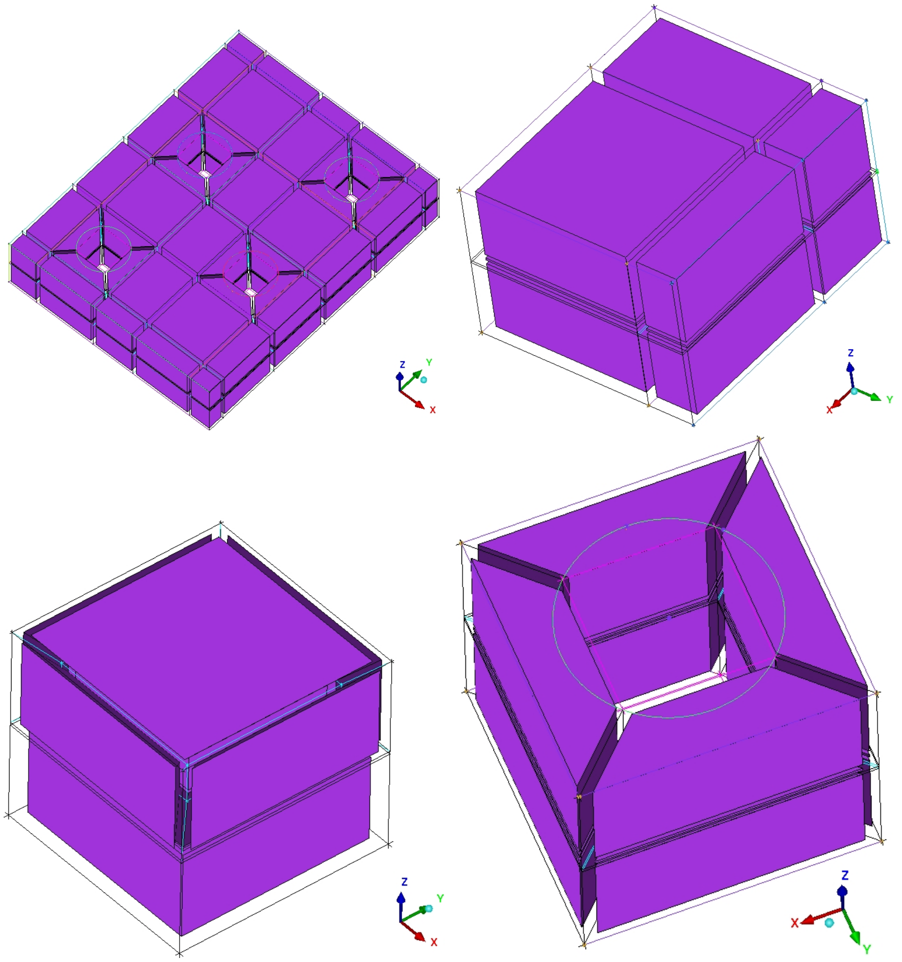

Figure 2.6: Multi block strategy used on the ANCYS-ICEM CFD software for designing structured meshes.

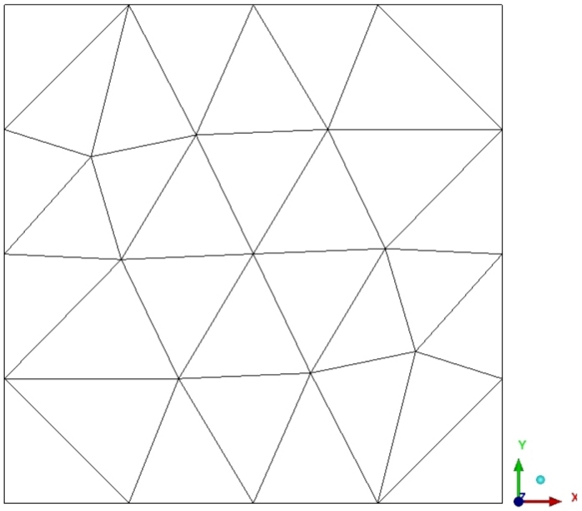

(a)

Figure 2.7: Irregular connectivity between cells of unstructured mesh.

a mesh. Almost any kind of geometry can be suitable for unstructured meshes. The mesh size can be optimized by significantly reducing the quantity of cells on non critical regions of the flow. However, the user may find some trouble to accurately define certain areas of the mesh. Tetrahedral elements do not stretch well, which will drastically impact the accuracy of the results specially on the border of curved surfaces. The post processing stage requires larger computer power.

The program ANSYS-ICEM CFD can create structured and unstructured meshes by defining the mesh parameters along the curves or over the surfaces of the geometry. By using this strategy, the meshes are in concept always unstructured, however the user is capable to decide whether to use triangles or rectangular bi dimensional cells (or even a mixture of both kind, see Section 2.2.3). Triangles are called “TRI”, while rectangular are denoted by “QUAD”. For unstructured meshes, the most typical selected option is the “ALL TRI” for computing the grid elements, which admit only triangular elements on the plane of the bi dimensional mesh. Such meshes shall be extruded in order to obtain the final three dimensional mesh.

Another particular option of unstructured meshes is when clearly defined regions are meshed using ″TRI″ and ″QUAD″ elements with the purpose of carefully adjusting quadrilateral elements to curved surfaces and obtaining the advantages of

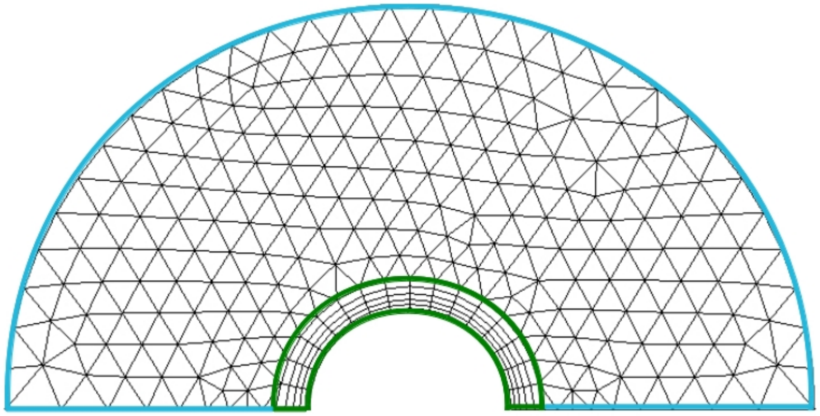

Figure 2.8: Bi dimensional unstructured mesh with structured region around the cylinder (limited by the green lines) and unstructured grid on the external zone of the domain (limited by the blue lines).

using unstructured grids in the rest of the domain, an illustrative example can be found in Fig. 2.8. The so called QUAD elements are placed in the boundary layer zone and it is usually referred as prismatic layer technique.

For example, in order to simulate the flow around a cylinder with critical and supercritical Reynolds numbers [6] ($1.4 \times 10^5 \leq Re \leq 8.5 \times 10^5$) it is crucial to adequately solve the boundary layer around the cylinder. For this purpose, unstructured meshes have important difficulties to adjust properly to the cylinder curvature. Thus quadrilateral elements are used in the near wall region with the option *Prismatic boundary layer* of the ANCYS-ICEM CFD software and the rest of the bi dimensional mesh is built based on triangular elements (as in Fig. 2.9). Once the plane is properly meshed, it is extruded in the normal direction to complete the grid generation.

For predicting in detail the flow around one single cylinder for academic purposes, the prismatic layer mesh is a great alternative in order to adequately solve the boundary layer around the cylinder (at very high Reynolds numbers) and conserve a good quality of the mesh elements specially in the close regions to the boundary layer and the wake created behind the cylinder. However, good quality on the transition region between prismatic and triangular elements is desired. This smooth transition drastically increases the computational demand of the simulation whenever it is needed.

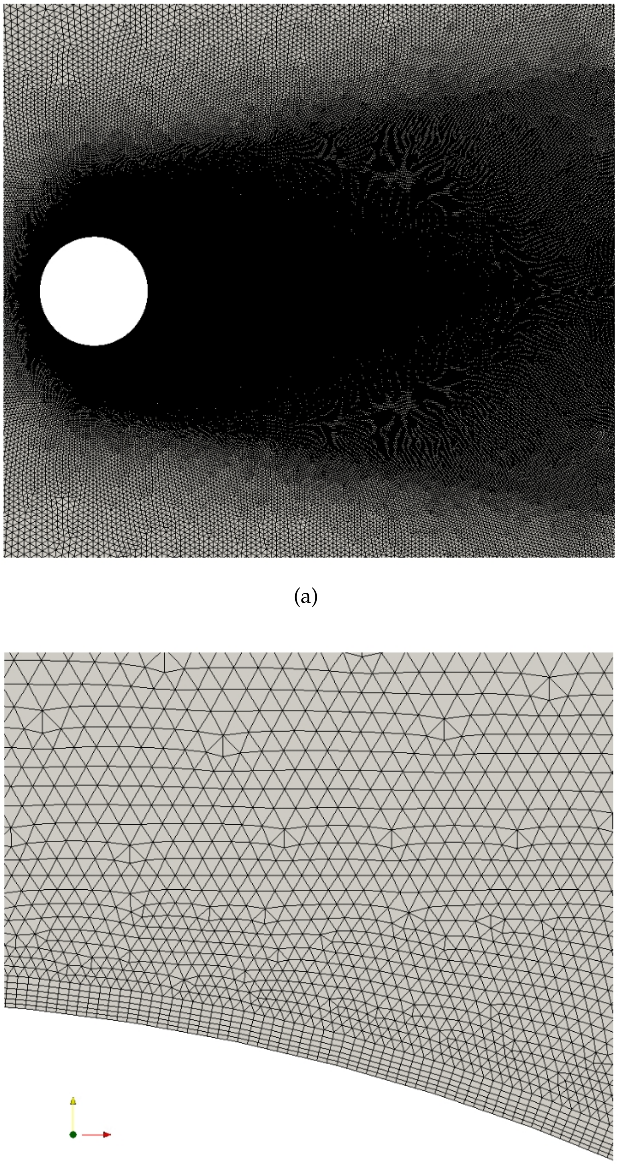

(a)

(b)

Figure 2.9: Detail of a computational 2D grid. a) Grid refinement around the cylinder (and the wake region). b) Detail of the prismatic layer at the cylinder surface.

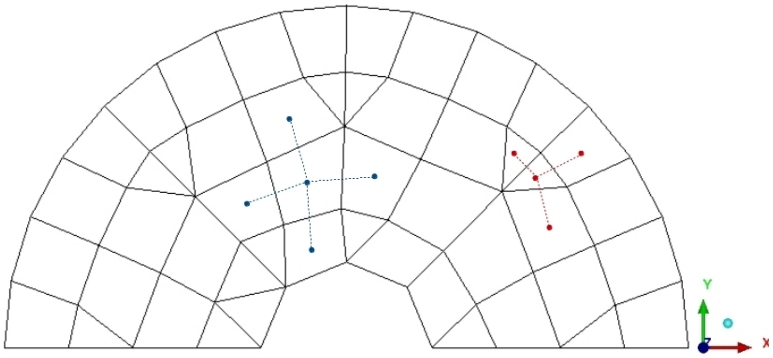

(a)

Figure 2.10: TRIs and QUADs neighborhood connectivity.

2.2.3 Hybrid meshes

A hybrid mesh is a grid that contains both ”TRI” and ”QUAD” elements. This kind of meshes have the same numerical treatment as the unstructured meshes, i.e. it requires the neighborhood connectivity to be stored and it can use any kind of element that a solver can handle.

The triangular and quadrilateral elements are arranged in a random manner defined by the grid generation software. An illustration of the neighborhood connectivity and the mixture of both types of elements is shown in Fig. 2.10.

LES was performed on the flow over a NACA profile for a flow with Reynolds number set to 3.0×10^6. Different mesh configuration have been used in order to compare their capabilities to predict the flow. Table 2.1 presents the details about the different grids used, while Fig. 2.11 illustrates the distribution of CVs of m2 and m3 respectively. As can be seen, a-priori, when comparing with m2, no significant differences can be observed, as both meshes have similar resolution. However, in terms of instantaneous and averaged statistics, quite large differences are obtained.

Figure 2.12 shows the instantaneous velocity profile obtained with grids m2 (quad-based), m3 (tri-based) and the DNS grid. At first sight, it is clear that m3 is reproducing quite well the physics of the flow, whereas the flow topology for m2 is quite different that the DNS one. For the mesh m2, the flow seems almost to reattach at about 0.35 and there is no massive separation in the trailing edge. On the other hand, m3 shows large flow separation and as expected the large-scales of the flow are well captured. Large-scales are roughly the same for both m3 and DNS, although the DNS also resolves the smallest-scales of the flow. The latter is expected to be mod-

Case	Element type	NCV_{plane}	N_{planes}	$NCV_{total} \times 10^{-6}$
m1	QUAD/TRI	60167	16	0.96
m2	QUAD/TRI	121642	32	3.9
m3	TRI	138276	16	2.21
m_{DNS}	TRI	340526	128	43.6

Table 2.1: Meshes used for the different cases

eled by the LES model. In addition to the instantaneous results, the large differences between both results can be well observed in the average streamlines obtained with m2 and m3 which are depicted in figure 2.13.

A posteriori inspection of the grid has shown that in the beginning of the laminar shear layer, there is a combination of quad-based and tri-based elements, which a priori has a good mesh quality (in terms of aspect ratio) but, such a combination produces false gradients of the velocity.

As partial conclusion, it can be said that given the difficulties that unstructured and hybrid meshes have to properly solve the boundary layer around a cylindrical surface and that its solution is crucial for the success of the simulation, structured meshes are selected for the prediction of the flow over heat exchangers. Namely the multi-block strategy is recommended to be used for designing the conformed meshes of an evaporator fin and tube heat exchanger. However, for the cases when the flow is completely laminar and the boundary layer around the cylinders is thicker, well designed unstructured meshes are also a strong recommendation due to its flexibility for refinement at certain regions.

2.3 Boundary Layer

The proper solution of the boundary layer region is crucial for the success of the entire simulation process. If this critical zone is not sufficiently good resolved, the execution can diverge or end with mistaken and unrealistic results. Many complex problems in aerodynamics and general engineering applications have been clarified by a study of the flow within the boundary layer and its effect on the general flow around a body.

Due to the relevance of the boundary layer in complex flows, it is important to carefully analyze the different situations that can be present on the flow over a heat exchanger. So many objects interacting with the flow will generate new boundary layers along the flow direction. First at the beginning of the fins, then around each cylinder and if the case considers double fin spacing, another boundary layer will be formed at the leading edge. On that ground, this section is intended to clarify the

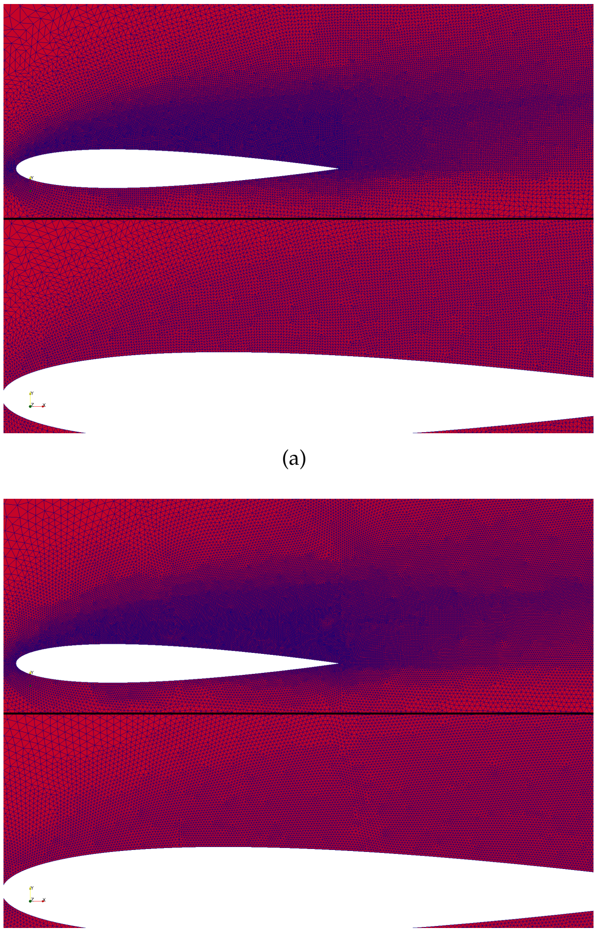

(a)

(b)

Figure 2.11: a) Mesh distribution with QUAD/TRI elements (m2). b) Mesh distribution with TRI elements (m3).

study of the flow inside the boundary layer and its interaction with the outer flow in order to build good boundary layer meshes in the complex geometrical cases.

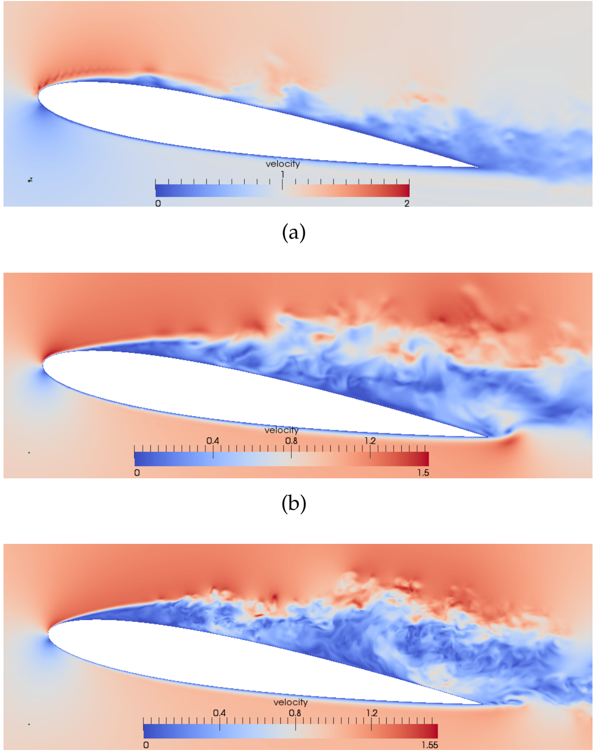

(a)

(b)

(c)

Figure 2.12: Instantaneous velocity profile obtained with the meshes a) m2, b) m3, c) m_{DNS}

2.3.1 Some history

During the week of 8 August 1904, a small group of mathematicians and scientists gathered in picturesque Heidelgerg, Germany. One of the presenters at the congress was Ludwig Prandtl, a 29-yer-old professor at the Technische Hochschule in Hannover. His presentation, and the subsequent paper that was published in the congress's proceedings one year later, introduced the concept of the boundary layer in a fluid flow over a surface.

The modern world of aerodynamics and fluid dynamics is still dominated by Prandtl's idea.

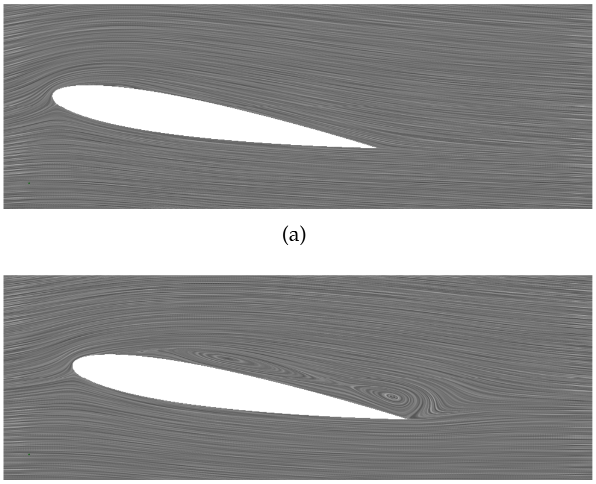

(a)

(b)

Figure 2.13: Time averaged flow. Streamlines obtained with the meshes a) m2, b) m3.

Before and after Prandtl

Archimedes (287 - 212 BC) introduced some basic ideas in fluid statics, and Leonardo da Vinci (1452 - 1519) observed and drew sketches of complex flows over objects in streams. But a quantitative physical and mathematical understanding of fluid flow began only when Isaac Newton (1642 - 1727) devoted Book II of his *Principia Mathematica* (1687) exclusively to the examination of fluid dynamics and fluid statics.

Leonhard Euler (1707 - 1783) described flow in terms of spatially varying three-dimensional pressure and velocity fields and modeled the flow as a continuous collection of infinitesimally small fluid elements. By applying the basic principles of mass conservation and Newton's second law, Euler obtained two coupled, nonlinear partial differential equations involving the flow fields of pressure and velocity. He did not account for the effect of friction acting on the motion of the fluid elements (that is, he ignored viscosity).

One hundred years after, the Euler equations were modified to account for the effect of internal friction within a flow field. The resulting equations, a system of even more elaborate nonlinear partial differential equations called the Navier-Stokes equations, were first derived by Claude-Louis Navier in 1822, and then independently derived by George Stokes in 1845. To this day, those equations are the gold standard in the mathematical description of a fluid flow [7].

On 1905 one of the most important fluid-dynamics papers ever writen was published. It was titled *"On the motion of fluids with very small viscosity"* by Ludwig Prandtl [8]. This paper gave the first description of the boundary layer concept (see Fig. 2.14). In the types of flows associated with a body in flight, the boundary layer is very thin compared to the size of the body.

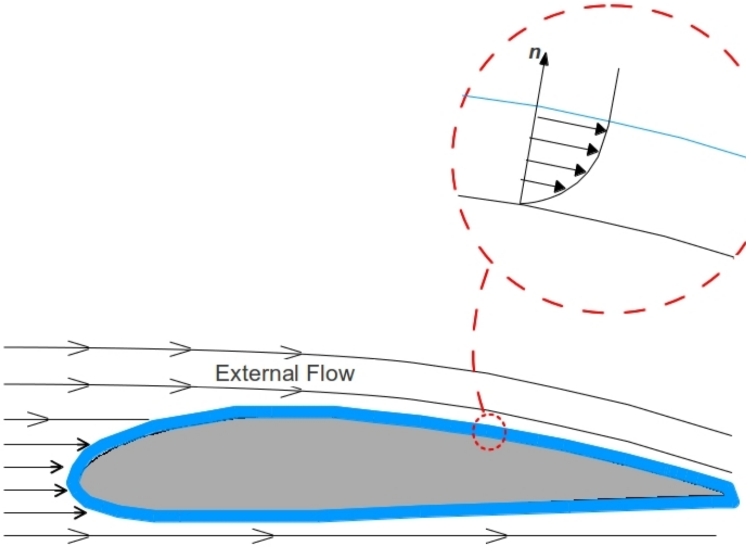

Figure 2.14: Boundary layer of a fluid over a body.

A very satisfactory explanation of the physical process in the boundary layer between a fluid and a solid body could be obtained by the hypothesis of an adhesion of the fluid to the walls, that is, by the hypothesis of a zero relative velocity between fluid and wall. If the viscosity was very small and the fluid path along the wall was not too long, the fluid velocity ought to resume its normal value at a very short distance from the wall. In the thin transition layer however, the sharp changes of velocity, even with small friction coefficient, produce marked results [8].

One of those marked results is that the boundary layer is a region of very large velocity gradients. According to Newton's shear stress law, which states that the shear stress is proportional to the velocity gradient, the local shear stress can be very large within the boundary layer. Another marked result according to Prandtl is flow separation. In given cases in certain points fully determined by external conditions, the fluid flow ought to separate from the wall. That is, there could be a layer of fluid wich insinuates itself into the free fluid.

The pressure distribution over the surface of the body is radically changed once the flow separates. The altered distribution creates a pressure drag due to flow separation, that is, a large unbalanced force that acts in the direction of the free stream flow. When the separated flow region is large, the pressure drag is usually much larger than the skin friction drag.

The type of external inviscid flow that promotes boundary layer separation is a flow that produces an adverse pressure gradient, which will occur when the flow presents an increasing pressure in the same direction of the fluid. Beyond the separation point, the boundary layer simply lifts off the surface.

An aerodynamic flow over a body can be divided into two regions: a thin boundary layer near the surface, where friction is dominant, and an inviscid flow external to the boundary layer, where friction is negligible. The outer inviscid flow strongly affects the boundary layer properties; indeed, the outer flow creates the boundary conditions at the outer edge of the boundary layer and dictates the velocity profile within the layer. On the other hand, the boundary layer is so thin that it has virtually no effect on the outer inviscid flow. The exception to the "no effect" rule is if the flow separates; then the outer inviscid flow is greatly modified by the presence of the separation region.

With the new Prandtl's boundary concept, it became possible to quantitatively calculate aerodynamic drag. Prandtl showed that for the boundary layer, the Navier-Stokes equations can be reduced to a simpler form, applicable only to the boundary layer. The resulting "boundary layer equations" are similar to Navier-Stokes in that each system consists of coupled, nonlinear partial differential equations. However, the major mathematical improvement is that the boundary layer equations exhibit a completely different (and simpler) mathematical behavior than the Navier Stokes equations.

Physicists and engineers have written hundreds of books about various aspects of boundary layer theory. The classic and best known is Hermann Schlichting's *Boundary Layer Theory* [9]. Schlichting was, during the early 1930's, a Prandtl student who conducted research on various aspects of flow with friction.

2.3.2 Boundary layer concept

The great contribution of L. Prandtl was to recognize that at high Reynolds numbers, the viscous regions remain of limited extension (δ) along the surfaces of the solid bodies immersed in the flow. For the cases with no separation of the flow, the viscous regions remain close to the body surfaces and the calculation of the pressure field may be decoupled from the calculation of the viscous velocity field.

When a fluid flows around the outside of a body, it produces a force that tends to drag the body in the direction of the flow. Drag arises from two sources: pressure and shear stress. Drag from pressure is called *form drag* because it depends on the shape or form of the body. Drag from shear stress is called *skin friction drag* or *friction drag*. Friction drag depends primarily on the amount of surface in contact with the fluid.

2.3.3 Boundary layer over flat plates

Consider a thin flat plate that is aligned with the approach flow (Fig. 2.15). Because the plate is thin, it has negligible area perpendicular to the flow and experiences no form drag. The fluid velocity at the plate surface is zero and increases to the free-stream velocity a short distance from the plate. The velocity gradient is not zero at the plate surface, so there is a shear stress there and the plate experiences friction drag.

Figure 2.15: Flat plate aligned with the flow approaching.

Fig. 2.16 shows a boundary layer on a flat plate. The following boundary layer characteristics are of primary importance:

- The boundary layer is thin ($\delta \ll x$).
- The thickness of the boundary layer increases in the downstream direction, but δ/x is always small.
- The boundary layer velocity profile satisfies the no-slip condition at the wall and merges smoothly into the free-stream velocity at the edge of the layer.
- There is a shear stress at the wall.
- The streamlines of the boundary layer flow are *approximately* parallel to the surface; that is, the velocity parallel to the surface is considerably larger than the velocity normal to the surface.

Many of the boundary layer flows are at least qualitatively similar to flow over a flat plate. The boundary layer is the region of flow where viscous forces and inertia forces are the same order of magnitude.

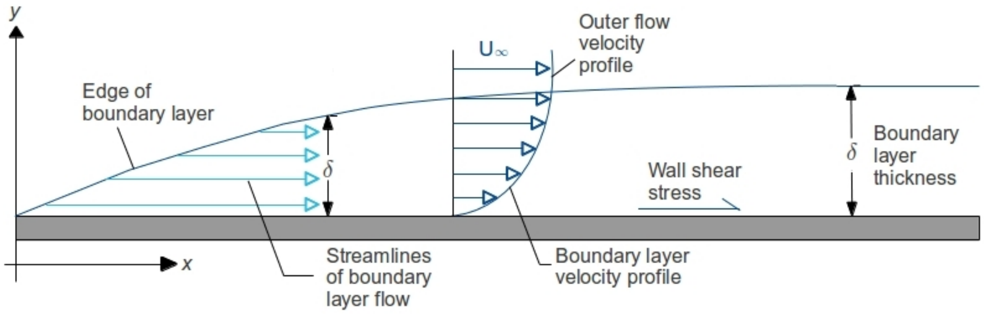

Figure 2.16: Details of boundary layer near a thin flat plate.

Laminar boundary layer

It is impossible to indicate a boundary layer thickness in an unambiguous way, because the influence of viscosity in the boundary layer decreases asymptotically outwards. The parallel component, u, tends asymptotically to the value U_∞ of the potential flow. If it is desired to define the boundary layer thickness as that distance for which $u = 0.99U_\infty$, then, the boundary layer thickness becomes:

$$\delta \approx 5.0\sqrt{\frac{vx}{U_\infty}} \tag{2.1}$$

Another common way to estimate the boundary layer thickness is the one proposed by [10]:

$$\frac{\delta}{x} \approx \frac{1}{\sqrt{Re_x}} \tag{2.2}$$

which is limited to laminar boundary layers because only viscous stress was included in the estimation proposed ($Re = \frac{U_\infty L}{\nu}$).

The relation between the dimensionless boundary layer thickness $\delta\sqrt{U_\infty/vx}$ and the Reynolds number formed with the current length, x, is plotted in Fig. 2.17. This dimensionless thickness remains constant as long as the boundary layer is laminar, and its numerical value is nearly that given in Eq. 2.1. At large Reynolds numbers, the boundary layer ceases to be laminar and transition to turbulent motion takes place. This fact can be recognized in Fig. 2.17 by noticing the marked increase in the thickness of the boundary layer as the distance from the leading edge is increased.

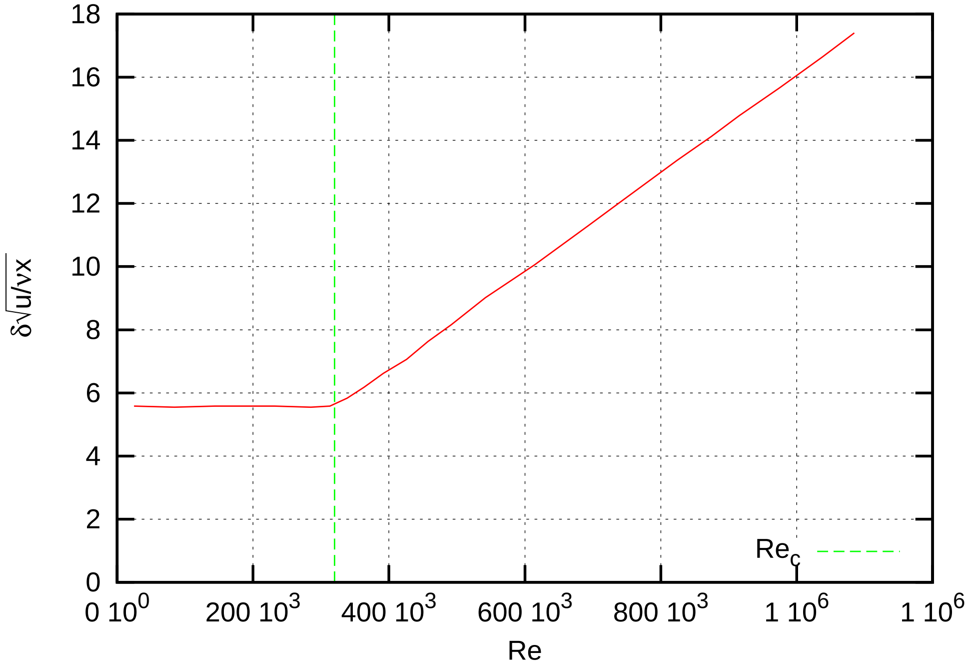

Figure 2.17: Boundary layer thickness plotted against Reynolds number [9].

Turbulent boundary layer

The boundary layer on a flat plate is the simplest boundary layer to calculate because there is no free-stream pressure or velocity gradient. Near the leading edge of the plate, the Reynolds number is small and the flow is laminar. If the plate is long enough, eventually the boundary layer becomes thick enough and the Reynolds number becomes large enough that transition occurs and the flow becomes turbulent. The laminar and turbulent portions of the boundary layer must be considered separately.

If the laminar boundary layer is allowed to develop along the plate, it eventually becomes unstable and the process of transition to turbulent flow begins. At certain location, the boundary layer becomes fully turbulent. The situation of the transition point depends on the Reynolds number and other parameters, such as surface roughness and the amount of turbulence in the flow adjacent to the boundary layer. For flow over a smooth plate, the transition Reynolds number is often taken to be

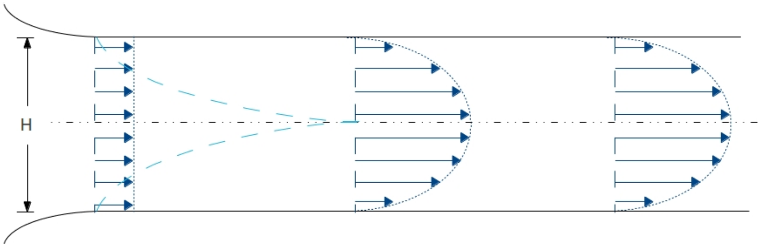

Figure 2.18: Developing and developed laminar flow.

3.2×10^5. The boundary layer downstream from the transition point is turbulent.

Thickness for turbulent boundary layer is determined by Eq. 2.3:

$$\delta = 0.370 \left(\frac{\nu}{V_\infty}\right)^{1/5} x^{4/5} \tag{2.3}$$

The turbulent boundary layer grows at a faster rate ($\delta \sim x^{4/5}$) than laminar boundary layer ($\delta \sim x^{1/2}$).

2.3.4 Flow between parallel plates

Laminar flow and heat transfer for the parallel plates have been analyzed in great detail. The parallel plates duct is a limiting geometry for the family of rectangular ducts. Since these geometries are widely used in fluid flow and heat transfer devices, the detailed analytical results for laminar flow and heat transfer for parallel plates will be described in this section.

The laminar flow in a bi dimensional duct is called *hydro dynamically developed flow* when the velocity distribution of a fluid on any cross section is invariant, this means it is independent from the axial distance as shown in Fig. 2.18.

The *hydrodynamic entrance region* is the zone where the hydrodynamic boundary layer is developing. In this region, the velocity profile changes from the entry profile up to the constant profile downstream. The flow in this space is known as *hydro dynamically developing flow* (see Fig. 2.18). Hydrodynamic entrance length L_{hy} is defined, somewhat arbitrarily, as the duct length required to achieve a duct section maximum velocity of 99% of the corresponding fully developed magnitude when the entering flow is uniform. The dimensionless hydrodynamic entrance length is expressed as $L_{hy}^+ = L_{hy}/(D_h Re)$.

Steady laminar flow on a bi dimensional duct is called *thermally developed flow* when the dimensionless temperature distribution at any cross section is invariant on the axial direction, eq. 2.4 defines the thermally developed flow condition.

$$\frac{\partial}{\partial x}\left[\frac{T_{w,m}-T}{T_{w,m}-T_m}\right]=0 \tag{2.4}$$

where $T_{w,m}$ is the peripheral mean wall temperature (eq. 2.5) and T_m is the fluid bulk mean temperature at an arbitrary duct cross section (eq. 2.6).

$$T_{w,m}=\frac{1}{P}\int_{\Gamma} T_w ds \tag{2.5}$$

$$T_m=\frac{1}{A_c u_m}\int_{A_c} uTdA_c \tag{2.6}$$

Conceptually, T_m is the temperature one would measure if the duct were cut off at a section, and escaping fluid were collected and exhaustively mixed in an adiabatic container.

In the same way, u_m is the fluid mean axial velocity. It is the integrated average axial velocity with respect to the flow area A_c:

$$u_m=\frac{1}{A_c}\int_{A_c} udA_c \tag{2.7}$$

Thermal entrance region is the zone where thermal boundary layer is under development. For this region the dimensionless temperature profile of the fluid varies from the initial shape at the point where the heating started to a constant distribution downstream of the duct. The flow in this region is known as *thermally developing flow*.

The thermal entrance length L_{th} is defined, somewhat arbitrarily, as the duct length required to achieve a value of local Nu_x equal to $1.05Nu$ for fully developed flow. The dimensionless thermal entrance length is expressed as $L^*_{th} = L_{th}/(D_h Pe)$. The local Nusselt number is defined as $Nu = \frac{hD_h}{\lambda}$, where h is the convective heat transfer coefficient, D_h is the corresponding hydraulic diameter of the duct and λ is the thermal conductivity of the fluid.

The velocity profile on the thermally developing region may be developed or under develop. When a flow is developing both thermal and hydrodynamic profiles it is called *simultaneously developing flow*.

Fully developed velocity profile

The fully developed velocity profile for the flow between flat plates can be calculated from the momentum equations. The resulting analytical velocity profile is expressed by eq. 2.8 [11].

$$U(y) = 6U_m \frac{Hy - y^2}{H^2} \tag{2.8}$$

Fanning friction factor is defined as the ratio of wall shear stress τ to the flow kinetic energy per unit volume $\rho u_m^2/2$. The peripheral average axially local fanning friction factor is then expressed as eq. 2.9.

$$f_x = \frac{\tau_x}{\rho u_m^2/2} \tag{2.9}$$

In the hydrodynamic entrance region, pressure drop results from the wall shear and the change in momentum flow rate across the complete channel. For this reason an *"apparent"* fanning friction factor is defined, which takes into account both factors, i.e. wall shear stress and change in momentum flow (eq. 2.10).

$$\Delta p^* = \frac{\Delta p}{\rho u_m^2/2} = f_{app} \frac{x}{r_h} \tag{2.10}$$

f_{app} is thus based on the total pressure drop from $x = 0$ to x. It takes into account both the skin friction and the change in momentum rate (due to change in the shape of the velocity profile) in the hydrodynamic entrance region.

For the case of fully developed flow through a duct, the velocity profile is invariant across any flow cross section. Consequently, the wall shear stress does not change axially, and the average friction factor is the same as the local friction factor for that part of the duct beyond the hydrodynamic entry length.

When the problem refers to the hydro dynamically developed flow, the friction factor inversely proportional to Re by a constant factor (eq. 2.11).

$$fRe = 24 \tag{2.11}$$

The analysis made on the course of this thesis, included bi dimensional numerical simulations of flow between parallel plates in order to validate the closure or the problem (including, initial and boundary conditions, convective schemes, geometry selected as domain, among others). The author found $fRe = 23.9529$ constant along the axial coordinate of the channel for the problem with developed velocity profile. The estimated error is of 0.19%.

Hydrodynamic entry length problem

The boundary condition at the duct inlet has been discussed by different authors using diverse methods. The hydrodynamic entry length problem for parallel plates was first investigated by Schiller [12] by the integral method. His results are very good at the entrance but poor downstream. Van Dyke [13] considered two entry conditions: velocity profile uniform at $x = -\infty$, and velocity profile uniform at $x = 0$. The first condition was also referred to as the entry condition for a "cascade of plates in a uniform oncoming stream". Van Dyke concluded that the most satisfactory model is that of uniform flow into an infinite cascade of parallel plates.

In the procedures described on this thesis, the velocity distribution at the entrance was considered to be uniform, and the idealizations were made that the effects of the $\mu(\frac{\partial^2 u}{\partial x^2})$ and $\frac{\partial p}{\partial y}$ terms in the momentum equations were negligible. The effects of these terms are retained in the solution of the complete set of Navier-Stokes equations. The development length calculated by boundary layer type equations is too small compared to that calculated by solving the complete Navier-Stokes equations.

Wang and Longwell [14] rigorously solved the complete set of Navier-Stokes equations. The subsequent solution was obtained by a finite difference iterative method. One interesting result of the analysis was that they obtained concave velocity profiles in the entrance region near the center of the plates. Normally, one would expect either a uniform or a convex profile. They concluded that if the velocity distribution and pressure gradients were accurately required near the entrance region, the boundary layer type idealizations were not appropriate and full differential equations must be solved with realistic boundary conditions.

The dimensionless hydrodynamic entrance length L^+_{hy} defined earlier, is constant when based on a boundary layer type momentum equation. Bodoia [15] and Liu [16] both obtained L^+_{hy} as 0.011. L^+_{hy} is a function of Re for low Reynolds number flows when the complete set of Navier-Stokes equations is solved. Atkinson et al. [17] presented (eq. 2.12) for cases where entrance profile is uniform at $x = 0$.

$$\frac{L_{hy}}{D_h} = 0.3125 + 0.011 Re \tag{2.12}$$

Three different Reynolds numbers were simulated for the hydrodynamic entry length problem ($Re =$ 100,500 and 1000). The results were compared against Atkinson correlation [17] (Eq. 2.12) and the relative difference between simulations and the expected result were for $Re = 100$ $\varepsilon = 0.142\%$, for $Re = 500$ $\varepsilon = 0.715\%$ and finally for $Re = 1000$ $\varepsilon = 0.784\%$. The minimum entry length is found for the lower Reynolds number while the boundary layer thickness is quantified at the larger Reynolds number. Since the same mesh is to be used for all the cases, it is recommended to design a mesh that can properly solve the details for all the cases. Hence, in the longitudinal direction of the flow at least 15 CV are placed inside the dimensionless hydrodynamic entrance length L^+_{hy}. While in the normal direction (perpendicular to the top and bottom solid walls) at least 5 CV should be used in order to build a good boundary layer mesh for the simulation of a channel flow (for laminar conditions, the mesh could be less demanding). It is important to emphasize the relevance of a smooth grow of the mesh for the rest of the domain.

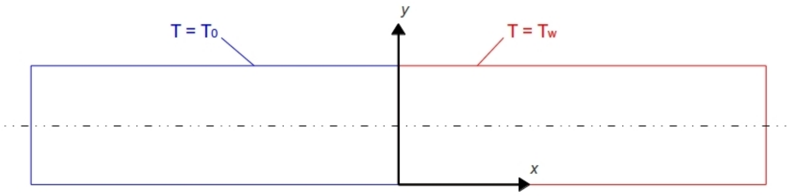

Figure 2.19: Thermal boundary conditions for the temperature problem treatment.

Thermal entry length problem

When the Peclet number ($Pe_{Dh} = \frac{D_h U_\infty \rho C_p}{\lambda}$) is greater than 100 and the heating/cooling region is long enough, the axial heat conduction of the fluid may be neglected [11]. However when the study is about lower Peclet numbers, it is of great importance to solve the complete set of Navier-Stokes equations. The dimensionless entrance length calculated by Shah [18] is defined in Eq. 2.13

$$L^*_{th} = \frac{L_{th}}{D_h Pe} \tag{2.13}$$

where $L^*_{th} = 0.00797350$.

Fig. 2.19 depicts the geometry and thermal boundary conditions recommended by the author to resolve the temperature problem on a parallel plate configuration. It can be distinguished that at $x = 0$ the temperature at the wall suddenly changes from T_0 to T_w. The temperature of the fluid at the entrance of the channel (when $x \to -\infty$) has a uniform profile of value T_0. Because of the heat exchanged between the solid walls and the fluid, temperature from the moving flux will asymptotically tend to the uniform wall temperature T_w.

On the methodology applied for computations on the problems treated at this thesis, the boundary layer type idealizations were not assumed. Thus axial heat conduction is taken into account and Peclet number is important.

Several simulations were performed as an effort to understand the flow along the entire domain of the channel. Fig. 2.21 shows the local distribution of the Nusselt number along the duct for a case where $Re = 4.0$ and $Pr = 1.0$, i.e. $Pe = 4.0$ (velocity profile is set to be fully developed as inlet boundary condition). Weigand [11] data was used for validation purposes, he solved the energy equation on its elliptic form (without neglecting the axial heat conduction term) because this particular Peclet number is considered to be small. At the initial zone of the thermal problem ($x = 0$), the size of the CV is smoothly stretched up to $x^* = 0.008$. Fig. 2.20 show an example of the mesh distribution to solve the thermal problem for a channel flow.

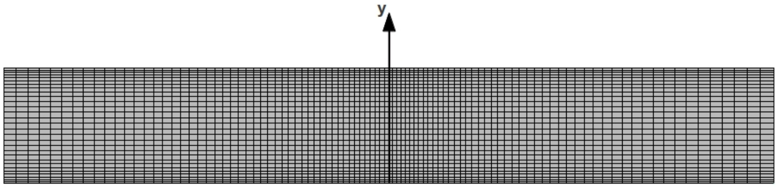

Figure 2.20: Detail of the mesh used to solve the thermal entry length problem.

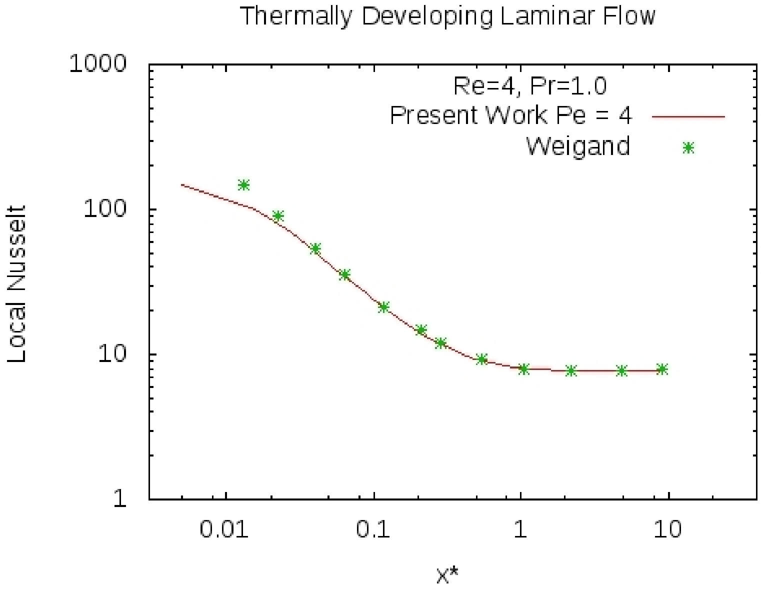

Figure 2.21: Local distribution of Nusselt ($Pe = 4.0$).

Moreover, Brown [19] expanded the first ten values of the infinite series solution displayed in eq. 2.14

$$\theta = \frac{T - T_w}{T_e - T_w} = \sum_{n=0}^{\infty} C_n Y_n exp(\frac{-32}{3}\lambda_n^2 x^*) \tag{2.14}$$

$$\theta_m = \frac{T_m - T_w}{T_e - T_w} = 3\sum_{n=0}^{\infty} \frac{G_n}{\lambda_n^2} exp(\frac{-32}{3}\lambda_n^2 x^*) \tag{2.15}$$

$$Nu_{x,T} = \frac{8}{3}\frac{\sum_{n=0}^{\infty} G_n exp(\frac{-32}{3}\lambda_n^2 x^*)}{\sum_{n=0}^{\infty} \frac{G_n}{\lambda_n^2} exp(\frac{-32}{3}\lambda_n^2 x^*)} \tag{2.16}$$

$$Nu_{m,T} = \frac{1}{4x^*} ln(\frac{1}{\theta_m}) \tag{2.17}$$

Sellers et al. [20] presented some expressions (eq. 2.18), that were capable to solve the eigenvalues and eigenfunctions. Shah [21] used the first 121 terms of those series and the results are illustrated in Fig. 2.22.

$$\lambda_n = 4n + \frac{5}{3} \tag{2.18}$$

$$G_n = 1.0127879 {\lambda_n}^{-1/3} \tag{2.19}$$

When the Peclet number under analysis is considered to be large enough to neglect the axial heat conduction, Shah and London [18] is a typical reference. Fig. 2.23 illustrates the local and averaged Nusselt number for two different cases, $Pe = 71$ and $Pe = 1420$ respectively. The local study is found to be in a very good concordance with reference data, but for the mean Nusselt number distribution some discrepancies are found at the inlet zone, specially if the Peclet number is decreased.

The effect of the deviation observed on clause b) of Fig. 2.23 for $Pe = 71$ is due to the axial heat conduction phenomena between the plates and the working fluid. Shah and London [18] disregard this effect on their solution of the equations with no distinction on the Peclet number. However this has been found to be a good hypothesis only for large Peclet ($Pe > 100$). To understand and illustrate this effect, numerical simulations were performed, and the distribution of the dimensionless temperature profile along the center line of the parallel plates channel is depicted on Fig. 2.24. The symbols represent data taken from Weigand [11] for the corresponding Peclet number.

Given the boundary conditions of the problem (Fig. 2.24a.), at $x^* = 0$ it is expected that the dimensionless temperature at the center line would be equal to the unity, as expressed on equation 2.20.

$$\theta|_{y=H/2} = \frac{T_{y=0} - T_H}{T_C - T_H} = 1 \tag{2.20}$$

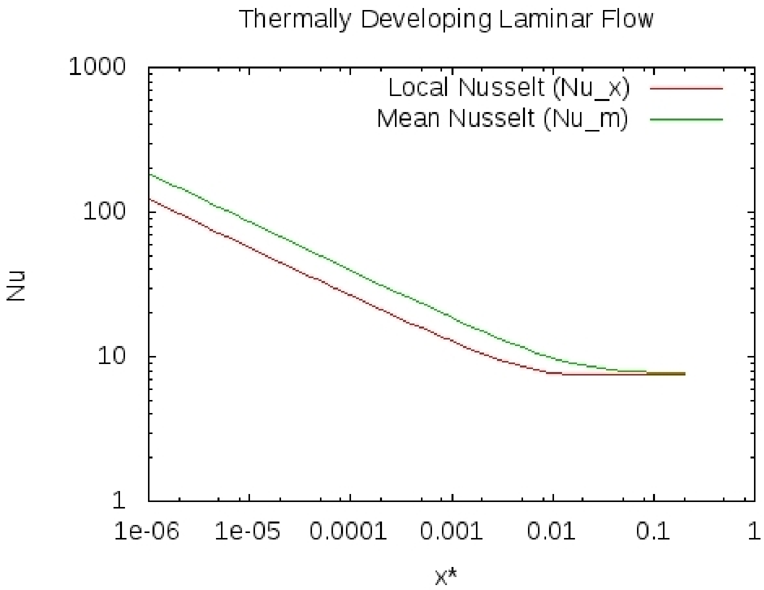

Figure 2.22: Local ($Nu_{x,T}$) and mean ($Nu_{m,T}$) distribution of Nusselt number for the thermally developing flow problem. [21].

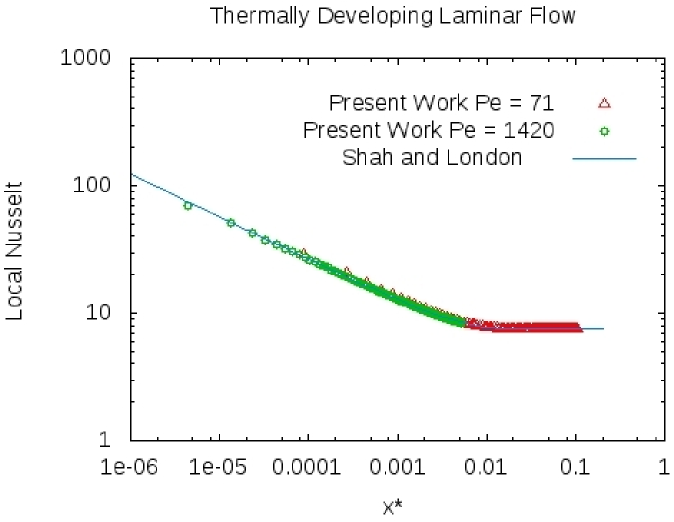

(a)

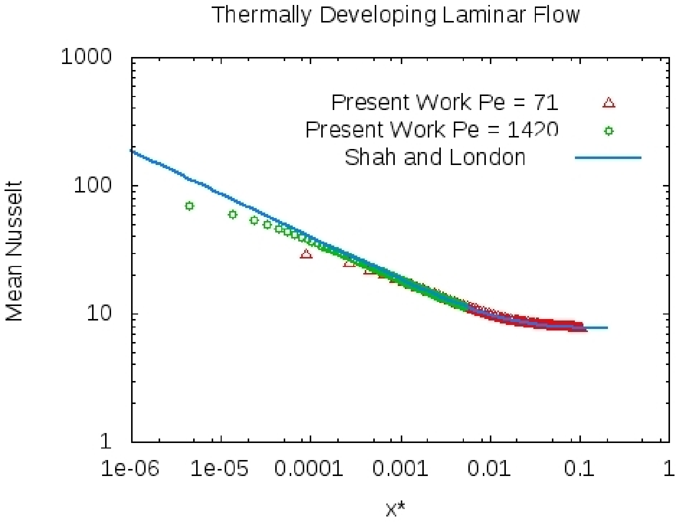

(b)

Figure 2.23: a) Local ($Nu_{x,T}$) and b) mean ($Nu_{m,T}$) distribution of Nusselt number for medium to large Peclet numbers.

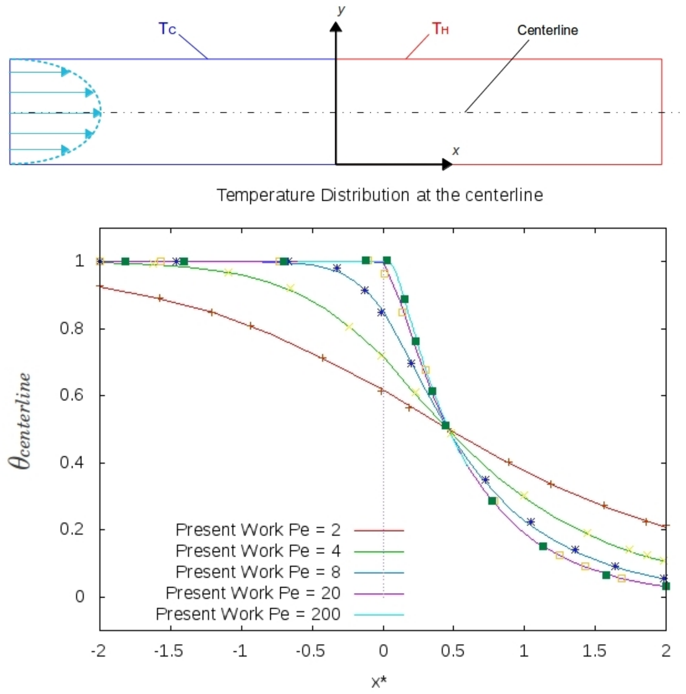

Figure 2.24: Dimensionless temperature distribution along center line for low Peclet numbers. Symbols represent data from Weigand [11].

Fig. 2.24 shows that for very small Peclet values, the axial heat conduction effect is clearly present, and heating from downstream can be concluded. Thus the energy equation must be resolved on its elliptic form (Eq. 2.21).

$$\rho c_p u(y)\frac{\partial T}{\partial x} = \lambda(\frac{\partial^2 T}{\partial x^2} + \frac{\partial^2 T}{\partial y^2}) \tag{2.21}$$

Simultaneously developing flow

This is the problem of both, hydrodynamic and thermal entry length at the same time. Both profiles are under develop from the beginning of the simulation.

Simultaneous development of velocity and temperature profiles for parallel plates was first investigated by Sparrow [22] for equal wall temperatures of the plates. Stephan [23] employed an approximate series solution for the combined entry length problem and approximated his $Nu_{m,T}$ by the empirical equation 2.22 for a Pr range of 0.1 to 1000.

$$Nu_{m,T} = 7.55 + \frac{0.024(x^*)^{-1.14}}{1 + 0.0358(x^*)^{-0.64}Pr^{0.17}} \tag{2.22}$$

Apparent fanning friction factor is defined on eq. 2.10, the approximation obtained by Bodoia [15] for this parameter and the ratio of maximum velocity over mean velocity along the channel is shown in Table 2.3.4.

Fig. 2.25 illustrates the results obtained with the numerical simulations and the comparison against [15] is shown for validation. The case is a flow emulating air ($Pr = 0.71$) with Reynolds number of 100. Friction factor, apparent friction factor (Eqs. 2.9 and 2.10 respectively) and ratio of maximum and mean velocity along the channel on its dimensionless form is depicted. Once the flow is developed, the results have the expected behavior, and the developed values of f_{app} and u_{max}/u_m present an excellent agreement with the comparison reference. The differences between present simulations and the literature are visible at the entrance region. This is a numerical error induced by the mesh size at the inlet zone, the axial coordinate is expressed on its dimensionless form and this would need very small control volumes (CV). Nevertheless, on the real duct, this x^+ represents an extremely small part of the parallel plates channel ($0.08\ mm$ at the entrance of a channel with axial length equal to $400\ mm$).

Thermal boundary layer of this problem is under develop as well as the hydrodynamic boundary layer. Hwang and Fan [24] obtained the numerical solution by finite difference method for the combined entry length problem neglecting the axial heat conduction at the entrance. They presented their results for $0.1 < Pr < 50$ as mean Nusselt number for constant temperature boundary condition at the walls ($Nu_{m,T}$). Table 2.3 shows the numerical results published for a fluid simulating air ($Pr = 0.72$) [24].

x^+	$\frac{u_{max}}{u_m}$	$f_{app}Re$
0.0000625	1.062	496.8
0.000125	1.075	306.6
0.000250	1.101	210.0
0.000375	1.124	174.3
0.000500	1.144	153.3
0.000625	1.162	138.4
0.000750	1.177	127.2
0.001000	1.203	111.1
0.001250	1.226	99.96
0.001500	1.246	91.73
0.001750	1.265	85.36
0.002000	1.282	80.21
0.002500	1.312	72.38
0.003125	1.344	65.42
0.003750	1.371	60.33
0.005000	1.411	53.26
0.006250	1.439	48.50
0.009375	1.476	41.34
0.012500	1.490	37.31
0.031250	1.494	29.41
0.062500	1.500	26.70

Table 2.2: Ratio of maximum and mean velocity and apparent friction factor along the channel for developing laminar flow. Bodoia [15].

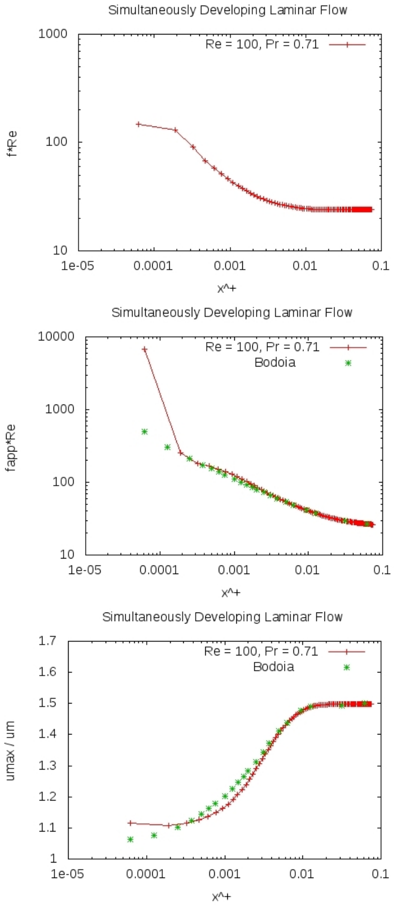

Figure 2.25: Friction factor, apparent friction factor and ratio of velocities along the parallel plates duct. Green symbols represent data from Bodoia [15].

x^*	$Nu_{m,T}$
0.0000434	116.1
0.0000868	72.87
0.0002600	44.14
0.0004340	35.09
0.0006080	30.23
0.000955	24.91
0.001300	21.90
0.001740	19.52
0.002600	16.63
0.003470	14.90
0.00434	13.74
0.00608	12.24
0.00868	10.96
0.01480	9.59
0.02340	8.83
0.0321	8.47
0.0434	8.23
0.0651	7.99
0.0942	7.79
0.1519	7.71

Table 2.3: Mean Nusselt number for simultaneously developing flow between parallel plates duct. Hwang and Fan [24] $Pr = 0.72$.

The simulations made for the combined entry length problem corresponded to three different flow regimes, every one of them with thermophysical properties of air. Fig. 2.26 illustrates the results obtained for the cases of $Re = 10$ and $Re = 100$. As can be seen by the figure, for lower Peclet number (Fig. 2.26a.) has some discrepancies against reference data at the entrance region, this is due to the axial heat conduction effect explained earlier on this chapter.

Finally an extra simulation was made for a higher Reynolds number ($Re = 2000$) with the same fluid properties considered. Validation data is available for this case, Nguyen and Maclaine-cross [25] also numerically studied this problem and presented results for $x^* > 0.00153$. The values of the dimensionless axial coordinate of the study made for this thesis are significantly smaller than those presented by other authors. This is an indication of the good quality of the mesh at the entrance region of the parallel plates geometry. Fig. 2.27 illustrates the results obtained for this case and excellent agreement is found due to the high Peclet number and the negligible effect of axial heat conduction that other authors assume.

Transition from laminar to turbulent flow in parallel plate channels

The difficult problem of understanding the physical mechanisms at work in the change from laminar to turbulent flow, within its wide range of active time and space scales has occupied the fluid dynamics research community for the past century. When an airfoil is placed parallel to a running fast moving air, the boundary layer forms on its surface as the velocity of the air at the surface must be reduced to zero. Near the front of the airfoil the boundary layer flow is smooth and steady, but further downstream it is found to become highly irregular, unsteady and turbulent. Scientists working in transition prediction aim to answer the questions of where and why this transition occurs. It is a problem distinct from that of understanding turbulent flow itself. For example, a turbulent flow offers more drag resistance, and indeed, an aircraft is designed intended to keep most part of the flow over its wings laminar.

Understanding the physical structures and flow patterns visible in the late end stage of transition and the initiation of turbulent spots, isolated patches of turbulence surrounded by laminar flow should also throw much information on the structures seen in fully developed wall turbulence and help in the equally difficult problem of modeling turbulent flow [26].

The lower critical Reynolds number for the laminar-turbulent transition has been calculated theoretically as a function of the duct aspect ratio (ratio of width to height) for the steady, isothermal flow of Newtonian fluids in straight ducts with constant rectangular cross section. Davies and White [27] measured the critical Reynolds number as 2960. Cornish [28] experimentally measured 2360. The data presented by Allen and Grundberg [29] estimates $Re_c = 2300$. Rothfus et al. [30] proposed

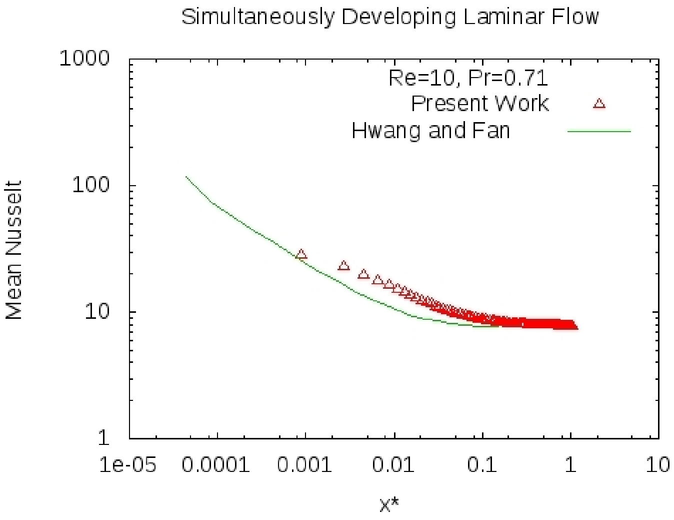

(a)

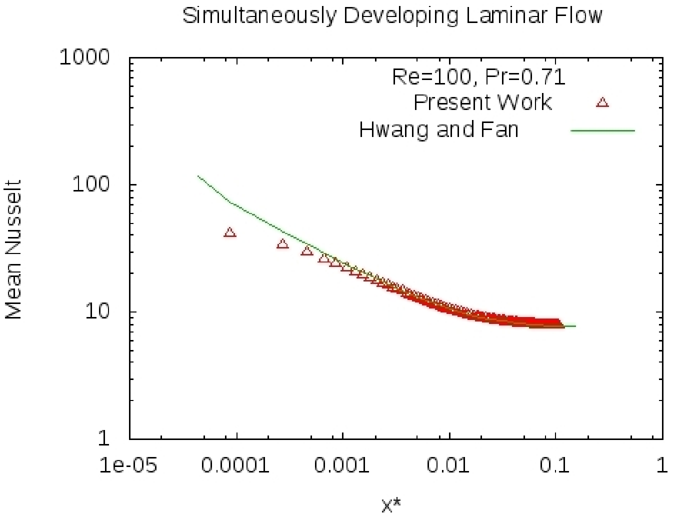

(b)

Figure 2.26: Mean Nusselt number along the parallel plates duct for a) $Pe = 7.1$ and b) $Pe = 71$ with simultaneously developing flow. Green line represent data taken from Hwang and Fan [24].

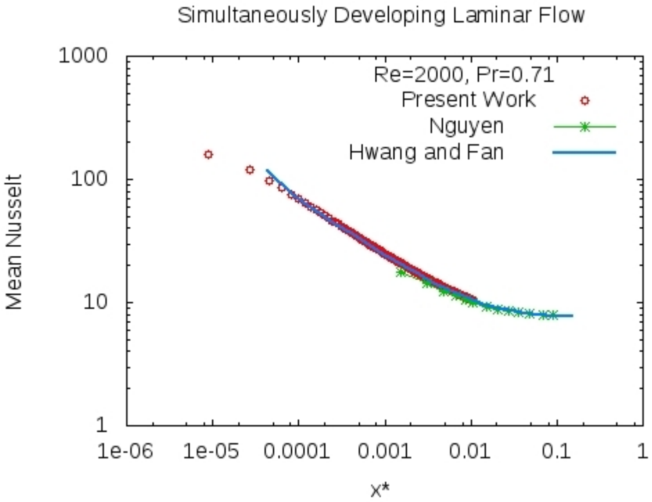

Figure 2.27: Mean Nusselt number along the parallel plates duct for $Pe = 1420$ with simultaneously developing flow. Green symbols represent data taken from [25] and blue line represent data taken from [24].

empirically that the product $Re_c(v_{max}/\overrightarrow{v})$ is a constant equal to 4200.

It has been observed that the flow development process depends critically on the specifics of the inlet conditions characterized by the shape of the velocity profile and the magnitude of the turbulence intensity. This is the main reason of the discrepancies in the literature in order to obtain a definite critical Reynolds number. However a general consensus of the results studied is that laminar breakdown in flat rectangular ducts occurs for a Reynolds number on the order of $2500 - 4000$, where the Reynolds number is based on the mean velocity and the hydraulic diameter [5].

2.3.5 Flow around cylinders

The flow past a circular cylinder is associated with various instabilities. These instabilities involve the wake, separated shear layer and boundary layer. Williamson [31] has given a comprehensive description of the flow phenomena at different Reynolds numbers (based on the cylinder diameter and free-stream velocity). Up to $Re \sim 40$, the flow is steady with two symmetric vortices on each side of the wake center line. The first wake instability, manifestation of a Hopf bifurcation, occurs at $Re \sim 47$. For $Re > 47$, although it remains laminar, the flow becomes unsteady and asymmetric. Von Karman vortex shedding is observed for slightly larger Re. At $Re \sim 190$, three-dimensional instabilities, such as formation of vortex loops, deformation of primary vortices and streamwise and spanwise vortices, appear in wake. The wake flow undergoes a series of complex three-dimensional instabilities, eventually making it turbulent. When the Reynolds number is approximately 260, the flow experiences transition to finer scale three dimensionality (also named as mode B instability). With increasing Reynolds number, the three dimensional cylinder wake becomes more chaotic. Finally, according to Prasad and Williamson [32], the shear layers separating from the cylinder become unstable at Reynolds number around 1200.

Boundary layer

The value of the critical Reynolds number (Re_c) varies in the literature from 300 to 3000. It is believed that the separating shear layers are very sensitive to various experimental factors such as free-stream turbulence level, acoustic noise, cylinder vibrations, boundary conditions and aspect ratio [33]. Beyond a certain critical Reynolds numbers, the shear layer separating from the upper and lower surface of the cylinder, starts becoming unstable via the Kelvin-Helmholtz mode of instability. The transition point, beyond which the separated layer becomes unstable, moves upstream with increase in Reynolds. At $Re \sim 2 \times 10^5$, the boundary layer on the cylinder surface undergoes a transition from laminar to turbulent. This transition leads to a delay of the separation of flow from the cylinder surface causing a substantial reduction in the drag force that the cylinder experiences. This is often referred to as *Drag crisis*.

Depending on the free stream turbulence and surface roughness, beyond a certain critical Reynolds number, the boundary layer on the cylinder becomes turbulent [34, 35]. It is accompanied with a significant reduction in drag and is often referred to as drag crisis. It also results in an increase in the base pressure coefficient. The drag coefficient for the subcritical flow is approximately 1.2 and it reduces to about 0.3 for the supercritical flow. For the transcritical flow [34], it again increases to almost 0.7. For a smooth cylinder, critical Reynolds number (Re_c), is approximately equal to 3×10^5. As Re is increased, beyond the critical value, transition in boundary layer moves ahead of the laminar separation point. The turbulent boundary layer can withstand a greater pressure rise and delays separation.

Drag coefficient

Understanding the drag characteristics of objects in fluid flow is essential for engineering design aspects, such as to reduce the drag on automobiles, air-crafts, and buildings.

As the flow circulates through the entire domain, the cylinder obstructs the path of the fluid flow causing the stream to deviate from its otherwise uninterrupted flow path. The uniform velocity profile of the flow becomes non-uniform as the fluid passes by the cylinder.

The drag force is often non-dimensional as a function of Reynolds number. This is then referred to as the *drag coefficient* (eq. 2.23). Similarly, the pressure acting on each differential element of an object may be normalized by the dynamic free-stream pressure $\frac{1}{2}\rho U_\infty^2$ to obtain the *pressure coefficient* (eq. 2.24).

$$C_D = \frac{F_D}{\frac{1}{2}\rho U^2 A} \tag{2.23}$$

$$C_p = \frac{\Delta p}{\frac{1}{2}\rho U^2} \tag{2.24}$$

Fig. 2.28 illustrates drag coefficient over a smooth circular cylinder. The cylinder has equal amount of area parallel and perpendicular to the flow and experience both form drag and friction drag. The Reynolds number is based on the diameter and the drag coefficient is based on frontal area.

White [36] suggested the following curve fits for numerical work calculating the drag coefficient:

$$C_{D,cylinder} \approx 1.0 + 10.0(Re)^{-0.67} \tag{2.25}$$

valid for $Re < 2 \times 10^5$.

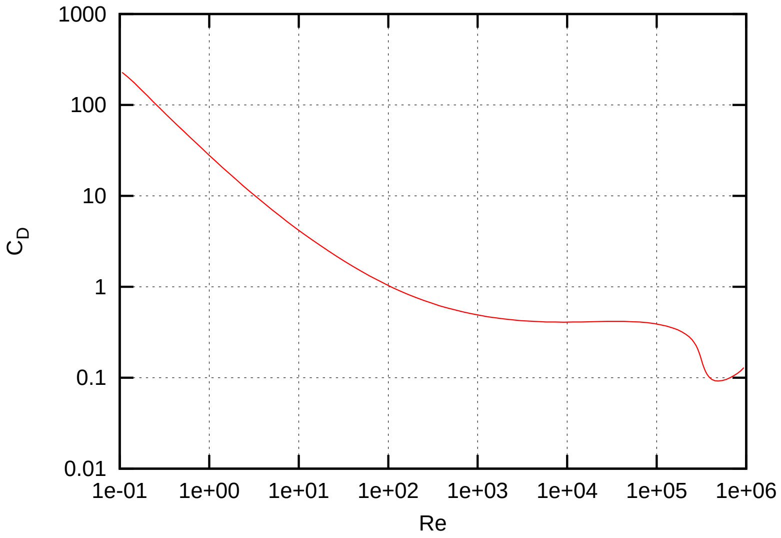

Figure 2.28: Drag coefficient of smooth cylinder as a function of Reynolds number [9].

At low Reynolds numbers, the cylinder drag coefficient vary with Reynolds number, decreasing as Reynolds number increases. At a Reynolds number of about 10^3, the drag coefficient becomes essentially constant and the curve is flat. At a Reynolds number of about 5×10^5, the cylinder drag coefficient dips and then returns to a lower constant value.

Consider the boundary layer on a circular cylinder. The pressure distribution has a profound effect on the boundary layer and the shape of the cylinder causes a pressure change in the flow. The flow outside the boundary layer is determined by a balance between pressure force and fluid momentum. On the front of the cylinder, the fluid momentum increases and the pressure drops, while on the back side the fluid exchanges momentum for increasing pressure. For the boundary layer, the flow is determined by a balance between momentum and pressure plus viscous forces. On the back side of the cylinder, as the pressure begins to rise, the fluid must exchange momentum for pressure. Because the boundary layer is deficient in momentum, it is unable to penetrate very far into the rising pressure. The pressure causes the fluid in the boundary layer to stop and, ultimately, reverse its direction. The boundary layer separates from the cylinder surface and a broad wake forms behind the cylinder. The separating boundary layer pushes the flow streamlines outward and therefore alters

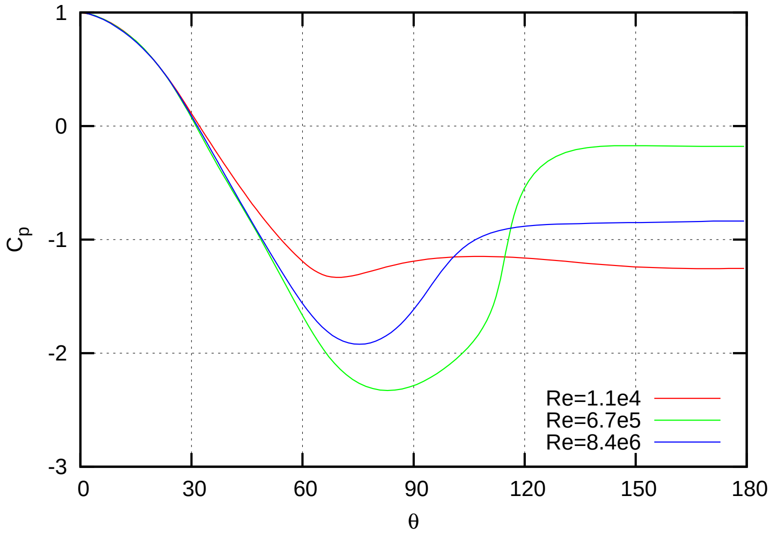

Figure 2.29: Pressure distribution on cylinder surface for laminar and turbulent boundary layers [9].

the entire flow pattern and pressure distribution.

A turbulent boundary layer contains more momentum than a laminar boundary layer. Therefore, the turbulent boundary layer can penetrate farther into the rising pressure on the rear of the cylinder, and separation is delayed. The wake is smaller, and the pressure in the wake is higher. Fig. 2.29 shows pressure distributions on cylinders with laminar and turbulent boundary layers. The higher average pressure in the back of the cylinder with a turbulent boundary layer results in lower form drag and lower drag coefficient, even though the friction drag of the turbulent boundary layer is higher than that of the laminar layer.

For laminar flow conditions, the boundary layer separation occurs at approximately 82 degrees from the stagnation point. After this point, the pressure coefficient remains negative and approaches -1.0 (Fig. 2.29). This increases the severity of the pressure gradient and increases total pressure drag.

It is clear that the success of the simulation of the flow around a single cylinder is closely related to the accurate prediction of the boundary layer features of the studied flow. Thus, the mesh used on this critical region is of major priority on the preprocessing tasks. Fig. 2.30 illustrates the different results obtained for the same flow regime ($Re = 3.8 \times 10^5$) using different mesh strategies. Both meshes

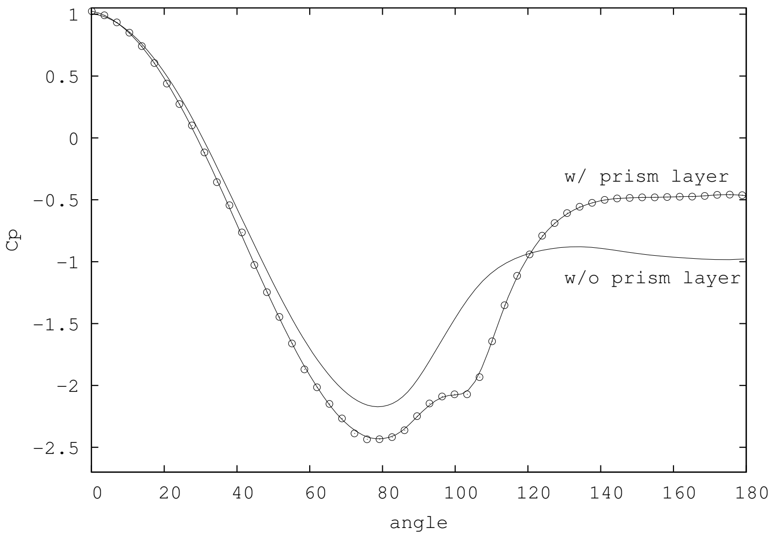

Figure 2.30: Pressure distribution on cylinder surface for $Re = 3.8 \times 10^5$ with different meshes.

are unstructured with similar resolution, one of them is built using the prismatic layer technique (explained on Sec. 2.2.2) while the other mesh is built using only triangular elements.

The mesh with a prismatic layer captures the formation of a laminar separation bubble (LSB) as it is reported in experimental studies [37]. This LSB which is a fundamental feature of the flows in the critical regime can be observed as a plateau in the pressure at about $\theta = 100°$. As can be seen from the figure, the mesh without the prismatic layer is not capable of capturing this LSB as it does not have enough resolution in the boundary layer.

2.4 Periodic boundary condition

2.4.1 Numerical treatment

The main core of the research done within this doctoral thesis, is composed by several numerical experiments aiming at a better understanding of the fluid dynamics and heat transfer mechanisms on the external part of typical high efficiency fin and tube heat exchangers (whether pin fin matrix or evaporator configurations).

Most part of the simulations were performed by using the in-house TermoFluids software [2], it is a very complete software capable of striking many different issues under distinct contexts (for either academic or industrial interests). Normally a Computational Fluid Dynamics (CFD) simulation is composed by three different stages: i) the pre-process (where the set up of the case is defined), ii) the time integration (simulation is advanced in time by solving steady or unsteady equations), and iii) the post-process (where the results are printed and analyzed) [38].

The computational domain is defined and a structured or unstructured mesh should be built dividing the geometry into small control volumes (CV) on which the differential equations will be discretized and solved with well known numerical methods. A mesh is set up by defining two types of control volumes: i) inner CVs and ii) boundary CVs.

- Inner control volumes are the three dimensional cells that are confined by the boundary control volumes. The algebraic equations that define the physics of the problem are solved by approximations on each inner CV which is always surrounded by other CVs denominated as neighbors in every direction (x,y,z for Cartesian meshes).
- On the other hand, boundary CV are used to define the boundary conditions that delimit the problem. Usually, no equation is solved at each time step on this type of CV because it is defined at be preprocessing of the simulation (remember, this CV does not have any volume attached to it, is only composed by the boundary face).

All the processes related to the boundary conditions are labeled in TermoFluids as *BoCo*. There are different types of *BoCos* included, such as: TYPE_FLUID (applied on fluid nodes), TYPE_FLUID_CONV (applied on convective nodes), TYPE_SOLID (applied over solid nodes), TYPE_COUPLED (applied over the interface between two different domains, generally fluid-solid), TYPE_PERIODIC (applied to simulate periodic domains).

Moreover, *BoCoBase* is the class used only for boundary conditions. It dictates the basic algorithm for the use of a boundary condition. It is possible to evaluate the boundary condition by solving the corresponding coefficients of the equation, or directly obtain the value of a specific field at the boundary.

The structure of the different boundary conditions implemented on the TermoFluids software is illustrated in Fig. 2.31.

TermoFluids has an increasing number of users and developers with different needs and interests. The growing capabilities of the software is a result of the interaction between the group of scientists involved with the CTTC. Particularly the author contributed in the development of a specific part of TermoFluids. Namely

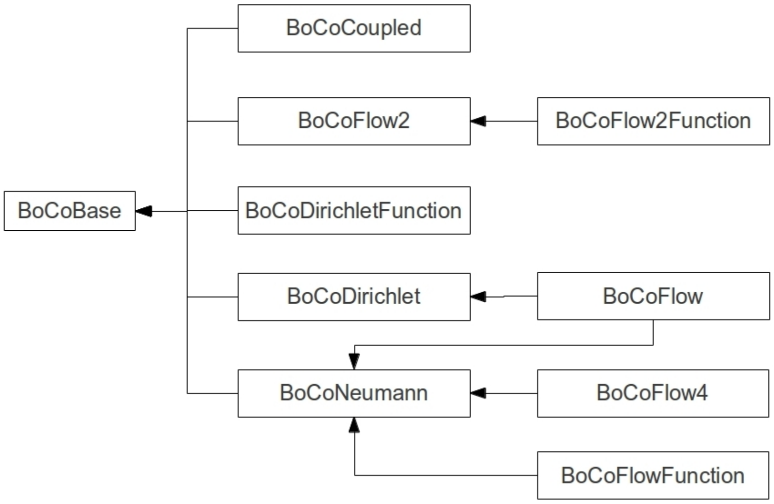

Figure 2.31: Inheritance diagram for BocoBase class of TermoFluids software.

the design, implementation, testing and validation of a fully three dimensional periodic boundary condition.

The Poisson equation, which arises from the incompressibility constraint and has to be solved at least once per time step, is usually the most time consuming and difficult for parallelization of part of the algorithm. Therefore, TermoFluids already counted with a periodic boundary condition implemented which allow the user to significantly reduce the computational time for solving the Poison equation with a geometric discretization obtained by the uniform extrusion of generic 2D meshes. Periodic boundary conditions are imposed in the extrusion direction, thus the linear couplings of the Poisson equation in such direction results into circulant submatrices [39], Such boundary condition is named PERIODIC_FFT and it is used over bidimensional domains extruded along one periodical direction.

Periodic boundary condition is a good alternative for reducing the computational domain to the minimum size. It is commonly used when the analyzed flow case is known to have periodic behavior, i.e. the same flow features are found on related consecutive regions of the complete geometry. An illustrative example of a bidimensional mesh extruded in the periodic direction is shown in Fig. 2.32, such geometry could use the available PERIODIC_FFT boundary condition.

However, some domains may be periodic in more than one direction or in only

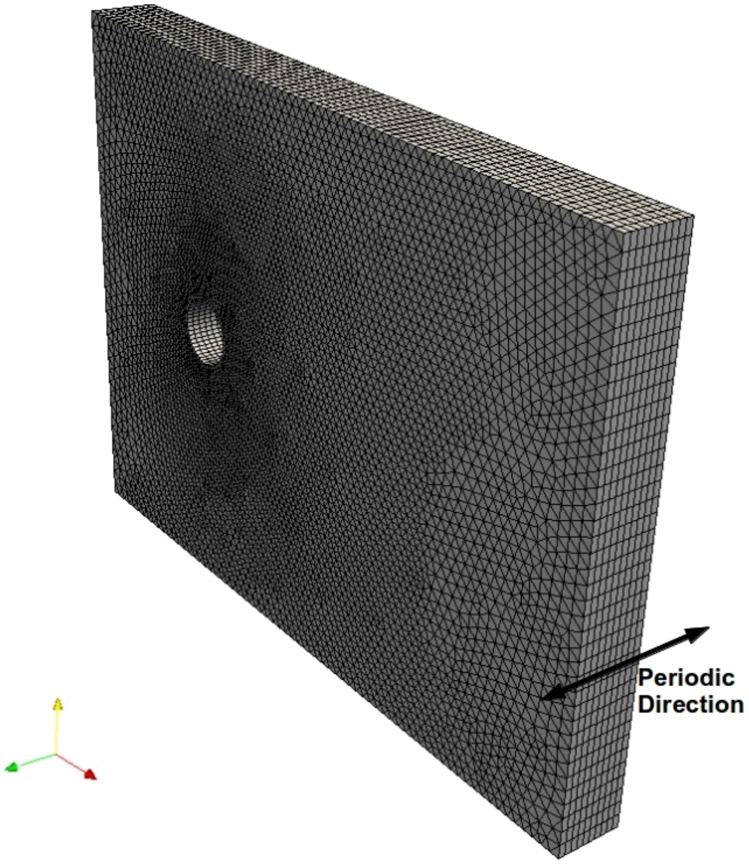

Figure 2.32: Three dimensional mesh around a cylinder. Mesh was generated by the extrusion of a bidimensional mesh.

one direction but with a geometry impossible to extrude. For example, if there is a bluff body between two periodic planes it is not possible to reproduce the same bidimensional mesh on the periodic direction. Fig. 2.33 illustrates an example of a fully three dimensional domain on which the PERIODIC_FFT condition would not be applicable.

At the pre-processing stage of the CFD simulation, the responsible tool of the set up of the periodic boundary condition needs to relate one periodic plane with the opposite periodic plane (we call them *bocoA* and *bocoB* respectively). Some geometric conditions need to be ensured in order to link each boundary node with its corresponding neighbor from the other periodic boundary. The mesh needs to have a perfect matching between two periodic boundaries, those boundaries need to have different boco identification numbers (*bocoId*) and the periodic planes need to be parallel to each other (see Fig. 2.34).

Broadly, the process consists in a loop going through the boundary nodes at *bocoA* and an internal secondary loop going through the boundary nodes at *bocoB*. The corresponding geometrical position is compared between each other, and if the components of the non periodic direction match in between the neighbor node has been found. To store this list of relationships, a map which links the global identification number (we call it *gid*) from *bocoA* with the *gid* of *bocoB*. Some additional information will be needed on the time-integration stage of the CFD simulation and it is stored in similar objects that can be called during the execution of the final transient code.

Aiming at maintaining the uniform structure of the general TermoFluids code, two important inline public functions were created:

- *getNbPerLid()* (indicating "get Neighbor Periodic Local ID"), on which the user enters a local identification number (*lid*) from one of the periodic boundaries and the function returns as result the corresponding *lid* of its neighbor at the contrary periodic boundary.

- *getNbPerPos* (indicating "get Neighbor Periodic Position), on which the user enters the *lid* of the node that is interested on obtaining its position. The position of that *lid* will be a D3 with the corresponding coordinates of its position.

2.4.2 Parallelization

TermoFluids is a parallel software that is persistently improving its capabilities trying to take advantage of the constantly growing computing power. Running the code in parallel is of major importance in order to divide the computational and memory requirements, specially for fully three dimensional simulations. Current supercomputers are composed of many net worked individual nodes, being each node itself an independent computer, most commonly with a multi-core processor. To

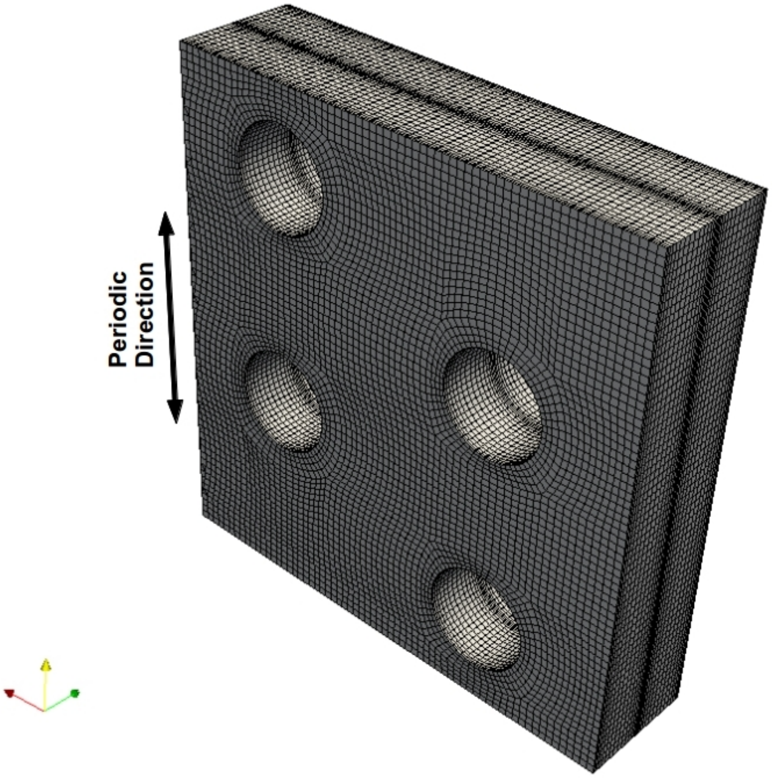

Figure 2.33: Three dimensional mesh around a characteristic part of a bank of cylinders.

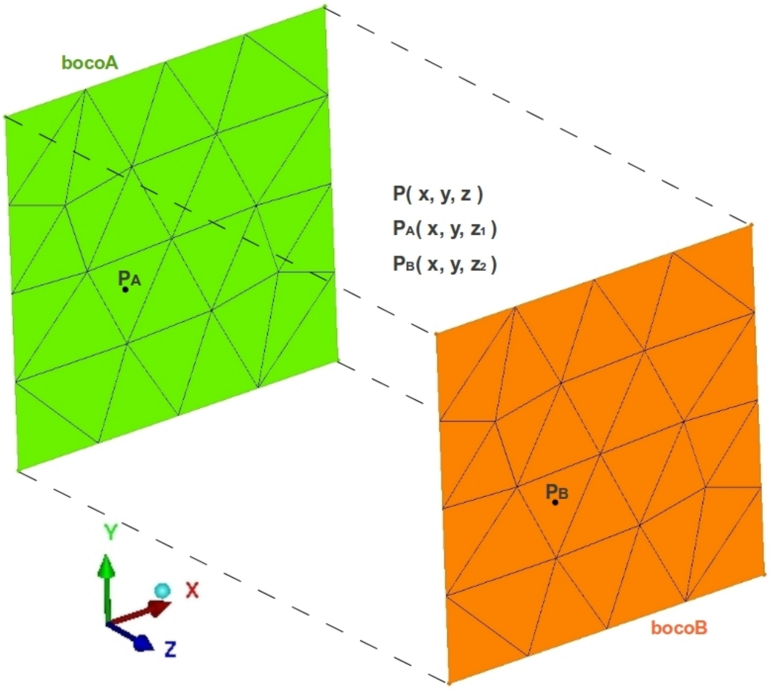

Figure 2.34: Schematic view of the geometric discretization of 3D periodic boundary condition. P_A is the neighbour of P_B and vice versa.

make processors located in different nodes working together, the distributed memory paradigm, based in message-passing, becomes indispensable. The libraries of TermoFluids are implemented using the Message Passing Interface (MPI) standard, chich makes the code portable across all distributed memory systems [38].

The user is not able to determine how the partition of the mesh is done, resulting on a great number of possible different partition distributions for the same mesh. At the second phase of the simulation (time-integration) the pressure, velocity and temperature equations must be solved and at the periodic boundary faces some information from the corresponding neighbor node will be need. If that neighbour node is not stored at the same processor, then communication routines should be applied.

The implementation of the 3D periodic boundary condition included the parallelization of the tool which will be briefly explained in this section. Two main routines have been used for the necessary communications, i.e. MPI_ALLREDUCE and MPI_ALLGATHERV.

MPI_ALLREDUCE

Consists in a function that performs a global reduction operation that returns the result to all processes in the group. MPI requires that all processes participating in the operation receive identical results. The message argument is written as follows:

MPI_ALLREDUCE (sendbuf, recvbuf, count, datatype, op, comm)

where *sendbuf* is an input that indicates the address of send buffer, *recvbuf* is an output that indicates the adress of receive buffer, *count* is an input that indicates the number of elements in send buffer, *datatype* is an input that indicates the data type of elements of send buffer, *op* is an input indicating the operation to be performed and *comm* is an input used as communicator.

The result of the operation appears in the receive buffer of all the group members. For the particular case of this section, the periodic boundary condition, the operation performed is a sumatory. The MPI_ALLREDUCE routine is used twice, to count the total number of nodes at each periodic boundary (*bocoA* and *bocoB*), all the processors will know the size of the receive vector.

Fig. 2.35 illustrates the global reduction made by the routine. The symbol ”o” represents the reduction operator (SUM for this case). The circles represent processes with ranks as shown. The small boxes represent buffer space and the letters represent data items. After the routine call, the dark-shaded boxes represent the result on all processes.

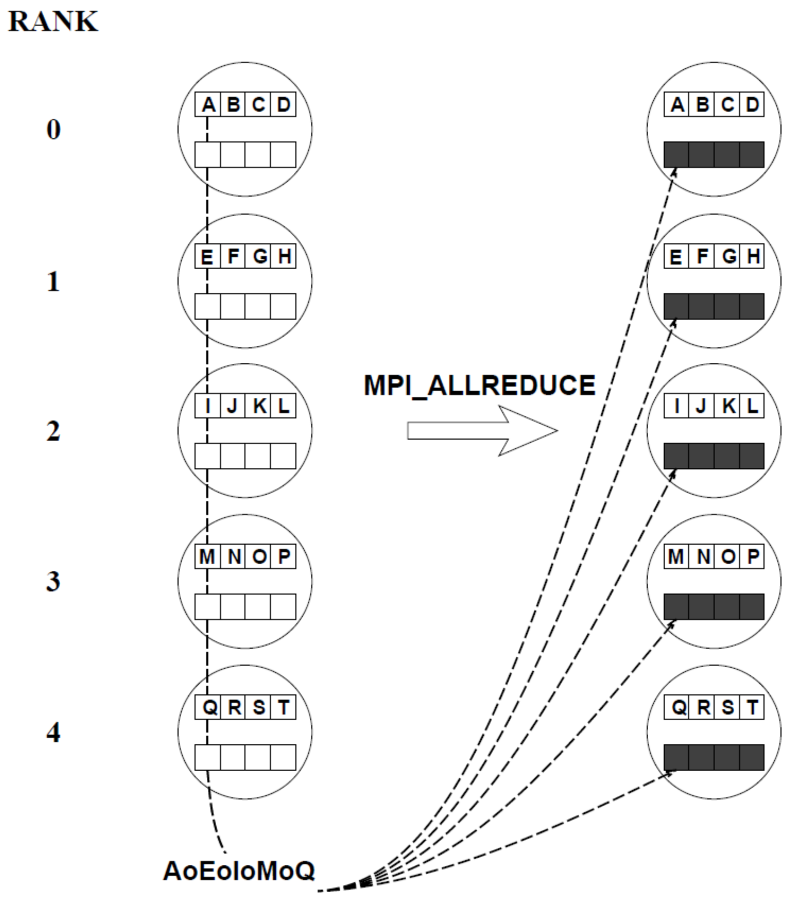

Figure 2.35: Global reduction in MPI_ALLREDUCE [40].

MPI_ALLGATHERV

There are some routines that distribute and re-distribute data wihtout performing any operation on the data. The routine named MPI_ALLGATHER is one of those functions and it does not have a specified root process. Send and receive details are significant on all processes and can be different, so are both specified in the argument lists. MPI_ALLGATHERV is an augmented version of the MPI_ALLGATHER function. The message argument is written as follows:

MPI_ALLGATHERV (sendbuf, sendcount, sendtype, recvbuf, recvcount, displs, recvtype, comm)

where *sendbuf* is an input that indicates the adress of send buffer, *sendcount* is an input that indicates the number of elements in send buffer, *sendtype* is an input that indicates the data type of elements of send buffer, *recvbuf* is an output that indicates the address of receive buffer, *recvcount* is an input that indicates the number of elements in the receive buffer, *displs* is an input that indicates the displacements, so that the data to be gathered lie contiguously in the root process memory space, *recvtype* is an input that indicates the data type of elements of receive buffer and *comm* is an input used as communicator.

The result of this operation is intended to have general information at all the processes included in the group. For this particular case of periodic boundary condition, every processor will know the macro vector composed by, for example, all the global identification numbers *gid* of the nodes composing each periodic boundary (*bocoA* and *bocoB*). More information besides *gid* is communicated for this purpose, like the global identification numbers of the cell to which the boundary face is linked, the coordinates of the face nodes and the position of the cell nodes.

Fig. 2.36 illustrates the gatherv operation. The circles represent processes with ranks as shown. The small boxes represent buffer space and the letters represent data items. Receive buffers are represented by the empty boxes on the left side of the figure (*before*), send buffers by the full boxes.

2.4.3 Validation

A bidimensional periodic boundary condition (boco PERIODIC2D) was already implemented on the TermoFluids software. A direct Schur complement based decomposition (DSD) algorithm in conjunction with a fast Fourier transform (FFT) was successfully used to perform DNS/LES simulations on general unstructured grids and modern supercomputers [39, 41–44]. The three dimensional periodic boundary condition (boco PERIODIC) implemented as a necessary tool for the development of the present doctoral thesis was validated by comparing the results against the bidimensional periodic boundary.

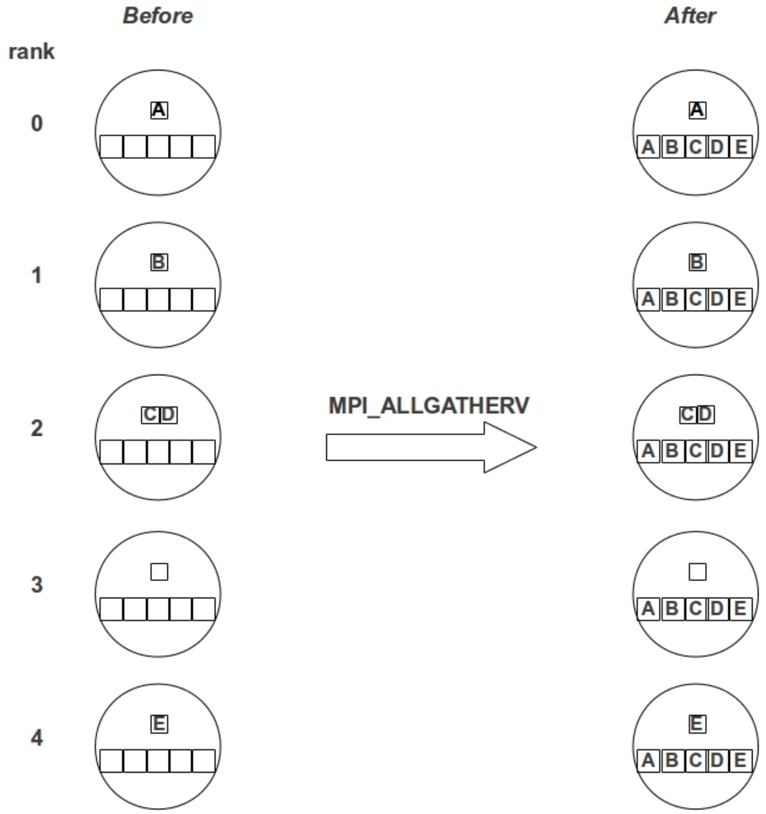

Figure 2.36: Global distribution and re-distribution involved in MPI_ALLGATHERV [40].

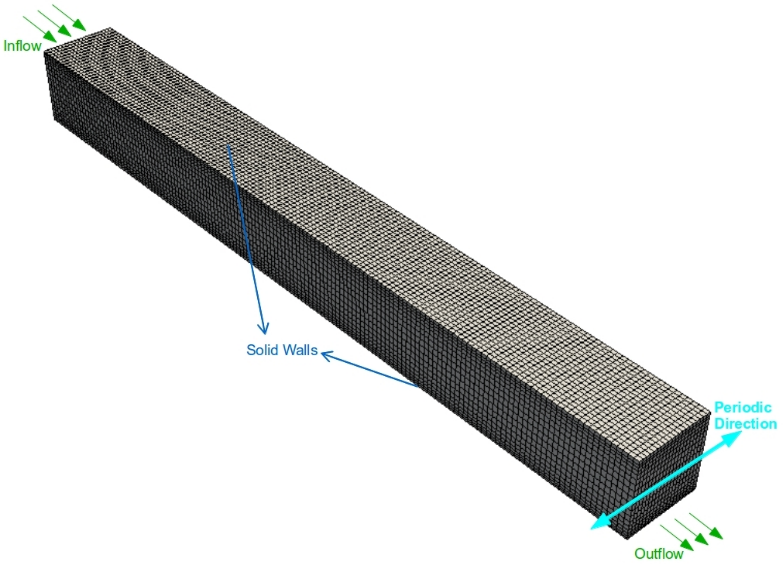

Figure 2.37: Parallel plates geometry for validation of three dimensional periodic boundary condition.

Simple channel flow was simulated for different Reynolds numbers. Uniform velocity profile at the entrance was set as the inlet boundary with isothermal temperature for air flow between isothermal solid parallel plates (with no-slip condition). Cooling of air was simulated $T_{in} = T_{air} = T_H$ (where subscript H denotes for HOT) and the parallel plates have the same cold constant temperature, $T_{wall} = T_C$ (where subscript C denotes for COLD). Fig. 2.37 represents the characteristic geometry selected for the benchmark cases. Axis *z* is where the periodic direction is imposed and 20 planes are equally spaced along a vector of magnitude five.

Some hydrodynamic and thermal dimensionless parameters like $P/\rho {u_{in}}^2$, u/u_{in} and $(T - T_C)/(T_H - T_C)$ are illustrated in Fig. 2.38. The boundary condition represents the same flow characteristic in both periodic treatments. By consequence, the same dimensionless profiles are found for PERIODIC2D and PERIODIC bocos respectively.

Three dimensional temperature and velocity distributions are shown in Fig. 2.39, the flow is cooled along the channel which is a characteristic part of a bigger (wider) domain. It represents the flow along infinite plates on the spanwise direction.

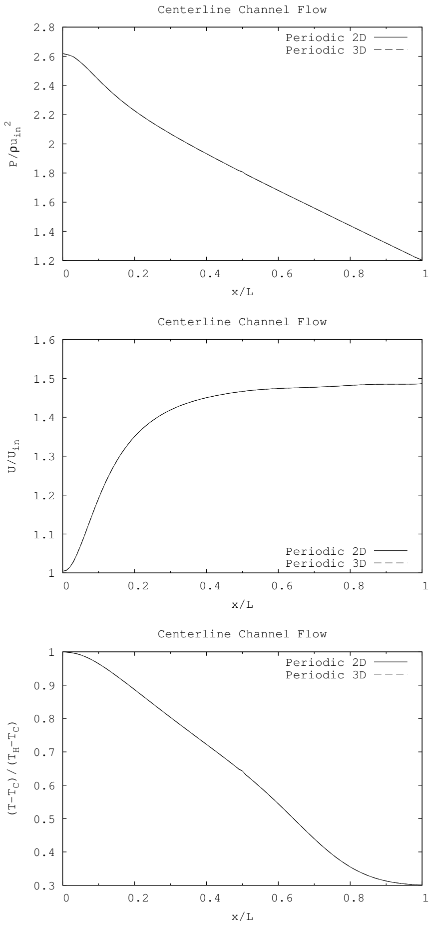

Figure 2.38: Validation of three dimensional periodic boundary condition with typical dimensionless parameters. Bidimensional periodic boundary condition was used as benchmark.

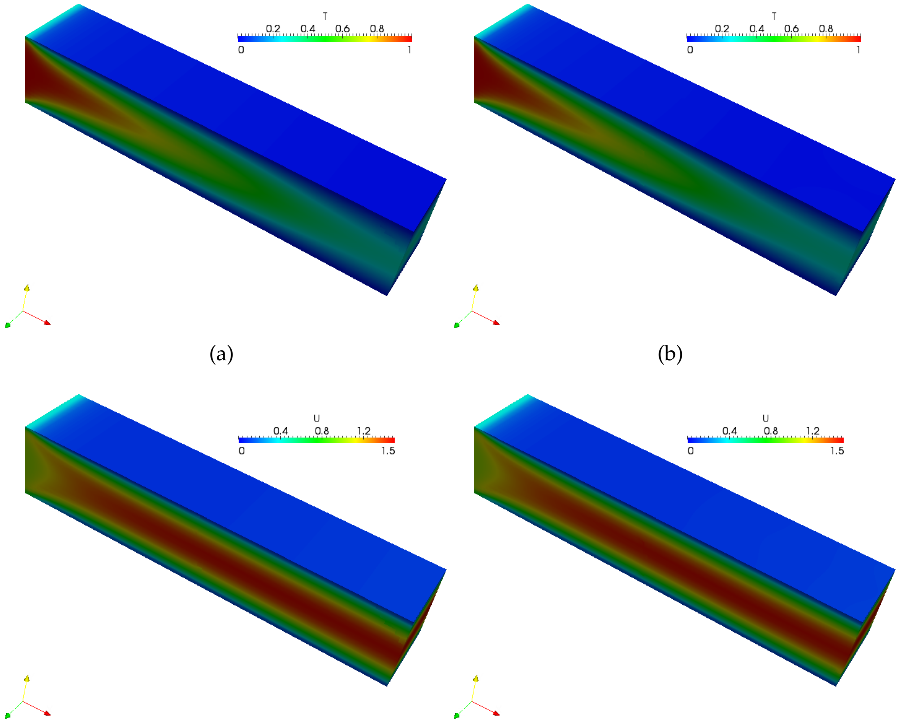

(a) (b)

(c) (d)

Figure 2.39: Three dimensional views of a periodic channel. Left: boco PERIODIC2D, right: boco PERIODIC. Top: temperature distribution, bottom: velocity distribution.

2.5 Conjugated problems

Thermal engineering works to solve problems that concern the generation, use, and exchange of thermal energy and heat between physical systems. Conjugate heat transfer problems are found in many practical applications in which heat conduction in a solid domain is intimately related with the convection heat transfer in an adjacent fluid domain. Some of the potential applications include air conditioning, refrigeration, building heating, defrost, cooling of electronic equipments among others.

The first stage of the turbine and the combustor of an aircraft engine are typical examples because they are subjected to high heat transfer rates with the surrounding hot gases. The turbine gases have temperatures that are mostly above the melting point of the alloys employed for the solid components, which can survive only because of the application of advanced cooling systems and metal coatings. Thus an accurate prediction of the solid temperature is essential to properly estimate the life expectations of these components.

The ″conjugate simulation″ of fluid heat transfer and solid heat conduction will be considered aiming at preserving the real conditions of the industrial applications that will be studied. By coupling both fluid and solid solvers, the investigation of ″conjugate heat transfer″ in both domains will be reached at the same time.

Particularly the conjugated heat transfer process is treated in the TermoFluids software by incorporating a solver for the temperature field in the solid domain linked with the existing fluid dynamics libraries. This links are managed by a recently added library called “NEST” which is designed to methodically connect different solvers to treat diverse kind of thermal issues such as conduction, radiation, combustion and more [45].

This linkage demands an interpolating procedure to communicate information from the solid to the fluid and vice versa through the common interface between both domains. To keep high accuracy, the approach needs that the two domains share the same faces at the interface boundaries (to avoid approximation errors introduced by the interpolation procedure). To ensure a simple and accurate matching between meshes, the same grid generator ANCYS-ICEM CFD.

2.5.1 Validation of coupling domains

The code that is intended to be used on complex geometries with interacting thermophysics in different domains is validated by solving the conjugate natural convection in a square cavity with a conducting side wall for which benchmark data from Hribersek and Kuhn [46] is available. The cavity is heated at the left (solid wall) and cooled at the right side, all the other boundaries are considered adiabatic. All

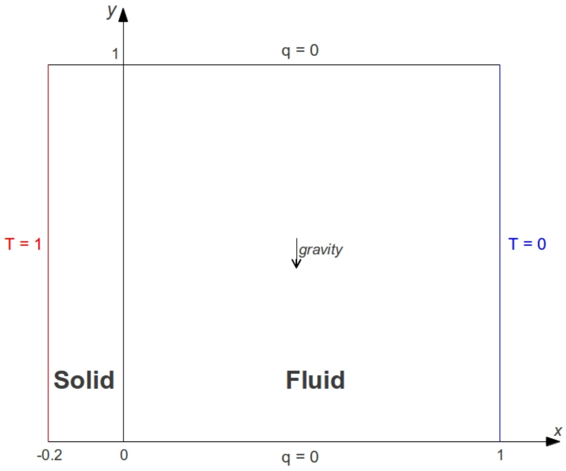

Figure 2.40: Conjugate natural convection problem.

boundaries represent solid walls, thus no-slip velocity boundary condition is set (see Fig. 2.40).

The computational mesh consists on 10×50 CV in the solid domain with exponential densification close to the interface with the fluid domain which has 60×50 CV with hyperbolic densification close to the vertical walls. The working fluid is air with $Pr = 0.721$. The test case is of Rayleigh number of 71000. The thermal conductivity ratio $K = \lambda_{solid}/\lambda_{fluid}$ of 1 and 10 are compared with the benchmark corresponding case.

Fig. 2.41 presents the temperature distribution in both domains, and good consistency of the profile is observed. Also a smooth transition from one domain (solid) to the other (fluid) is perceived, which indicates a good coupling and communication of data at the interface. It is worth to mention that qualitative comparison with the benchmark case is in good agreement.

Local comparison of temperature distribution along the interface center line is shown in Fig. 2.42. This local distribution present very good agreement with the benchmark data for both ratios of thermal conductivity which validates the adequate performance of the coupling and conjugated code to be used on different problems like the applications motivating this thesis.

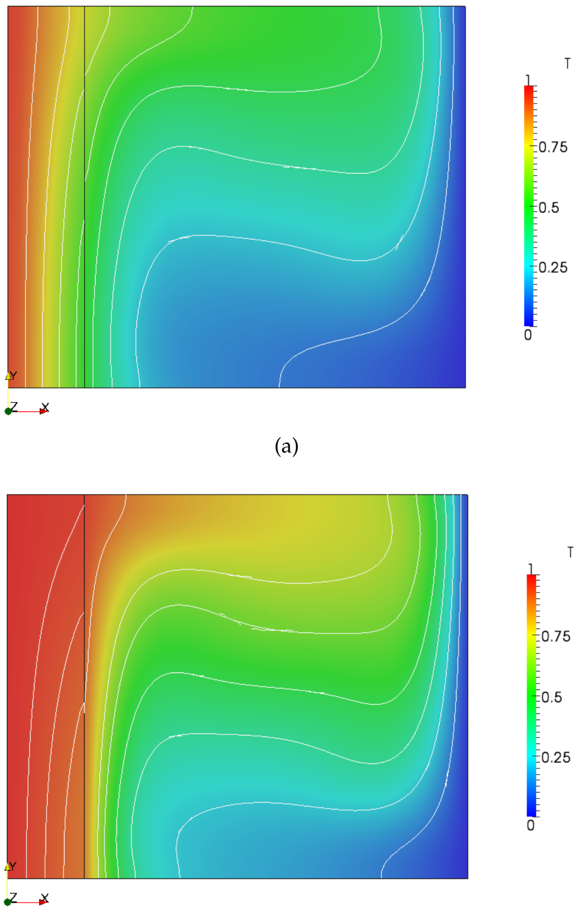

(a)

(b)

Figure 2.41: Temperature contours for a) $K = 1$ and b) $K = 10$.

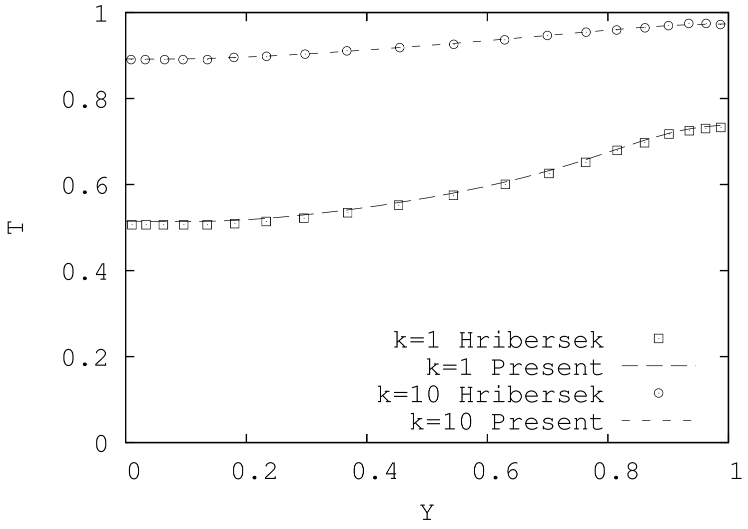

Figure 2.42: Temperature distribution along the solid-fluid interface for different K.

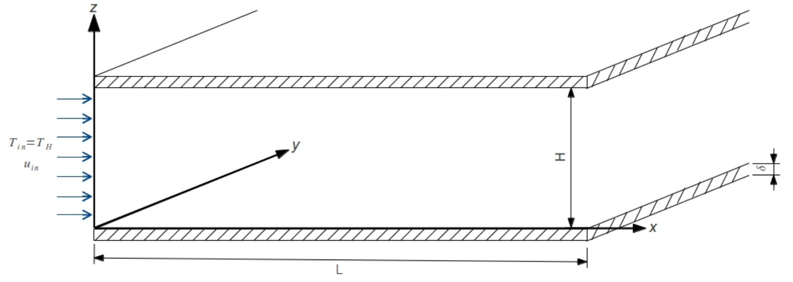

Figure 2.43: Schematic representation of the flow between horizontal parallel plates.

2.5.2 Dimensionless approach

A first attempt of conjugated simulation was made using a realistic set up of the case. This is, that constant thermophysical properties were imposed for the fluid (working fluid was air) and solid (aluminum fins) domains respectively. However, the combination of the thermal performance of the real case and the small discretization needed to adequately solve the boundary layer near the solid walls, the time step was of the order of 1×10^{-7}.

For the previous experience simulating similar fluid flows around a confined tube bundle, it is known that a typical CFD simulation with constant wall temperature as boundary condition can use more than 1200 time units to converge. Since about ten iterations of the conjugated problem take about one second to be completed (handing 35000 CVs per core), it would take an excessive unaffordable amount of time to complete only one simulation.

Based on the above mentioned data, the author performed a dimensional study trying to control the critical parameters and increase the dominant time step of the transitory simulation. The definition of the dimensionless parameters for a simple channel flow (Fig. 2.43) are defined on the following equations (2.26):

$$\overline{X} = \frac{x}{L_c} \tag{2.26}$$

$$\overline{Y} = \frac{y}{L_c} \tag{2.27}$$

$$\overline{Z} = \frac{z}{L_c} \tag{2.28}$$

$$\theta = \frac{T - T_C}{T_H - T_C} \tag{2.29}$$

$$\overline{P} = \frac{P + \rho g L_c}{\rho {u_c}^2} \tag{2.30}$$

$$\overline{U} = \frac{u}{u_c} \tag{2.31}$$

$$\overline{V} = \frac{v}{u_c} \tag{2.32}$$

$$\overline{W} = \frac{w}{u_c} \tag{2.33}$$

$$\bar{t} = \frac{t\alpha_f}{{L_c}^2} \tag{2.34}$$

where x,y and z are the Cartesian coordinates, $L_c = 2H$ is the characteristic length, T_C is cold temperature, T_H is hot temperature, ρ is the density of the fluid, g is the gravity, u_c is the characteristic velocity and α is the thermal diffusivity (subscript f holds for fluid domain) defined in Eq. 2.35.

$$\alpha = \frac{\lambda_f}{(\rho c_p)_f} \tag{2.35}$$

Dimensionless Navier Stokes equations used for the fluid domain are written hereafter (Eq. 2.36):

$$\frac{\partial \overline{U}}{\partial \overline{X}} + \frac{\partial \overline{V}}{\partial \overline{Y}} + \frac{\partial \overline{W}}{\partial \overline{Z}} = 0 \tag{2.36}$$

$$\frac{1}{Pe}\frac{\partial \overline{U}}{\partial \bar{t}} + \overline{U}\frac{\partial \overline{U}}{\partial \overline{X}} + \overline{V}\frac{\partial \overline{U}}{\partial \overline{Y}} + \overline{W}\frac{\partial \overline{U}}{\partial \overline{Z}} = \frac{1}{Re}[\frac{\partial^2 \overline{U}}{\partial \overline{X}^2} + \frac{\partial^2 \overline{U}}{\partial \overline{Y}^2} + \frac{\partial^2 \overline{U}}{\partial \overline{Z}^2}] - \frac{\partial \overline{P}}{\partial \overline{X}} \tag{2.37}$$

$$\frac{1}{Pe}\frac{\partial \overline{V}}{\partial \bar{t}} + \overline{U}\frac{\partial \overline{V}}{\partial \overline{X}} + \overline{V}\frac{\partial \overline{V}}{\partial \overline{Y}} + \overline{W}\frac{\partial \overline{V}}{\partial \overline{Z}} = \frac{1}{Re}[\frac{\partial^2 \overline{V}}{\partial \overline{X}^2} + \frac{\partial^2 \overline{V}}{\partial \overline{Y}^2} + \frac{\partial^2 \overline{V}}{\partial \overline{Z}^2}] - \frac{\partial \overline{P}}{\partial \overline{Y}} \tag{2.38}$$

$$\frac{1}{Pe}\frac{\partial \overline{W}}{\partial \bar{t}} + \overline{U}\frac{\partial \overline{W}}{\partial \overline{X}} + \overline{V}\frac{\partial \overline{W}}{\partial \overline{Y}} + \overline{W}\frac{\partial \overline{W}}{\partial \overline{Z}} = \frac{1}{Re}[\frac{\partial^2 \overline{W}}{\partial \overline{X}^2} + \frac{\partial^2 \overline{W}}{\partial \overline{Y}^2} + \frac{\partial^2 \overline{W}}{\partial \overline{Z}^2}] - \frac{\partial \overline{P}}{\partial \overline{Z}} \tag{2.39}$$

$$\frac{1}{Pr}\frac{\partial \theta}{\partial \bar{t}} + Re[\overline{U}\frac{\partial \theta}{\partial \overline{X}} + \overline{V}\frac{\partial \theta}{\partial \overline{Y}} + \overline{W}\frac{\partial \theta}{\partial \overline{Z}}] = \frac{1}{Pr}[\frac{\partial^2 \theta}{\partial \overline{X}^2} + \frac{\partial^2 \theta}{\partial \overline{Y}^2} + \frac{\partial^2 \theta}{\partial \overline{Z}^2}] \tag{2.40}$$

The solid domain is defined by the following dimensionless Eq. 2.41:

$$\frac{\partial^2 \theta}{\partial \overline{X}^2} + \frac{\partial^2 \theta}{\partial \overline{Y}^2} + \frac{\partial^2 \theta}{\partial \overline{Z}^2} = \frac{\alpha_f}{\alpha_s}\frac{\partial \theta}{\partial \overline{t}} \tag{2.41}$$

The problem is fully defined with the appropriate boundary conditions, which in dimensionless form read as follows (Eqs. 2.42 to 2.51):
At $\overline{Z} = 0$ and $\overline{Z} = 1$ for the range $0 \leq \overline{X} \leq \frac{L}{L_c}$:

$$\theta_s = \theta_f \tag{2.42}$$

$$\lambda_{sf}\frac{\partial \theta_s}{\partial \overline{Z}} = \frac{\partial \theta_f}{\partial \overline{Z}} \tag{2.43}$$

$$\overline{U} = 0 \tag{2.44}$$

$$\overline{V} = 0 \tag{2.45}$$

$$\overline{W} = 0 \tag{2.46}$$

where $\lambda_{sf} = \frac{\lambda_s}{\lambda_f}$, subscript f holds for fluid and s for solid. Then, at $\overline{X} = 0$ for the range $0 \leq \overline{Z} \leq 1$:

$$\overline{U} = 1 \tag{2.47}$$

$$\overline{V} = 0 \tag{2.48}$$

$$\overline{W} = 0 \tag{2.49}$$

$$\frac{\partial \overline{P}}{\partial \overline{Z}} = 0 \tag{2.50}$$

At $\overline{X} = \frac{L}{LC}$ for the range $0 \leq \overline{Z} \leq 1$:

$$\frac{\partial \overline{P}}{\partial \overline{X}} = 0 \tag{2.51}$$

It is well known that as long as the characteristic dimensionless numbers are kept constant, different thermophysical properties can be used for the fluid or solid domains and the flow features will be equivalent. Aiming at increasing the time step for the simulation of conjugated heat transfer over plate fin and tube heat exchangers, the fluid and solid thermophysical properties were set as explained in Fig. 2.44. This way, the time step is increased from 1.0×10^{-7} with real air-aluminum properties, to 1.0×10^{-4} with modified fluid-solid properties. Furthermore, the advantage of this strategy comes not only from the significant increase of the time step, but also comes from the fact that adapting the thermophysical properties the user can modify the thermal behavior of the fluid and achieve the convergence faster.

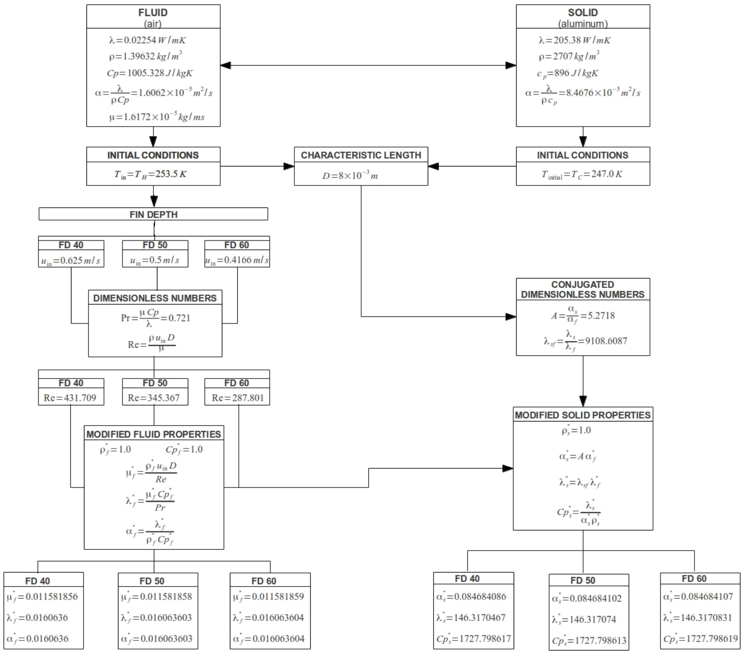

Figure 2.44: Schematic dimensionless analysis of the conjugated heat transfer problem.

dt	Set tolerance	Time
1.0	1.0×10^{-10}	7.896 min
1.0×10^{-3}	1.0×10^{-10}	+2 days
1.0×10^{-3}	1.0×10^{-5}	32.436 min
1.0×10^{-4}	1.0×10^{-5}	32.614 min

Table 2.4: Solid time step assessment for heat conduction simulation over a perforated fin.

2.5.3 Coupling different time steps

The solver used to simulate the solid domain is an implicit model. If the simulation consisted only in solid regions, the time step imposed for a similar geometrical configuration would be much bigger than the conjugated one. However, for the convection and conduction problem, the convection will impose a small time step according to the fluid needs.

Simulating only the solid domain allowed the author to perform a time assessment for the influence of the time step imposed to the heat conduction equation solver. Table 2.4 presents the details of this assessment, the simulations were executed using a structured mesh composed by 94656 CV partitioned in 64 cores. The results show that the solid will converge relatively fast (7.8 minutes) if a coherent high time step is imposed ($dt = 1.0$). However, if the time step is decreased, the time to achieve the same level of accuracy is much higher.

Attempting to save computational costs on unnecessary communications between domains and to help the convergence of the solid solver, the fluid domain is forced to work within an internal loop to accumulate heat until the sum of fluid time steps is of the order of one solid coherent time scale. The boundary condition at the interface is the last temperature profile sent by the solid domain during the internal fluid loop, and it is updated with the new temperature profile sent by the solid once the time scales have the same order of magnitude. The fluid sends to the solid domain the accumulated heat flux of the internal fluid loop and it is used as boundary condition at the interface for the solid region. Fig. 2.45 synthesize the main steps required by the conjugated heat transfer problem with communication between domains every time step and with an internal fluid loop to accumulate heat.

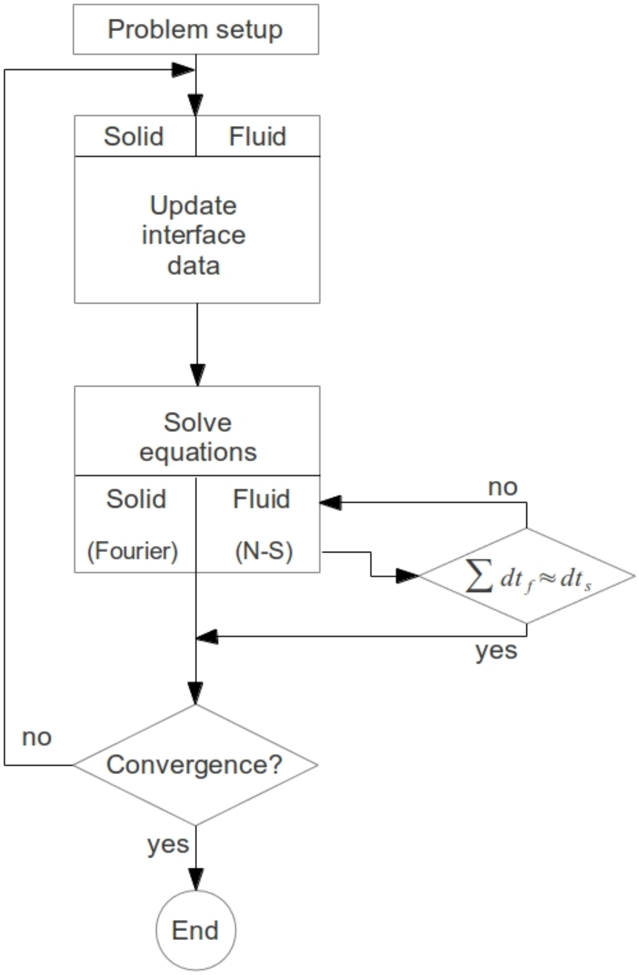

Figure 2.45: Schematic conjugated heat transfer procedure with an internal fluid loop to accumulate heat and equate domains time scales.

2.6 Concluding remarks

A general approach for the high-end numerical simulation of heat exchangers used on the refrigeration industry has been presented. The complete process can be divided into smaller sections where special attention should be paid (mesh generation, reduction of the domain using periodic boundary conditions, and analysis of conjugated heat transfer coupling different domains). First, once the real geometry of the heat exchanger is selected, a proper mesh design is needed. After analyzing different mesh strategies and categories available on the grid generation software (ANSYS ICEM-CFD) in conjunction with the physical behavior of the flow passing through the domain, it has been determined that the use of unstructured meshes could lead to unrealistic flow prediction of the boundary layer around curved surfaces (like the tubes present in a fin and tube heat exchanger) if the flow is found to be turbulent. Furthermore, a smooth grow of the CV sizes is desirable in order to obtain acceptable mesh quality. In this respect, unstructured meshes with prismatic cells on the region close to the curved solid surfaces might be too expensive on the final computational time needed. This is because the prismatic CVs are intended to adequately solve the boundary layer around cylinders, but depending on the Reynolds number this region may be very small and at least three CVs would be used for that purpose. However for laminar flows it is affordable to build a good mesh around curved surfaces with unstructured meshes and its advantages can be very useful as well. In order to have a good approximation of the boundary layer around curved surfaces and generate affordable meshes at the same time, structured body fitted meshes are proposed for turbulent flow regimes.

The numerical simulation of a heat exchanger (with complex geometry) is a very challenging issue if high level tools (like LES) are to be used. As aforementioned, the meshes can be very big (with several millions of CVs) due to the complex flow features that need to be captured by the simulation. Hence, an alternative to reduce the size of the computational domain is always helpful. Evaporator heat exchangers are usually composed by a large matrix of tubes with multiple fins mounted on the normal direction. If the matrix is big enough, the flow tend to have a periodic behavior on the transversal direction. Once the size of the periodic domain is identified, the final computational domain can be reduced by using periodic boundary conditions at the transversal planes. This reduction has shown to have great impact on the computational costs and it definitely increase the possibilities of alternative geometries to be studied using the tools that have been implemented.

Finally, since the heat exchanger is largely composed by solid walls it is relevant to study the conjugated heat transfer problem. Solving the energy equation not only on the fluid domain, but also on the solid regions in order to have more realistic approximation of the flow and heat transfer features. Different contributions have been made to the existing NEST code on the CTTC for the simulation of industrial devices under real conditions. Such contributions are important because by understanding the particular characteristics of this applications, the capabilities of the code are expanded to work with the refrigeration industry partners.

References

[1] J. Barbosa, C. Hermes, and Melo C. CFD Analysis of tube-fin 'no-frost' evaporators. *J. of the Braz. Soc. of Mech. Sci. & Eng.*, 32(4):445–453, 2010.

[2] O. Lehmkuhl, C.D. Pérez-Segarra, R. Borrell, M. Soria, and A. Oliva. TERMOFLUIDS: A new parallel unstructured CFD code for the simulation of turbulent industrial problems on low cost PC cluster. *In Proceedings of the Parallel CFD 2007 Conference*, pages 1–8, 2007.

[3] G. Delibra, D. Borello, K. Hanjalić, and F. Rispoli. URANS of flow and endwall heat transfer in a pinned passage relevant to gas-turbine blade cooling. *Int. J. Heat Fluid Flow*, 30:549–560, 2009.

[4] G. Delibra, K. Hanjalić, D. Borello, and F. Rispoli. Vortex structures and heat transfer in a wall-bounded pin matrix: LES with a RANS wall-treatment. *Int. J. Heat Fluid Flow*, 31:740–753, 2010.

[5] W. J. Minkowycz, J. P. Abraham, and E. M. Sparrow. Numerical simulation of laminar breakdown and subsequent intermittent and turbulent flow in parallel-plate channels: Effects of inlet velocity profile and turbulence intensity. *Int. J. of Heat and Mass Transfer*, 52:4040–4046, 2009.

[6] I. Rodríguez, O. Lehmkuhl, R. Borrell, L. Paniagua, and C. D. Pérez-Segarra. High Performance Computing of the flow past a circular cylinder at critial and supercritical Reynolds numbers. *Procedia Engineering. Parallel Computational Fluid Dynamics Conference (ParCFD2013)*, 61:166–172, 2013.

[7] J. D. Anderson Jr. Ludwig Prandtl's Boundary Layer. *American Institute of Physics*, pages 42–48, 2005.

[8] L. Prandtl. Über Flüssigkeitsbewegung bei sehr kleiner Reibung (On the motion of fluids of very small viscosity). *Third International Congress of Mathematicians.*, 1905.

[9] H. Schlichting. *Boundary-Layer Theory*. McGrawHill, New York., 1955.

[10] P. M. Gerhart, R. J. Gross, and J. I. Hochstein. *Fundamentals of Fluid Mechanics*. Addison-Wesley Publishing Company, 1992.

[11] B. Weigand. *Analytical Methods for Heat Transfer and Fluid Flow Problems*. Springer, 2004.

[12] L. Schiller. Die Entwicklung der laminaren Geschwindigkeitsverteilung und ihre Bedeutung für Zähigkeit Messungen (The development of the laminar velocity distribution and its significance for resistance measurements). *Angew. Math. Mech.*, 2:96–106, 1922.

[13] M. Van Dyke. Entry flow in a channel. *J. Fluid Mech.*, 44:813–823, 1970.

[14] Y. L. Wang and P. A. Longwell. Laminar flow in the inlet section of parallel plates. *AIChEJ.*, 10:313–317, 1964.

[15] J. R. Bodoia. *The Finite Difference Analysis of Confined Viscous Flows*. Ph.D. Thesis. Carnegie Institute of Technology, Pittsburgh, Pennsylvania, 1959.

[16] J. Liu. *Flow of a Bingham Fluid in the Entrance Region of an Annular Tube*. M.S. Thesis. University of Wisconsin-Milwaukee, 1974.

[17] B. Atkinson, M. P. Brocklebank, C. C. H. Card, and J. M. Smith. Low Reynolds number developing flows. *AIChE J.*, 15:548–553, 1969.

[18] R. K. Shah and A. L. London. *Laminar flow forced convection in ducts*. Academic Press, Inc., 1978.

[19] G. M. Brown. Heat or mass transfer in a fluid in laminar flow in a circular or flat conduit. *AIChE J.*, 6:179 –183, 1960.

[20] J. R. Sellers, M. Tribus, and J. S. Klein. Heat transfer to laminar flow in a round tube or flat conduit - the Graetz problem extended. *Transactions of ASME*, 78:441–448, 1956.

[21] R. K. Shah. Thermal entry length solutions for the circular tube and parallel plates. *Proc. Natl. Heat Mass Transfer Conf., 3rd Indian Inst. Technol. Bombay*, 1:HMT–11–75, 1975.

[22] E. M. Sparrow. Analysis of laminar forced-convection heat transfer in entrance region of flat rectangular ducts. *NACA Tech. Notes*, TN3331, 1955.

[23] K. Stephan. Wärmeübergang und druckabfall nicht ausgebildeter Laminare Strömung in Rohren und in ebenen Spalten. (Heat transfer and pressure drop laminar flow in pipes and in planar ducts). *Chem.-Ing.-Tech.*, 31:773–778, 1959.

[24] C. L. Hwang and Fan. L. T. Finite difference analysis of forced convection heat transfer in entrance region of a flat rectangular duct. *Appl. Sci. Res. Sect. A*, 13:401–422, 1964.

[25] T. V. Nguyen and I. L. Maclain-cross. Simultaneously developing, laminar flow, forced convection in the entrance region of parallel plates. *Journal of Heat Transfer*, 113:837–842, 1991.

[26] R. I. Bowles. Transition to turbulent flow in aerodynamics. *Phil. Trans. R. Soc. Lond.*, 358:245–260, 2000.

[27] S. J. Davies and C. M. White. An Experimental Study of the Flow of Water in Pipes of Rectangular Section. *Proc. R. Soc. Lond.*, 119A:92–107, 1928.

[28] R. J. Cornish. Flow in a Pipe of Rectangular Cross Section. *Proc. R. Soc. Lond.*, 120A:691–700, 1928.

[29] J. Allen and N. D. Grundberg. The Resistance to the Flow of Water Along Smooth Rectangular Passages and the Effect of a Slight Convergence or Divergence of the Boundaries. *Phil. Mag.*, 23:490–503, 1937.

[30] R. R. Rothfus, R. I. Kermode, and J. H. Hackworth. Pressure Drop in Rectangular Ducts. *Chem. Eng.*, 71:175–176, 1964.

[31] C. H. K. Williamson. Vortex dynamics in the cylinder wake. *Annual Review of Fluid Mechanics*, 28:477–539, 1996.

[32] A. Prasad and C. H. K. Williamson. The instability of the separated shear layer from a bluff body. *Phys. Fluids*, 8:1347, 1996.

[33] O. Lehmkuhl, R. Borrell, C. D. P'erez-Segarra, J. Chiva, and A. Oliva. Direct Numerical Simulations and Symmetry-Preserving Regularization Simulations of the flow around a circular cylinder at Reynolds number 3900. *Turbulence, Heat and Mass Transfer 6*, 2009.

[34] A. Roshko. Experiments on the flow past a circular cylinder at very high Reynolds number. *Journal of Fluid Mechanics*, 10:345–356, 1961.

[35] E. Achenbach and E. Heinecke. On vortex shedding from smooth and rough cylinders in the range of Reynolds numbers $6x10^3$ to $5x10^6$. *Journal of Fluid Mechanics*, 109:239–251, 1981.

[36] F. M. White. *Viscous, Fluid Flow*. McGraw-Hill, New York., 1974.

[37] P. Bearman. On vortex shedding from a circular cylinder in the critical Reynolds number regime. *J. Fluid Mech.*, 37:577–585, 1969.

[38] Ricard Borrell Pol. *Parallel algorithms for Computational Fluid Dynamics on unstructured meshes*. Ph.D. Thesis. Universitat Politécnica de Catalunya (UPC), Terrassa, Barcelona. Spain, 2012.

[39] R. Borrell, O. Lehmkuhl, F. X. Trias, and A. Oliva. Parallel direct Poison solver for discretisations with one Fourier diagonalisable direction. *Journal of Computational Physics*, 230:4723–4741, 2011.

[40] N. MacDonald, E. Minty, T. Harding, and S. Brown. *Writing Message-Passing Parallel Programs with MPI. A two-day course*. Edinburgh Parallel Computing Centre. Course Notes.

[41] F. X. Trias, M. Soria, A. Oliva, and C. D. Pérez-Segarra. Direct numerical simulations of two- and three-dimensional turbulent natural convection flows in a differentially heated cavity of aspect ratio 4. *Journal of Fluid Mechanics*, 586:259–293, 2007.

[42] M. Soria, C. D. Pérez-Segarra, and A. Oliva. A direct parallel algorithm for the efficient solution of the pressure-correction equation of incompressible flow problems using loosely coupled computers. *Numerical Heat Transfer, Part B*, 41:117–138, 2002.

[43] F. X. Trias, M. Soria, C. D. Pérez-Segarra, and A. Oliva. A direct Schur-Fourier decomposition for the efficient solution of high-order Poisson equations on loosely coupled parallel computers. *Numerical Linear Algebra with Applications*, 13:303–326, 2006.

[44] F. X. Trias, R. W. C. P. Verstappen, A. Gorobets, M. Soria, and A. Oliva. Parameter-free symmetry-preserving regulatization modeling of a turbulent differentially heated cavity. *Computers and Fluids*, 39:1815–1831, 2010.

[45] J. Lopez, R. Lehmkuhl, O. Damle, and J. Rigola. A parallel and object-oriented general purpose code for simulation of multiphysics and multiscale systems. *24th International Conference on Parallel Computational Fluid Dynamics. "ParCFD 2012 Abstract Booklet*, pages 58–59, 2012.

[46] M. Hribersek and G. Kuhn. Conjugate heat transfer by boundary-domain integral method. *Engineering Analysis with Boundary Elements*, 24:297–305, 2000.

Chapter 3

Large Eddy Simulations (LES) on the Flow and Heat Transfer in a Wall-Bounded Pin Matrix

The contents of this chapter have been published as:

L. Paniagua, O. Lehmkuhl, C. Oliet, C. D. Pérez-Segarra. Large Eddy Simulations (LES) on the Flow and Heat Transfer in a Wall-Bounded Pin Matrix. *Numerical Heat Transfer, Part B: Fundamentals: An International Journal of Computation and Methodology*

Abstract. In this chapter, three-dimensional turbulent forced convection in a matrix of wall-bounded 8×8 cylindrical pins is studied. Large Eddy Simulations (LES) with three levels of grid refinement are performed for three distinct Reynolds numbers (3000, 10000 and 30000). Results are presented and compared with the available experimental data and numerical analysis previously reported in scientific literature. Three different subgrid-scale (SGS) models (WALE, QR and VMS) are compared on a local row-by-row study. For the hydrodynamic study, velocity and pressure coefficient local values are depicted. The thermal field is analyzed and validated with the time averaged Nusselt number present at the endwalls of the channel. Turbulence characteristics of the flow are well illustrated. Moreover, qualitative and quantitative study of heat transfer in this kind of equipments is presented. In general, the combination of the mathematical formulation, LES models and meshes used in this analysis, can successfully predict the flow features.

3.1 Introduction

Pin fin arrays are considered an enhanced geometry commonly used in a wide variety of applications ranging from HVAC&R heat exchangers, cooling of electronic equipments, automobile radiators or cooling of gas turbine airfoils. This kind of equipments have been used and investigated during decades because of their great impact on industry.

Configurations of pin fin geometries and fin and tube heat exchanger are very similar between each other on the external region where usually gas flows through the fins and pins or tubes. The difference relies more on the applications and the actual function of the device. For pin fin arrangements, the pins are considered to be the extended area and no fluid is inside of them. They are placed in order to increase the effective heat transfer area of the flow that is forced to pass between the fins to cool the turbine blade. On the contrary, the fins of fin and tube heat exchangers are the extended surfaces, fluid goes inside the tubes and it is intended to exchange energy with the external fluid. Aiming at increasing the heat transfer capacity of the equipment, fins (of different possible configurations) are placed across the tube bundle.

In compact heat exchangers, thermal resistance is usually higher on the gas side of the heat exchanger. It may reach more than 80% of the total thermal resistance. This is a principal reason to research on this kind of equipments and specially on the gas zone because any improvement can significantly increase the device performance.

Inline and staggered fin-and-tube arrangements are often used in heat exchanger applications. According to Ostanek and Thole [1] these bundles can be ranked by the pins size. Arrays with long pins have a height to diameter ratio larger than 5 and their main implementation is power generation. For pins with shorter aspect ratio (smaller than 0.5) the most common application is HVAC&R heat exchangers. When channel height is in the range in between long and short bundles ($0.5 < H/D < 4.0$) [2] the arrays are known as pin fin and they are used for cooling the trailing edge of gas turbine airfoils or for cooling electronic equipments.

Gas turbine applications are definitely a tall order. Due to the high velocities of the flow passing along the external surface of an airfoil, the heat transfer coefficients generated at their leading edge are very large. In addition to these high heat transfer coefficients, there is the difficulty of accomplishing a proper design in the small cross section of the airfoil trailing edge.

Configurations with pin fin arrays are a clear option to take into account also because they provide structural support to the facility by adding contact surface between endwalls. In this kind of layouts, heat transfer is a result of the interactions taking place between the pin fin wakes with the endwalls and downstream pins. The contribution of the pins and endwalls surfaces to the total heat transfer varies depending on the aspect ratio, streamwise and spanwise separation, and the actual array flow regime. This particular application usually presents turbulent flow regime, and the experience of understanding the most critical regions will be very useful to study similar problems with different purposes like evaporators of fin and tube heat exchangers on the next Chapter.

A pin fin array consists of a rectangular cross section channel with a finite number of pins that cross it from one end-wall to the other. A crucial aspect that needs to be covered is the limitation of space on which most applications work. Thereby, it is of much interest to develop pin fin channels with small aspect ratio. The addition of pins between walls increases the wetted heat transfer area and increases the turbulence levels of the channel flow. Therefore, the main objective of this kind of installations is accomplished by augmenting the convective heat transfer.

Experimental and numerical effort has been made trying to understand the complexity of the flow generated by this kind of geometry configuration. The principal characteristic parameters included in pin fin analysis are friction factor and heat transfer coefficients. Han et al. [3] provide a general description of heat transfer on gas turbine applications, where the proposed methodology can be applied to heat exchangers, nuclear power plants and electronic component cooling, which generally include pin fin layouts.

VanFossen [4] experimentally measured the heat transfer coefficients on pin and endwall surfaces for several staggered arrays of short pin fins. He found that heat transfer for short pin fin arrays was lower than for longer pin bundles at Reynolds numbers in the range from 300 to nearly 60000. Chyu et al. [5] carried out an experimental study on the individual contributions from pins and endwalls with the entire wetted surface of the pin fin array thermally active. Both inline and staggered distributions were studied for $5000 \leq Re \leq 25000$. They concluded that the pins had consistently 10 to 20 percent higher heat transfer coefficient than the endwalls.

Ames et al. [6–8] experimentally investigated the fluid dynamics and heat transfer of staggered pin fin arrays, they presented midline distribution of static pressure and heat transfer for every row of their array at three particular Reynolds numbers (3000, 10000 and 30000). They pointed out that turbulent augmentation and the rise in convective velocities within the array are the dominate drives of increased heat transfer rates. According to Labois and Lakehal [9], the complex behavior of this particular industrial flow application is found to be non homogeneous and inherently unsteady, with a flapping effect in the wake of the bundles. Lawson et al. [10] conducted several experiments to determine the effects of pin spacing in heat transfer and pressure loss through pin fin arrays for a range Reynolds numbers between 5000 and 30000. Ostanek and Thole [1] experimentally quantified the effects of streamwise spacing on the turbulent wake throughout various pin fin arrays.

References above, correspond to some of the experimental analysis known in the scientific literature. This kind of equipments and configurations have been also numerically studied by the fluid dynamics research community. The appropriate numerical solution of the complex flow presented in this kind of equipments is strongly related with the adequate use of Computational Fluid Dynamics (CFD) and the particular turbulence models selected to solve each case.

There has been an extensive research work on this topic trying to optimize the simulations by comparing different numerical strategies. Benhamadouche and Laurence [11] computed the cross flow in a staggered tube bundle with Large-Eddy Simulations (LES) and transient Reynolds stress transport model (RSTM) in 2D and 3D. Their LES results showed reasonable agreement with experiments, but RSTM showed no advantage over LES when the grid was coarsened.

Delibra et al. [12] studied an Unsteady Reynolds Averaged Navier Stokes (URANS) treatment using the eddy-viscosity model (ζ-f). They presented a geometrical configuration similar to the one experimentally studied by Ames et al. [6, 7] and compared their results for Reynolds number of 10000 and 30000.

Delibra et al. [13] used an hybrid LES/RANS simulation to study the same configuration dividing it on three distinct regions of the pin matrix. First, they detected that the flow around the first pin row (subjected usually to non-turbulent entry), was laminar with possible separation induced transition in the pin wakes. Second, further downstream (typically beyond the fifth pin row) the flow was fully turbulent and almost periodic. Finally, the last pin row behaved different than the second region since there were no downstream obstructions to feedback the pressure effects upstream.

Labois and Lakehal [9] used a method that blend between URANS and LES to predict flow across a tube bundle. The method resolved very large structures and modeled all sub scales of turbulence using a RANS two equation model. This strategy was able to provide the flow unsteadiness in three dimensions.

Typical LES is very costly in terms of computational power, in particular when applied to high Reynolds number practical industrial flow problems. This is one of the leading motivations for the present work, we have found in previous numerical researches that the mathematical formulation and LES models used herein are capable to accurately predict the flow over bluff bodies with massive separation [14], specially when coarse meshes are being used [15].

In the present paper LES studies have been performed using three SGS models suitable for unstructured mesh formulations: the QR eddy-viscosity model [16], the wall-adapting local-eddy viscosity model (WALE) [17] and the WALE model within a variational multiscale framework (VMS-WALE) [18].

This paper aims at comparing the performance of these SGS models applied to industrial applications in different flow regimes (Reynolds number of 3000, 10000 and 30000 respectively). As far as the authors knowledge is concerned, the performance of the selected SGS models have not been reported in the literature for this kind of applications. Furthermore, we are not aware of previous numerical results published on Reynolds number equals to 3000.

3.2 Mathematical and numerical model

In this work, the proposed methodology is based on the numerical simulation of the channel by means of CFD using the inhouse TermoFluids software [19]. The domain is divided into multiple control volumes (CV) on which the Navier-Stokes and energy equations (Eqs. 4.3, 4.4 and 4.5) are written and converted into algebraic equations using three-dimensional unstructured collocated meshes and symmetry preserving schemes [20] as follows,

$$\begin{aligned} \mathsf{M}\boldsymbol{u} &= \mathbf{0} & (3.1) \\ \frac{\partial \boldsymbol{u}}{\partial t} + \mathsf{C}\left(\boldsymbol{u}\right)\boldsymbol{u} + \nu \mathsf{D}\boldsymbol{u} + \rho^{-1}\mathsf{G}\boldsymbol{p} &= \mathsf{C}\left(\boldsymbol{u}\right)\boldsymbol{u} - \overline{\mathsf{C}\left(\boldsymbol{u}\right)\boldsymbol{u}} & \\ &\approx -\mathsf{M}\mathcal{T} & (3.2) \\ \frac{\partial T}{\partial t} + \mathsf{C}\left(\boldsymbol{u}\right)T + \frac{\nu}{Pr}\mathsf{D}T &= \mathsf{C}\left(\boldsymbol{u}\right)T - \overline{\mathsf{C}\left(\boldsymbol{u}\right)T} & \\ &\approx -\mathsf{M}\mathcal{T}_T & (3.3) \end{aligned}$$

where $\boldsymbol{u}$ and $\boldsymbol{p}$ are the velocity and pressure fields, respectively. ν is the kinematic viscosity and ρ the density. Convective and diffusive operators in the momentum equation for the velocity field are given by $\mathsf{C}\left(\boldsymbol{u}\right) = \left(\boldsymbol{u}\cdot\nabla\right)$ and $\mathsf{D} = -\nabla^2$, respectively. Gradient and divergence operators are given by $\mathsf{G} = \nabla$ and $\mathsf{M} = \nabla\cdot$, respectively. $\mathcal{T}$ is the SGS stress tensor, which is defined as:

$$\mathcal{T} = -2\nu_{sgs}\overline{\mathcal{S}_{\mathsf{ij}}} + (\mathcal{T} : \mathsf{I})\mathsf{I}/3 \tag{3.4}$$

where ν_{sgs} is the subgrid-scale viscosity, and $\mathcal{S}_{\mathsf{ij}}$ is the stress tensor defined as $\overline{\mathcal{S}_{\mathsf{ij}}} = \frac{1}{2}\left[\mathsf{G}(\boldsymbol{u}) + \mathsf{G}^*(\boldsymbol{u})\right]$, where G^* is the transpose of the gradient operator. $\mathcal{T}_T$ term is evaluated as in $\mathcal{T}$ term, but ν_{sgs} is substituted by ν_{sgs}/Pr_t, where Pr_t is the turbulent Prandtl number (0.4 in this paper).

As aforementioned, numerical schemes used are conservative, i.e., they preserve the kinetic energy equation. These conservation properties are held if and only if the discrete convective operator is skew-symmetric ($\mathsf{C}\left(\boldsymbol{u}\right) = -\mathsf{C_c}^*\left(\boldsymbol{u}_c\right)$), the negative conjugate transpose of the discrete gradient operator is exactly equal to the divergence operator ($-\left(\Omega_c\mathsf{G}_c\right)^* = \mathsf{M}_c$), and the diffusive operator D_c is symmetric and positive-definite (the subscript *c* holds for the cell-centered discretization, and the subscript *s* holds for the staggered faces). These properties ensure both stability and conservation of the kinetic-energy balance even at high Reynolds numbers and with coarse grids.

A fractional-step method is applied to solve the momentum Eq. (4.4). The time-integration method chosen for the convective and diffusive terms is a two-step linear explicit scheme, while for the pressure gradient term an implicit first-order scheme is used [21].

The velocity-pressure coupling is solved by means of a classical fractional-step projection method, $\boldsymbol{u}_c^p = \boldsymbol{u}_c^{n+1} + \mathsf{G}\tilde{\boldsymbol{p}}_c$, where $\tilde{\boldsymbol{p}}_c = \boldsymbol{p}_c^{n+1}\Delta t^n/\rho$ is the pseudo-pressure, $\boldsymbol{u}_c^p$ is the predicted velocity, $n+1$ is the instant where the temporal variables are calculated, and Δt^n is the current time step ($\Delta t^n = t^{n+1} - t^n$). Taking the divergence of $\boldsymbol{u}_c^p$ and applying the incompressibility condition yields a discrete Poisson equation for $\tilde{\boldsymbol{p}}_c$: $\mathsf{L_c}\tilde{\boldsymbol{p}}_c = \mathsf{M}_c\boldsymbol{u}_c^p$. The discrete Laplacian operator $\mathsf{L_c}$ is, by construction, a symmetric positive definite matrix ($\mathsf{L_c} \equiv \mathsf{M}\Omega^{-1}\mathsf{M}^*$).

Finally, the mass-conserving velocity at the faces ($\mathsf{M}_s\boldsymbol{u}_s^{n+1} = 0$) is obtained from the correction, $\boldsymbol{u}_s^{n+1} = \boldsymbol{u}_s^p - \mathsf{G}_s\tilde{\boldsymbol{p}}_c$, where G_s represents the discrete gradient operator at the CV faces. This approximation allows to conserve mass at the faces but it has several implications. If the conservative term is computed using $\boldsymbol{u}_s^{n+1}$, in practice an additional term proportional to the third-order derivative of $\boldsymbol{p}_c^{n+1}$ is introduced. Thus, in many aspects this approach is similar to the popular Rhie and Chow [22] interpolation method and eliminates checkerboard modes.

However, collocated meshes do not conserve the kinetic energy as shown by Morinishi et al. [23] for finite-difference schemes and by Felten and Lund [24] for finite-volume schemes. When the fractional-step method on a collocated arrangement is used, there are two sources of errors in the kinetic energy conservation: i) due to interpolation schemes and, ii) due to inconsistency in the pressure field in order to ensure mass conservation. While the first one can be eliminated through the use of conservative schemes such as those used in the present work, the latter equals to $\epsilon_{\mathbf{ke}} = (\tilde{\boldsymbol{p}}_c)^*\mathsf{M}_c(\mathsf{G}_c - \mathsf{G}_s)\tilde{\boldsymbol{p}}_c$. This contribution of the pressure gradient term to the evolution of the kinetic energy can not be eliminated. Felten and Lund [24] have conducted a study to determine its scaling order. They have shown that the spatial term of the pressure error scales as $\mathcal{O}(\triangle x^2)$ and the temporal term scales as $\mathcal{O}(\triangle t)$, i.e., pressure errors are of the order of $\mathcal{O}(\triangle x^2\ \triangle t)$. However, it has been proved that pressure errors do not have a significant impact on the results at grid resolutions and time-steps used in both LES and Direct Numerical Simulation (DNS) [15, 25, 26].

A brief description of the models used in this analysis is given hereafter.

3.2.1 QR eddy-viscosity model

It was proposed by Verstappen [16] and it is a SGS model based on the invariants of the rate-of-strain tensor which is proposed with the following advantages compared to the classical Smagorinsky formulation:

- $\nu_{sgs} = 0$ in any laminar flow,
- $\nu_{sgs} = 0$ in any 2D flow,
- $\nu_{sgs} \propto y^3$ near a wall (with y being the wall normal coordinate), and
- $\nu_{sgs} \to 0$ when $l \propto Re^{\frac{-3}{4}}$ (where l is the grid cutting length).

The QR-model is expressed in terms of the invariants of the rate-of-strain tensor and does not involve any explicit filtering:

$$\begin{aligned} \nu_{sgs} &= (c_{qr}l)^2 \frac{r^+}{q} \\ c_{qr} &= \frac{1}{\pi} + \frac{1}{24} \\ \mid \overline{\mathcal{S}_{\mathsf{ij}}} \mid &= (2\overline{\mathcal{S}_{\mathsf{ij}}\mathcal{S}_{\mathsf{ij}}})^{1/2} \\ q &= \frac{1}{4} \mid \overline{\mathcal{S}_{\mathsf{ij}}} \mid^2 \\ r &= -det\overline{\mathcal{S}_{\mathsf{ij}}} \end{aligned} \tag{3.5}$$

3.2.2 Wall-adapting local eddy viscosity model (WALE)

This model proposed by Nicoud and Ducros [17] is based on the square of the velocity gradient tensor. In their formulation the SGS viscosity accounts for the effects of both the strain and the rotation rates of the smallest resolved turbulent fluctuations. In addition, the proportionality of the eddy viscosity near walls ($\nu_{sgs} \propto y^3$) is recovered without any dynamic procedure.

$$\begin{aligned} \nu_{sgs} &= (C_w\Delta)^2 \frac{(\mathcal{V}_{\mathsf{ij}} : \mathcal{V}_{\mathsf{ij}})^{\frac{3}{2}}}{(\overline{\mathcal{S}_{\mathsf{ij}}} : \overline{\mathcal{S}_{\mathsf{ij}}})^{\frac{5}{2}} + (\mathcal{V}_{\mathsf{ij}} : \mathcal{V}_{\mathsf{ij}})^{\frac{5}{4}}} \\ \mathcal{V}_{\mathsf{ij}} &= \frac{1}{2}[\mathsf{G}(\overline{\boldsymbol{u}_c})^2 + \mathsf{G}^*(\overline{\boldsymbol{u}_c})^2] - \frac{1}{3}(\mathsf{G}(\overline{\boldsymbol{u}_c})^2\mathsf{I}) \end{aligned} \tag{3.6}$$

In our studies a value of $C_w = 0.325$ is used according with the procedure recommended by Nicoud and Duros [17].

3.2.3 WALE model within a variational multiscale framework (VMS-WALE)

The variational multiscale (VMS) approach was originally formulated for the Smagorinsky model by Hughes et al. [18] in the Fourier space. In VMS three classes of scales are considered: large, small and unresolved scales. If a second filter with filter length $\hat{l}$ is introduced (usually called test filter), a splitting of the scales can be performed,

$$f' = \overline{f} - \hat{f} \tag{3.7}$$

where, following Vreman [27] notation, f' is called the small-scale component, $\hat{f}$ is the large-scale component and $\overline{f}$ is the original resolved quantity. Thus, for the large-scale parts of the resolved $\overline{u}$ a general governing equation can be derived,

$$\frac{\partial \overline{\boldsymbol{u}_c}}{\partial t} + \mathsf{C}\left(\overline{\boldsymbol{u}_c}\right)\overline{\boldsymbol{u}_c} + \nu \mathsf{D}\overline{\boldsymbol{u}_c} + \rho^{-1}\mathsf{G}\overline{\boldsymbol{p}} \quad = \quad -\frac{\partial \widehat{\mathcal{T}}}{\partial x_j} - \frac{\partial \mathcal{T}'}{\partial x_j} \tag{3.8}$$

Inspecting equation (3.8) it is possible to identify $\widehat{\mathcal{T}}$ as the subgrid term in the large-scale equation and $\mathcal{T}'$ as the subgrid small-scale term. Now, neglecting the effect of unresolved scales in the large-scale equation ($\widehat{\mathcal{T}} \approx 0$), we only need to model $\mathcal{T}'$. In our implementation the *small-small* strategy is used in conjunction with the WALE model:

$$\begin{aligned} \mathcal{T}' &= -2\nu_{sgs}\mathcal{S}_{\mathrm{ij}}{}' + \frac{1}{3}\mathcal{T}'\delta_{ij} \qquad (3.9) \\ \nu_{sgs} &= (C_w^{vms}\Delta)^2 \frac{(\mathcal{V}_{\mathrm{ij}}{}' : \mathcal{V}_{\mathrm{ij}}{}')^{\frac{3}{2}}}{(\mathcal{S}_{\mathrm{ij}}{}' : \mathcal{S}_{\mathrm{ij}}{}')^{\frac{5}{2}} + (\mathcal{V}_{\mathrm{ij}}{}' : \mathcal{V}_{\mathrm{ij}}{}')^{\frac{5}{4}}} \end{aligned}$$

where C_w^{vms} is the equivalent of the WALE coefficient for the *small-small* VMS approach and in the finite volume context its value lies in the range between 0.3 and 0.5.

3.3 Definition of the case

The geometric array presented for the experimental analysis by Ames et al. [6–8] and the numerical simulations by Delibra et al. [12, 13] consisted of a matrix of wall-bounded 8×8 cylindrical pins. The present work uses the same configuration of the domain in order to validate the results here obtained. The test case is an air flow across 8 staggered rows of pins, spaced at 2.5D in stream-wise and span-wise directions, with D being the diameter of the pins, and the channel height being twice the diameter ($H = 2D$). Upstream region before the first row, has a length of $7.5D$,

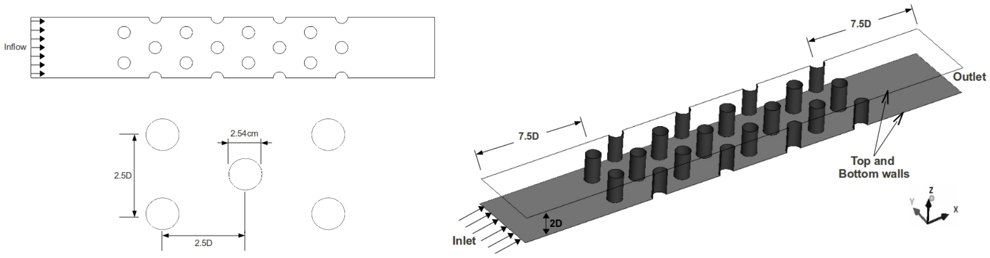

Figure 3.1: Pin fin array and complete computational domain.

and the same distance is considered downstream of the last row. This configuration is detailed in Fig. 3.1.

The meshes used for solving the considered domain are generated with a body fitted strategy (see Fig. 3.2). The final result of the mesh is a three-dimensional (3D) structured grid with a hyperbolic distribution on the z axis in order to solve the boundary layer caused by the top and bottom walls of the channel. The domain is periodic on the spanwise direction corresponding to y axis represented in Fig. 3.1. Originally the experiments of Ames et al. [6–8] were conducted on a complete matrix of 8 pins. However due to the nature of the flow in this kind of geometries, it is considered a good approximation to simulate only one part of the domain using periodic boundary conditions. This assumption has been previously made by other numerical investigations [12, 13] showing good results.

The simulations are performed for a computational domain composed of two rows of cylindrical pins in the spanwise direction. While for the streamwise direction all the length of the channel is considered in order to avoid the possible inflow and outflow external effects from the experiment (as shown in Fig. 3.1). The domain width is $5D$, the distance between endwalls (pins height) is $2D$ and the streamwise length is $32.5D$.

Homogeneous flow is assumed as the initial condition of all simulations. At the inlet, a uniform and constant velocity profile is considered $u = (1, 0, 0)$. No fluctuations are imposed. Non dimensional temperature is defined by $T^* = (T - T_C)/(T_H - T_C)$, where T_C represents cold temperature, and T_H is the hot temperature. The dimensionless thermal field is then in the range between zero and one along the domain. Temperature considered at the inlet boundary is set constant, $T = T_H$. The top, bottom and cylinder solid walls have non-slip conditions and a constant temperature is imposed ($T = T_C$). The Prandtl number used is 0.71 corresponding to air. As mentioned earlier, the domain is periodic (only one characteristic part of the experimental facility is simulated). The periodic conditions are fully implicit, i.e., the boundary faces are treated like the internal ones. Finally, downstream the outlet boundary condition is pressure based.

The Reynolds number is based on the pin diameter and the average gap bulk velocity ($Re = \frac{V_{max}D}{\nu}$). The gap bulk velocity is found between two adjacent pins of the same row. Fluid properties are set so as the Reynolds number based on the gap bulk velocity and constant diameter equals to 3000, 10000 and 30000, respectively.

3.3.1 Computational meshes

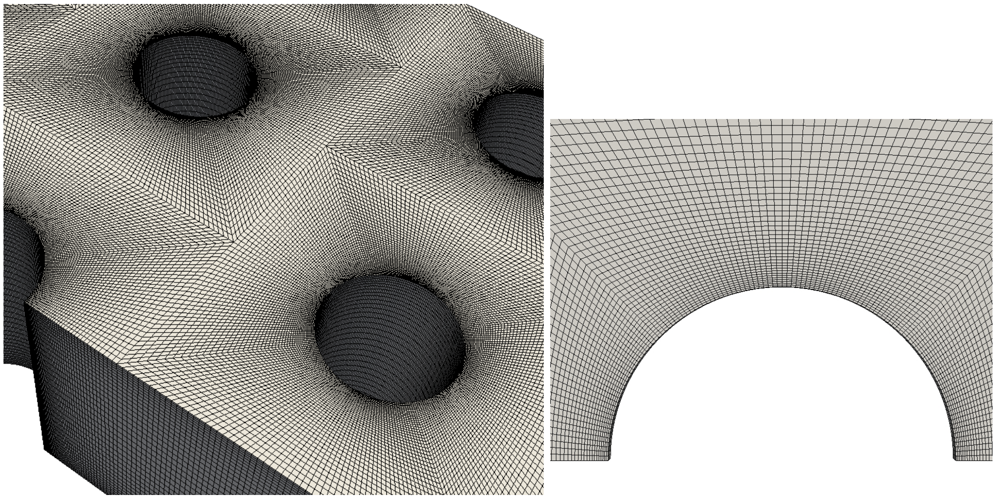

Figure 3.2: Details of the mesh used for the present LES treatment. (7.098×10^6 CV).

Three different mesh levels are considered. First, a coarse three dimensional mesh with 1.68 million CV (*m1*). The second level of grid refinement consists on a mesh with 3.74 million CV (*m2*), and finally the finer mesh with 7.09 million CV (*m3*). A picture of the finest mesh (*m3*) is shown in Fig. 3.2 where the reader can distinguish the refinement considered near the solid walls in every direction needed. All the results presented in the present paper are obtained using the finest mesh (*m3*). It should be pointed out that the grids used in Delibra et al. [13] on their LES analysis contained 5.5 million cells for $Re = 10000$ and up to 15 million CV for $Re = 30000$ (using only half of the present computational domain). The critical case is for the highest Reynolds number of 30000, where the boundary layer around the cylinders is thinner ($\delta/D \sim 0.0113$). Table 3.3.1 shows the non dimensional size of the first cell around cylinders ($\Delta y/D$ or $\Delta x/D$) and near the endwalls ($\Delta z/D$) on each mesh.

Mesh	NCV $\times 10^{-6}$	1st CV cylinders	1st CV endwalls
m1	1.68	0.02	0.08
m2	3.74	0.01	0.08
m3	7.09	0.01	0.03

Table 3.1: Detail of some mesh parameters.

3.3.2 Mesh assessment

To ensure mesh independence of the present results, a detailed study is carried out simulating the same case with three different mesh levels. Mesh 1 (*m1*) has 1.68 million prismatic elements, mesh 2 (*m2*) has 3.744 million control volumes (CV) and finally, mesh 3 (*m3*) contains 7.098×10^6 CV.

All meshes are built with prismatic elements refined on the near wall regions (both on the cylinders and on the end-walls) as shown in Fig. 3.3. To generate the meshes, the body-fitted technique is applied and therefore, three dimensional structured meshes with hyperbolic distribution on z-direction is used to run the present simulations.

Figs. 3.4 to 3.6 show some of the parameters studied for the present simulations, which are c_p on line C and velocity profiles on line B (location illustrated in Fig. 3.7) for the three Reynolds numbers presented. These results are obtained using the WALE model.

The wall y^+ is a non-dimensional distance, only technically applicable to parts of the flow that are close to the wall.

$$y^+ = (u_\tau y)/\nu \tag{3.10}$$

The objective of using this parameter is to ensure that the used mesh is appropriately solving the boundary layer of the flow. In the present research, the same meshes are used for three different Reynolds numbers, hence this non-dimensional distance (y^+) increases in proportion to the Reynolds number.

The values of y^+ of the wall nearest cells are in general less than 1 for the two lower Reynolds numbers (3000 and 10000), while for Reynolds equal 30000 the y^+ values are kept smaller than 2 in most of the domain.

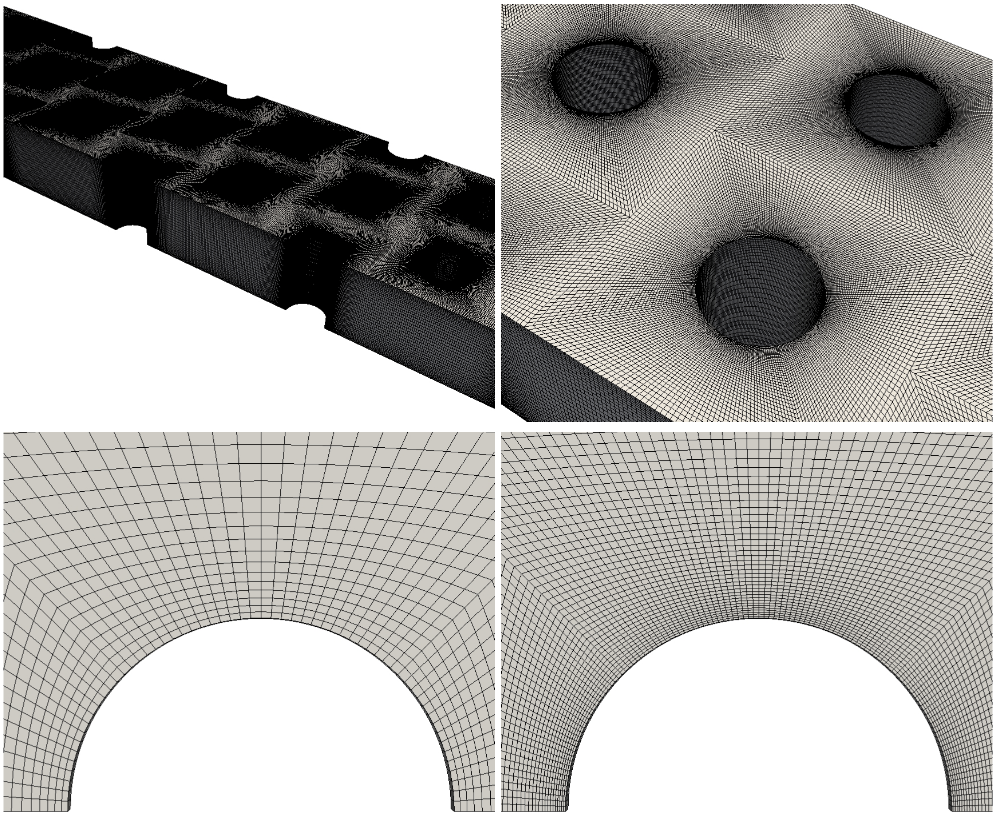

Figure 3.3: Mesh resolution of, top: *m3* used for present results. Bottom: comparison between coarser (*m1*) and finest (*m3*) meshes.

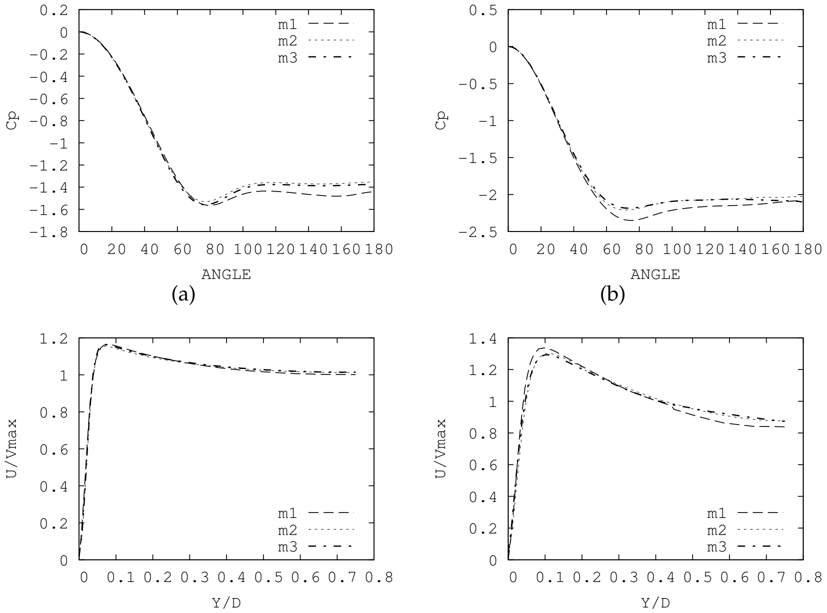

(a) (b)

(c) (d)

Figure 3.4: $Re = 3000$. a) Pressure coefficient, first row. b) Pressure coefficient, fifth row. c) Velocity distribution at line B, first row. d) Velocity distribution at line B, fifth row.

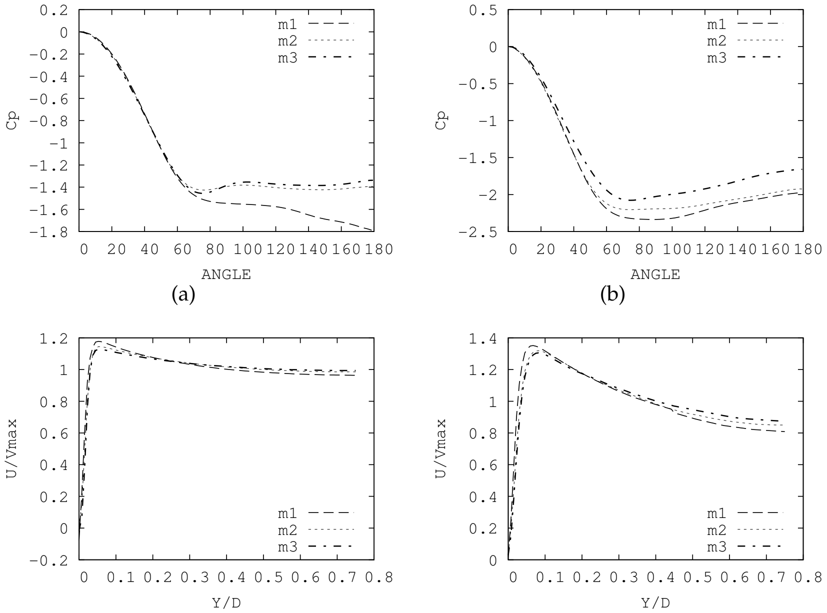

(a) (b) (c) (d)

Figure 3.5: $Re = 10000$, a) Pressure coefficient, first row. b) Pressure coefficient, fifth row. c) Velocity distribution at line B, first row. d) Velocity distribution at line B, fifth row.

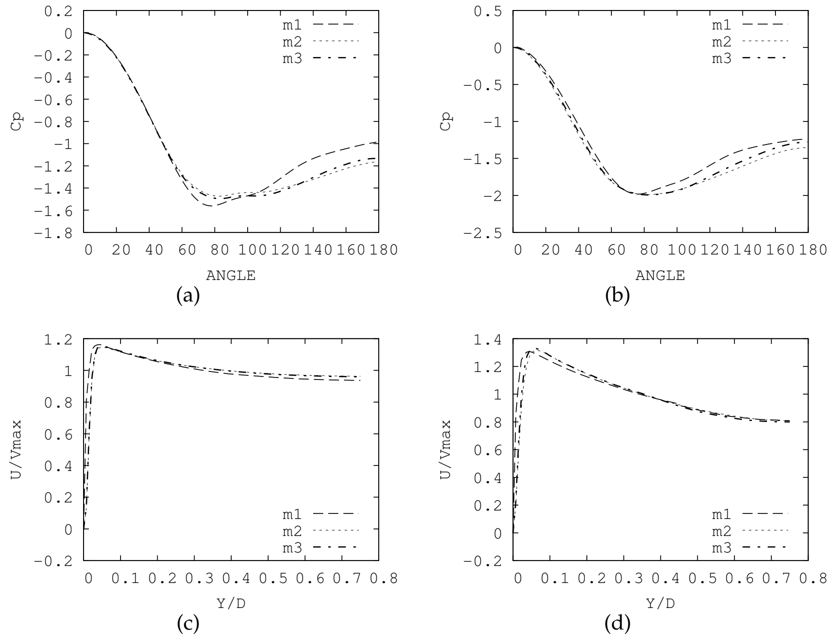

(a)

(b)

(c)

(d)

Figure 3.6: $Re = 30000$, a) Pressure coefficient, first row. b) Pressure coefficient, fifth row. c) Velocity distribution at line B, first row. d) Velocity distribution at line B, fifth row.

3.4 Results and discussion

In order to obtain the numerical results presented, simulations are advanced in time until statistical stationary flow conditions are achieved. 2000 dimensionless time units (TU^*) are simulated ($TU^* = tV_{max}/D$), and only the last 1200 are taken into account for the time averaged results. For validation purposes at some particular pin rows, the results are compared with the experimental data given by Ames et al. [6–8] and the numerical results presented by Delibra et al. [12, 13].

When analyzing the mean flow velocity profiles, two different locations are studied. First, the vertical line at exactly mid-distance between neighboring cylinders, which would be the line placed at $1.25D$ from the center of one pin on the y axis in the y-z plane (line A). And second, the horizontal line formed between the centers of two adjacent pins measured at $90°$ at the pin mid-heights (line B). For $Re = 30000$, two more locations are studied in order to understand the physics of the problem in the region closer to the cylinder wall. These locations are depicted as lines D and E in Fig. 3.7. For pressure distributions around the cylinders, line C is used at midhight of the pins height.

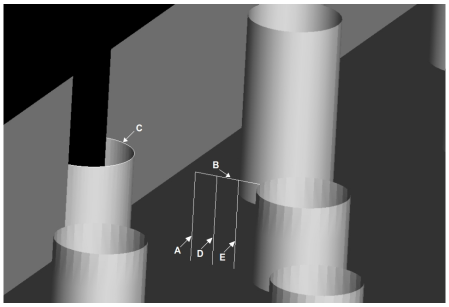

Figure 3.7: Geometrical location of lines (A,B,C,D and E) along which the computational results are compared with experiments and previous numerical investigations.

3.4.1 Instantaneous flow

The main purpose of this geometrical configuration is to enhance the heat transfer of the system by augmenting the turbulence of the flow and the heat transfer surface. Vorticity describes the local angular rate of rotation of the flow, and its study can illustrate the turbulence levels that are generated by the pins on the complete channel flow. Fig. 3.8 presents a comparison of the vorticity for the three Reynolds numbers discussed in the present study at the first four rows.

The most significant rows of pins that increase the turbulence level of the flow are the first two rows. Regardless of the Reynolds number under analysis, the first and second rows have great influence on mixing the air passing throughout the channel (except maybe for $Re = 30000$ where the second row has less impact thereon). The staggered configuration of the matrix array urges the vortex shedding of the cylinders to mix with each other, augmenting the turbulence level of the flow row by row. The near distance between cylinders along with the short aspect ratio of the pins, contribute to the heat transfer enhancement by introducing complex three-dimensional flow structures like horseshoe vortices (not shown in the figure). When the Reynolds number is enlarged the mixing of the flow takes place closer to the entrance region because of the complex turbulent behavior of the flow which presents strong oscillatory effects in the wake of the tube bundle.

Instantaneous snapshots of the thermal field at 50% of the channel height are presented in Fig. 3.9 for the three Reynolds numbers herein analyzed. In Fig. 3.9a, at

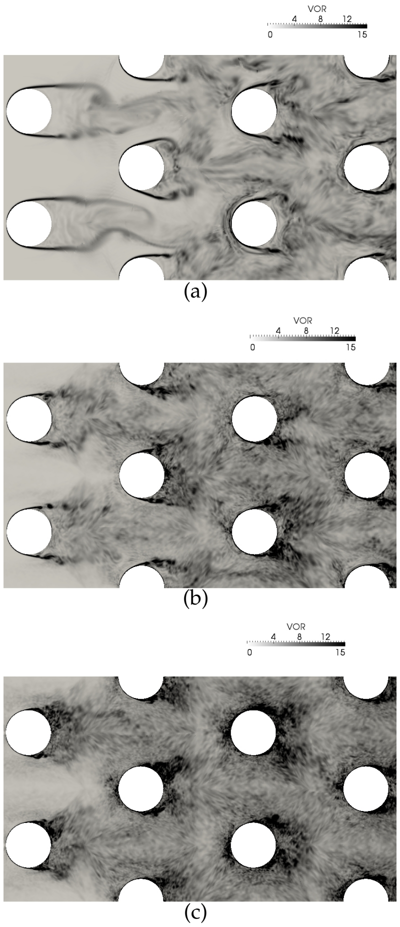

(a)

(b)

(c)

Figure 3.8: Instantaneous snapshot of the vorticity in plane x-y at $z = 1.4D$ a) $Re = 3000$, b) $Re = 10000$ and c) $Re = 30000$.

$Re = 3000$ the wake behind the first row is long enough to reach the space between the pins of the second row. This thick trail caused by the first row of pins is then mixed with the vortex caused at the second row because the nature of the flow tends to exhibit a slight oscillation in the spanwise direction. Hence, cooler flow of air reaches the third row and keeps mixing with the fluid downstream.

For $Re = 10000$, Fig. 3.9b illustrates the vortex structures generated by the pins and a clear separation of the boundary layer is present. Ahead the fourth row, recirculation zones are captured in the instant figure. The first three rows of pins have stronger interaction in the streamwise direction, nevertheless after the flow passes the third row the mixing between lateral adjacent pins is present. A close look to Fig. 3.9c representing Reynolds number of 30000, shows less cold fluid trapped behind the pins in the recirculation zones of the first two rows. There is a clear trail of cold flow leaving from the first row and interacting with the rear of the center pin from the second row. This early interaction is caused not only because of the high Reynolds number and turbulence intensity but also because of the staggered array that favors the mixing and thereby enhance the heat transfer between fluid and solid walls.

A common feature for the three Reynolds numbers is that disturbances from upstream wakes caused a more complex flowfield beyond the third row. In this kind of complex configurations, the flow presents a wide range of scales that the present formulation in conjunction with the selected SGS models can predict. It is observed that the principal transport mechanism in every Reynolds number analyzed in the present paper are the medium and large scales generated in the flowfield.

3.4.2 Average flow

Hydrodynamics

Pressure coefficient is defined as $c_p = [P_\theta - P_0]/(\rho {V_{max}}^2/2)$, where P_0 is the pressure at the stagnation point in the cylinder, and P_θ is the pressure of the flow at the θ circumferential angle around the pin (with θ ranging from 0 to 180 deg.).

Separation of the boundary layer occurs when the flow tries to decelerate quickly under an adverse pressure gradient. At that point on the cylindrical wall surface, the velocity gradient becomes zero. Thus location of flow separation is determined by the pressure gradient at the surface. For cross flow over a single cylinder, separation occurs around 90 degrees when the flow is laminar and later when the flow becomes turbulent. However if a matrix of cylindrical pins is studied, downstream pins directly affect the adverse pressure gradient of the flow, which determines the location of the separation point.

A comparison of pressure coefficient between the numerical models used for the simulations and the experimental data [6] for Re=3000 is presented in Fig. 3.10. The pressure distributions are measured at the circumference in the mid-height of the pins at $z = D$ (line C in Fig. 3.7).

QR and VMS SGS models seem to behave very similar around the cylinders for this particular Reynolds number, while WALE model performs slightly different specially at the second and third rows. In general, WALE model has a poorer performance in solving the pressure coefficient around the cylinders when $Re = 3000$.

Nevertheless, given the main goal of the present paper, it is important to stand out that each one of the three SGS models have a reasonable agreement with experiments.

For the velocity distributions, the comparison is made for the fifth row (see Fig. 3.11) where experimental measurements [6] are available. Both works (experiments and present CFD) have a very good agreement in absolute values.

For the velocity profile, WALE model can better predict the velocity boundary layer caused by the cylinder in line B at the fifth row (see Fig. 3.11). Again VMS and QR models have almost the same performance. At this point of the geometry (row #5) where the upstream pins and endwalls have modified the flow, WALE model has major capacity to predict the behavior of the flow configuration. At the fifth row the flow is fully turbulent (including the boundary layer formed around the pins) thus presenting more mixing and this may be the reason for WALE model to obtain slightly better results than the other SGS models. A closer analysis of the velocity profiles on the first, second, third and fifth rows is shown in Fig. 3.12 using WALE model.

Reynolds numbers of 10000 and 30000 were numerically investigated by Delibra et al. [12], using URANS simulations, where it was shown that the elliptic-relaxation eddy viscosity model, was able to capture the vortex shedding and the consequent gross effects on the flow development, although some deficiencies were observed in predicting the wakes behind the pins, their structure, size and recirculation strength. In a subsequent paper Delibra et al. [13] applied hybrid LES/RANS techniques and found that for the near-wall region URANS treatment was sufficiently adequate to model the unsteady turbulent transport. While for the outer region, LES reproduced well the local convection by coherent vortical structures.

Fig. 3.13 shows a comparison of pressure coefficients between models and literature available results. The clear differences for the results between models suggest that the selection of the SGS model is more significant for higher Reynolds numbers, specially because the same grid is used.

The velocity profiles numerically obtained for this flow are presented in Figs. 3.14 and 3.15. The distribution of velocity on the horizontal midplane (line B) of the present simulations compares well with the experimental data (see Fig. 3.14), but there are some differences specially for the distribution of the boundary layer (where WALE model seems to agree fair well with the expected results). At line A (vertical midplane) in Fig. 3.15, the models have sort of a different behavior showing clear discrepancies between each other. The mesh at the vertical midplane between neighboring pins near the endwalls is coarser than in the regions near the cylinders, this may be the reason why current results seem to have some difficulties to accurately estimate the boundary layer shown in Fig. 3.15. WALE model has a slightly better performance for this purpose than QR and VMS models. However, given the coarse mesh used in the present study, all three models can be considered as a practicable option for simulations in a set-up of industrial applications like pin fin arrays. These observations can be also made if the Reynolds number under study is 30000 for wich Figs. 3.17 and 3.16 show the velocity profiles along lines A and B respectively.

Making reference to Fig. 3.18 which illustrates the distribution of pressure coefficient around the cylinders for different tube rows, one can see that VMS model displays sufficiently good agreement with the experiment in all the rows, despite it is not the most accurate model in the local row by row analysis.

WALE model has some difficulties to accurately predict the pressure distribution of the boundary layer around the cylinders. But for the first row it seems to agree better with the experiment than other SGS models. Comparing present results also with previous numerical analysis, QR model shows acceptable coincidence with experiments for this flow regime ($Re = 30000$). The exception of the last statement is the third row where QR model seems to overpredict the pressure coefficient in all the circumference of the pin.

An important aspect to be considered is that with the algorithm used for the present analysis, even if the flow gets more turbulent, the results are not compromised and have good agreement with experiments (even when the mesh used is very coarse for the expectations at this Reynolds number and with LES treatment).

Fig. 3.19 is a comparison only for the third row at different locations of the y-z plane. Line A represents the vertical line between adjacent cylinders, this means that the location in this plane is $y = 1.25D$ from the center of the pin. Line D is at $y = D$, and line E is at $y = 0.75D$ from the center of the pin (see Fig. 3.7 for schematic representation).

For $Re = 30000$ at the third row, the models are in better agreement between each other than for Reynolds number of 10000. It is clear that the formulation of WALE SGS model shows slightly better predictions of the flow near the pins for the present configuration. As mentioned before, LES techniques usually require finer meshes than the ones used in the present study. For this reason, the ability of WALE model to sufficiently dissipate energy together with coarse meshes is necessary in order to obtain realistic results.

Heat transfer

Table 3.4.2 presents a comparison between experimental data [6], correlation results [28], previous numerical simulations [13] and the present analysis for the time averaged Nusselt number ($Nu = hD/k$) at one endwall of the domain with the different LES models used in the present research (h holds for the convective heat transfer coefficient and k holds for the thermal conductivity of the fluid).

For Reynolds number of 10000 and 30000 respectively, experiments and correlation show very good agreement between each other. At every Reynolds number

Re	correlation [28]	experiment [6]	numeric [13]	LES QR	LES WALE	LES VMS
3000	23.82	—	—	21.49	21.91	21.34
10000	54.33	54.1	44.3^{LES}	53.75	51.16	43.45
30000	115.31	111.5	$84.2.3^{LES}$	110.60	115.45	112.59

Table 3.2: Averaged endwall Nusselt number.

studied, sufficiently fine results for the average Nusselt number on the endwall are obtained for the presented methodology, reaching acceptable concordance with the reference data with the three models. QR SGS model seems to have slightly better performance to this purpose, however it is not completely clear the reason of this improvement.

Fig. 3.20 shows the local Nusselt number on the endwall normalized with the surface averaged value along the cutline placed at $y = 1.25D$ cutting through rows 1, 3, 5 and 7. The first aspect to point out is that the three models have some discrepancies in between for every Reynolds number in a local analysis. When experimental data is available (Reynolds numbers of 10000 and 30000 respectively), present results display better agreement for the first half of the domain than for the downstream region. On the other hand, Fig. 3.21 represents the cutline passing through even rows (2, 4, 6 and 8), where the performance is very similar to the one in the odd rows.

Comparing Figs 3.20 and 3.21 with the results presented in Table 3.4.2, some discrepancies between the present study and experimental data are observed regarding to local values of the heat transfer coefficients. This might be due to the fact that thermal field needs to be resolved more accurately than hydrodynamic field, and for this particular case, the local analysis supports this statement. However, analyzing the results obtained in terms of average quantities, the performance of the present simulations is considered to be sufficiently good, which might be of interest for practical applications.

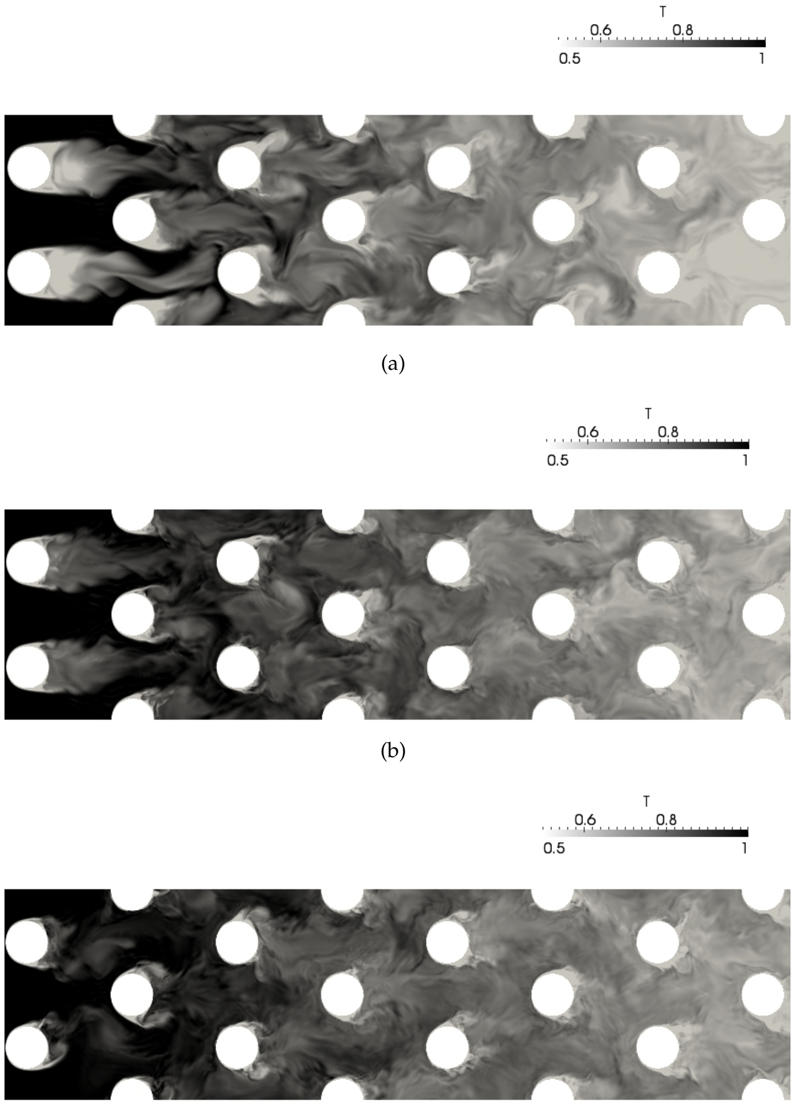

(a)

(b)

(c)

Figure 3.9: Instantaneous snapshot of the temperature at 50% of the channel height. a) $Re = 3000$, b) $Re = 10000$ and c) $Re = 30000$.

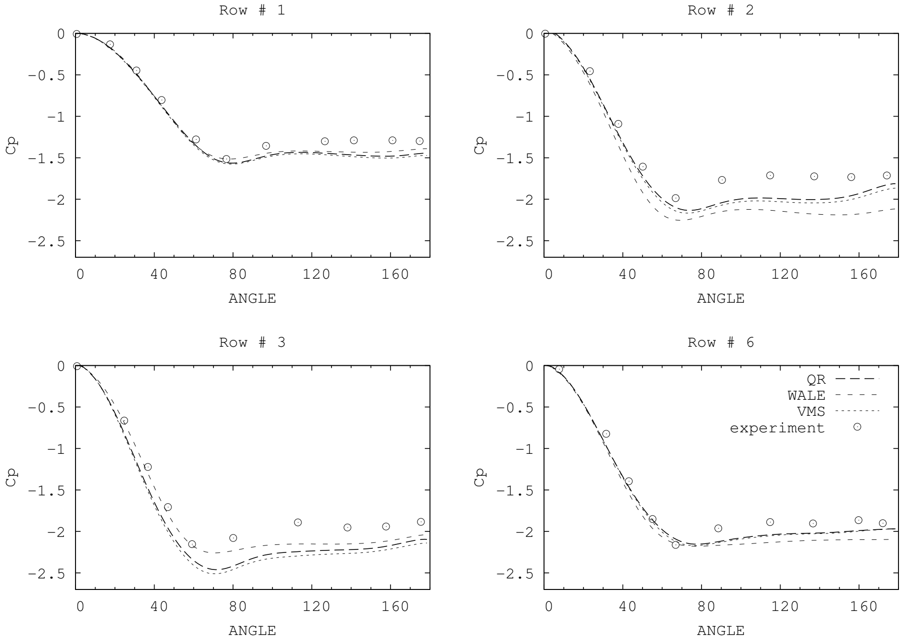

Figure 3.10: Distribution of pressure coefficients around pins (at z=D) for $Re = 3000$. Experimental data taken from [6].

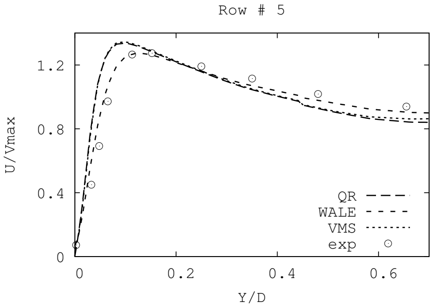

Figure 3.11: Mean velocity profile in line B at row 5 for $Re = 3000$. Experiment data taken from [7].

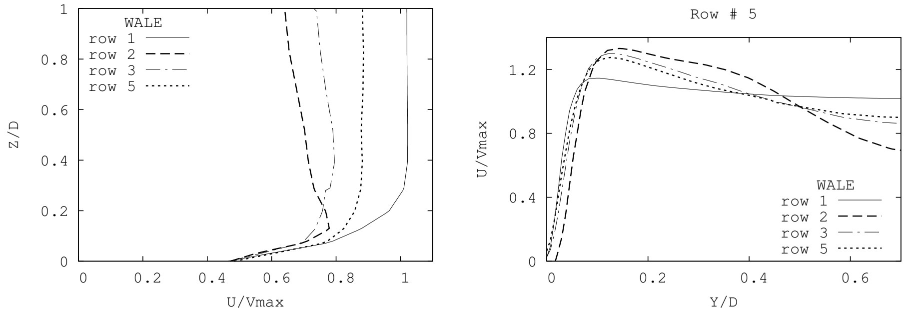

(a) (b)

Figure 3.12: Mean velocity profiles at different rows in: a) line A and b) line B using WALE SGS model for $Re = 3000$.

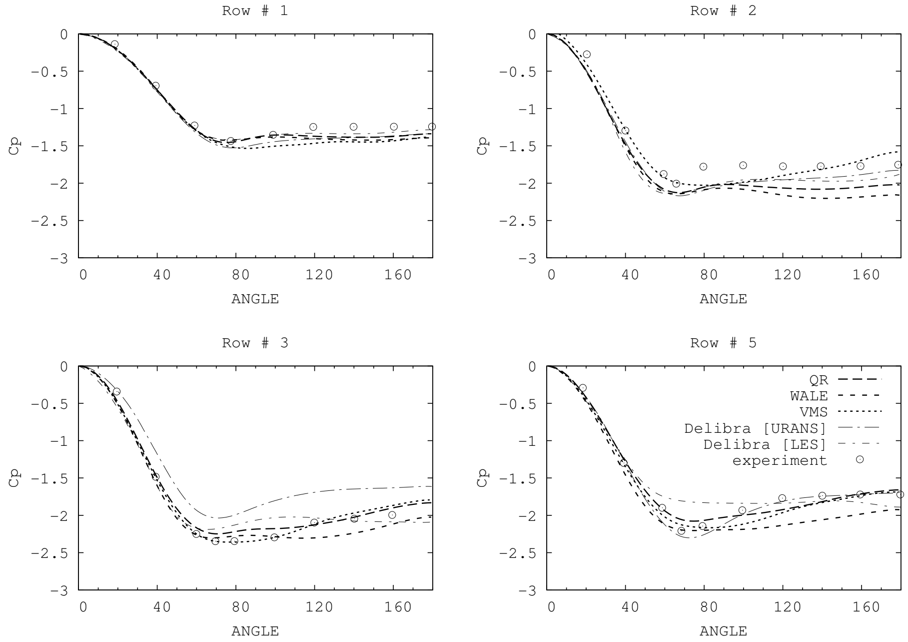

Figure 3.13: Distribution of pressure coefficients around pins (at z=D) for $Re = 10000$. [URANS] and [LES] data, taken from [12]. Experimental data taken from [6].

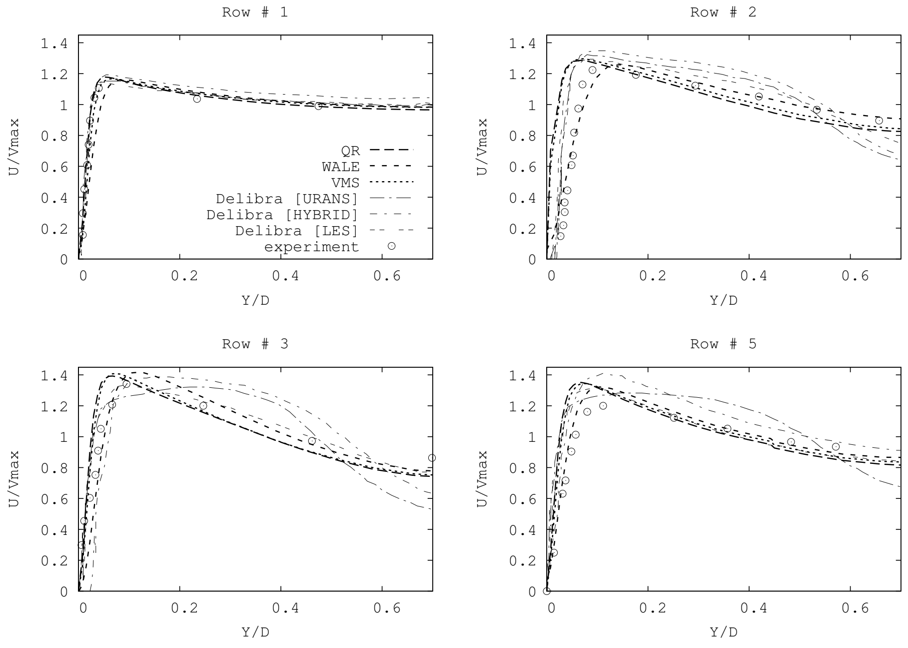

Figure 3.14: Mean velocity distribution between neighboring pins (line B) for $Re = 10000$. [URANS] data taken from [12]. [LES] and [HYBRID] data taken from [13]. Experimental data taken from [7].

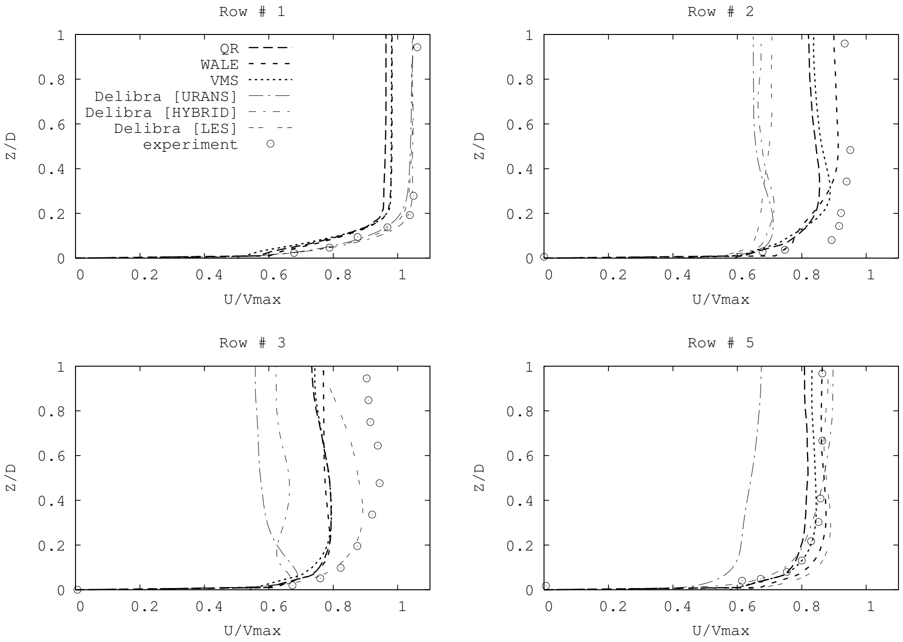

Figure 3.15: Mean velocity distribution in vertical midplane between neighboring pins (line A) for $Re = 10000$. [URANS] data taken from [12]. [LES] and [HYBRID] data taken from [13]. Experiment data taken from [7].

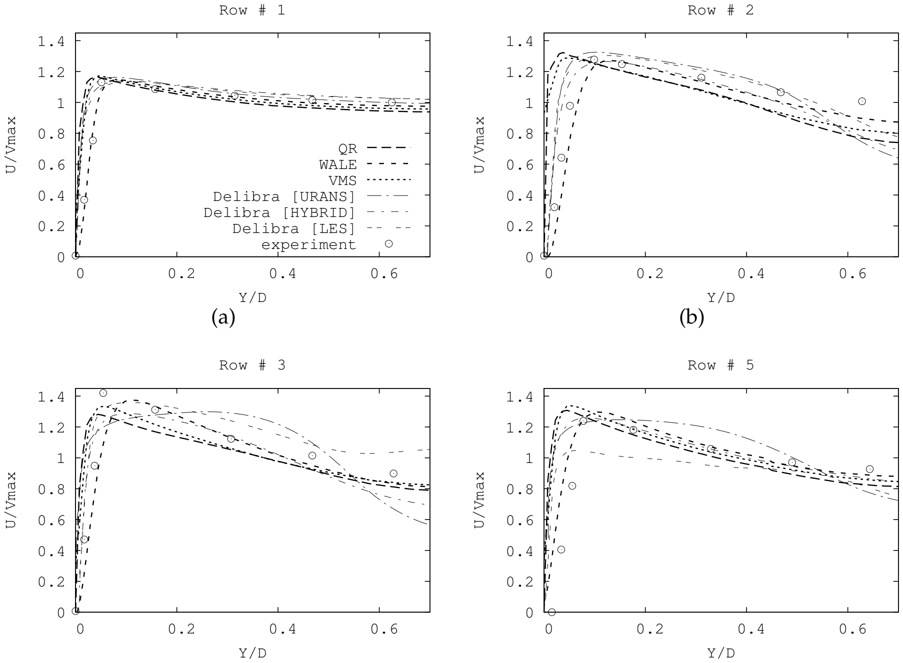

(a) (b) (c) (d)

Figure 3.16: Mean velocity distribution in the horizontal midplane between neighboring pins (line B) for $Re = 30000$. [URANS] data taken from [12]. [LES] and [HYBRID] data taken from [13]. Experiment data taken from [7].

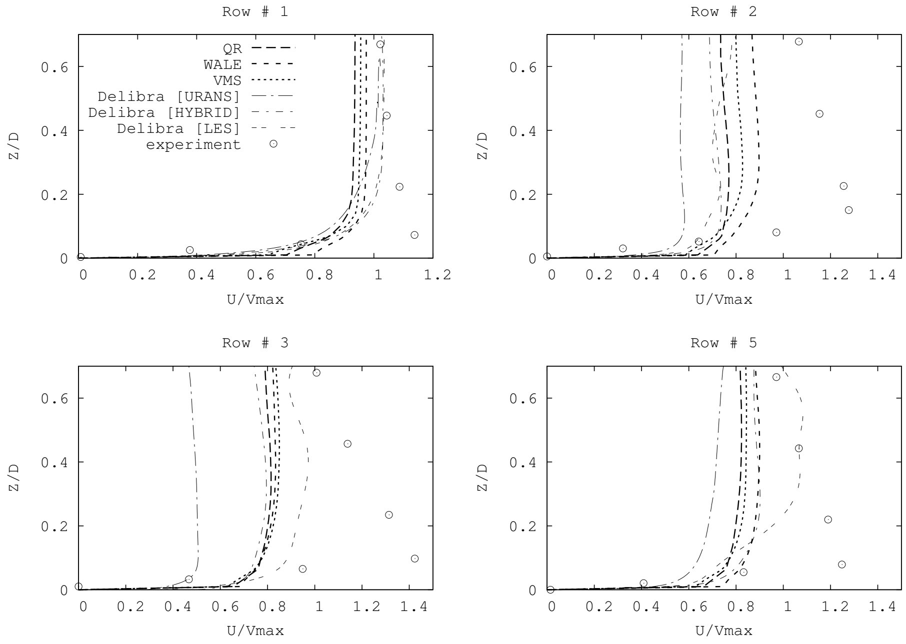

Figure 3.17: Mean velocity distribution in the vertical midplane between neighboring pins (line A) for $Re = 30000$. [URANS] data taken from [12]. [LES] and [HYBRID] data taken from [13]. Experiment data taken from [7].

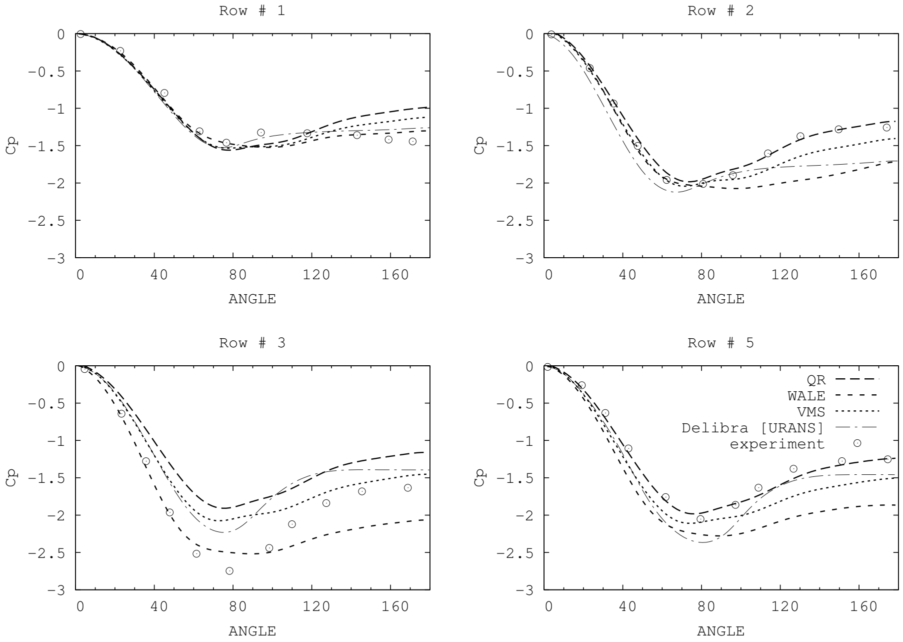

Figure 3.18: Distribution of pressure coefficients around pins (at z=D) for $Re = 30000$. [URANS] data taken from [12]. Experimental data taken from [6].

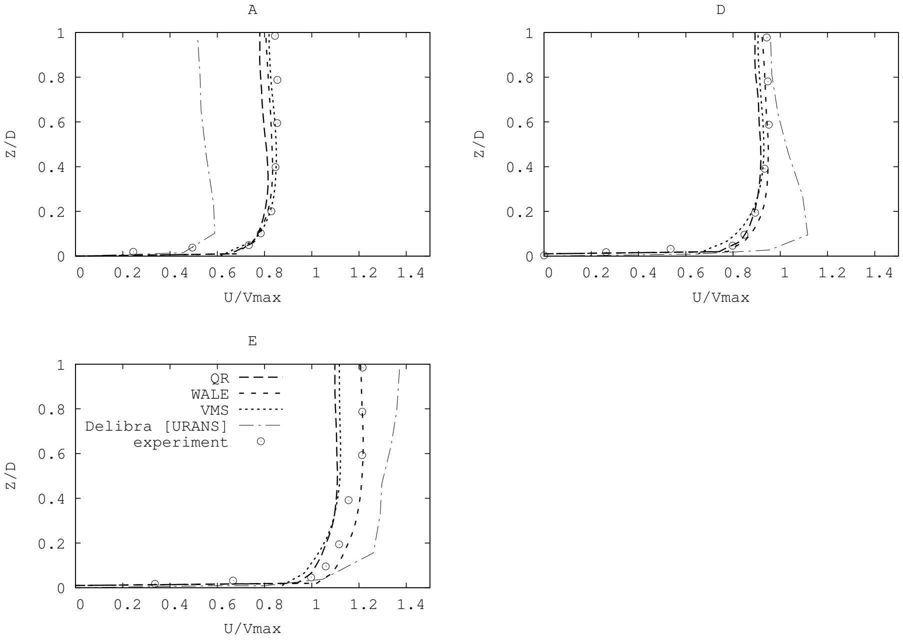

Figure 3.19: Mean velocity distribution in the vertical midplane between two pins of row 3 along lines A, D and E for $Re = 30000$. [URANS] data taken from [12]. Experiment data taken from [7].

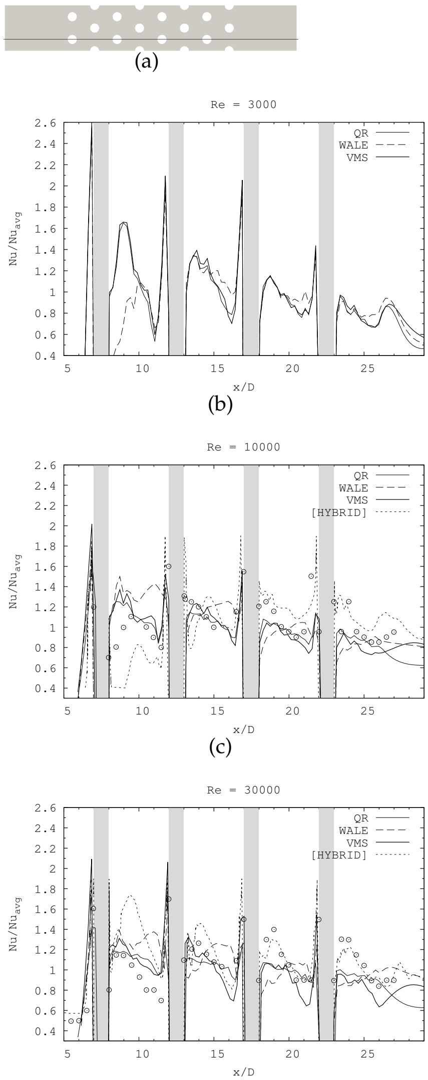

(a)

(b)

(c)

(d)

Figure 3.20: Distribution of Nusselt number along the cutline illustrated in a. b) $Re = 3000$, c) $Re = 10000$ and d) $Re = 30000$. [HYBRID] data taken from [13]. Points represent data taken from the experiment reported by [8].

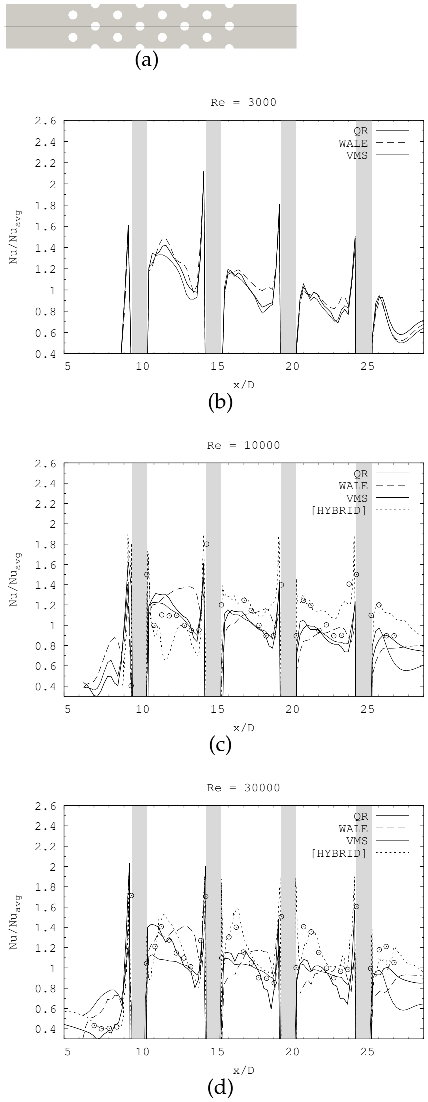

(a)

(b)

(c)

(d)

Figure 3.21: Distribution of Nusselt number along the cutline illustrated in a. b) $Re = 3000$, c) $Re = 10000$ and d) $Re = 30000$. [HYBRID] data taken from [13]. Points represent data taken from the experiment reported by [8].

3.5 Concluding remarks

Large-eddy simulation techniques were used to solve the flow and heat transfer in a relatively complex geometry (staggered matrix of cylindrical wall-bounded pins). In order to predict the broad spectrum of scale motions present in pin fin flow configurations, this paper aimed to compare three SGS models: QR eddy-viscosity model, Wall-adapting local eddy viscosity model (WALE) and WALE model within a variational multiscale framework (VMS-WALE). The three models used for this purpose were able to reproduce the bulk unsteady nature of the flow caused by vortex shedding downstream the pins. To validate the simulations, the experimental and numerical available data in literature were used.

The assessment included three different Reynolds numbers for study (3000, 10000 and 30000). As far as the authors knowledge is concerned $Re = 3000$ analysis had not been published until now. Despite the three models behaved similar between each other, pressure distribution around pins was in general better predicted by the QR eddy-viscosity model for the three Reynolds numbers studied on this paper. However, the velocity field of the channel was in better agreement with experimental results when WALE SGS model was applied for the simulations.

Thermal field was studied, qualitative and quantitative results were discussed. Averaged Nusselt number on one endwall was calculated and local distribution of Nusselt number on the endwall was illustrated. The results showed that the three SGS models had the ability for predicting fairly well the heat transfer on this kind of geometries if averaged values are needed. However, in the local study clear discrepancies between simulations and experiment are present, this different behavior was also found by other authors.

Capabilities of the three distinct LES SGS models (VMS, QR and WALE) were analyzed and the discrepancies between each other were discussed. Despite the three models were able to predict sufficiently good the flow characteristics on a wall bounded pin matrix, considering both hydrodynamic and thermal fields, WALE SGS model performed better in this kind of configurations.

It is important to emphasize that in the present study relatively coarse meshes were used and despite this, sufficiently good results were obtained. The realistic performance of the simulations can be attributed to the conjunction of the present conservative mathematical formulation and the tested LES SGS models. Because of this, a good part of the results presented were acceptable for the analysis of this particular problem, which is of great impact on industrial applications.

Even the industrial application of a pin fin array is very different to the applications of refrigerator fin and tube heat exchangers, the physics involved on the external part of both configurations share many relevant characteristics. Like the wakes generated behind the tubes, the development of 2 boundary layers at the leading edge of the fins and walls confining the fluid, the interaction of mixed fluid downstream with three dimensional structures like horseshoe vortices, etc. The acquired experience by the study of such interesting problems like flow and heat transfer in a pin fin matrix is very useful to address similar problems with different purposes like domestic refrigeration. Also, the selection of a SGS model for turbulent cases is supposed to be consistent for different usages when the flow presents turbulent or transition to turbulent characteristics. In conclusion, it was important to obtain clear information and understanding of the physics involved in the flow through this kind of geometries, specially under stringent conditions (high Re) in order to face the solution of different possible applications.

References

[1] J. K. Ostanek and K. A. Thole. Effect of streamwise spacing on periodic and random unsteadiness in a bundle of short cylinders confined in a channel. *Experiments in Fluids*, 53:1779–1796, 2012.

[2] S. C. Lau, Y. S. Kim, and J. C. Han. Effects of fin configuration and entrance length on local endwall heat/mass transfer in a pin fin channel. *ASME*, Paper 85-WA/HT-62, 1985.

[3] J-C. Han, S. Dutta, and Ekkad S. V. *Gas turbine heat transfer and cooling technology*. Taylor and Francis, New York., 2000.

[4] G. J. VanFossen. Heat-transfer coefficients for staggered arrays of short pin fins. *J. Eng. Power*, 104(2):268–274, 1982.

[5] M. K. Chyu, Y. C. Hsing, T. I. P. Shih, and V. Natarajan. Heat transfer contributions of pins and endwall in pin-fin arrays: Effects of thermal boundary condition modeling. *ASME J. Turbomach.*, 121:257–263, 1999.

[6] F.E. Ames, L.A. Dvorak, and M.J. Morrow. Turbulent augmentation of internal convection over pins in staggered pin-fin arrays. *ASME J. Turbomach.*, 127:183–190, 2005.

[7] F.E. Ames and L.A. Dvorak. Turbulent transport in pin-fin arrays: Experimental data and predictions. *ASME J. Turbomach.*, 128:71–81, 2006.

[8] F.E. Ames, C.A. Nordquist, and L.A. Dvorak. Endwall heat transfer measurements in a staggered pin-fin array with an adiabatic pin. In: Proc. GT2007. *ASME Turbo Expo 2007*, 2007.

[9] M. Labois and D. Lakehal. Very-Large Eddy Simulation (V-LES) of the flow across a tube bundle. *Nuclear Engineering and Design*, 241:2075–2085, 2011.

[10] S. A. Lawson, A. A. Thrift, K . A. Thole, and A. Kohli. Heat transfer from multiple row arrays of low aspect ratio pin fins. *Int. J. Heat Mass Transfer*, 54:4099–4109, 2011.

[11] S. Benhamadouche and D. Laurence. LES, coarse LES, and transient RANS comparisons on the flow across a tube bundle. *Int. J. Heat Fluid Flow*, 24:470–479, 2003.

[12] G. Delibra, D. Borello, K. Hanjalić, and F. Rispoli. URANS of flow and endwall heat transfer in a pinned passage relevant to gas-turbine blade cooling. *Int. J. Heat Fluid Flow*, 30:549–560, 2009.

[13] G. Delibra, K. Hanjalić, D. Borello, and F. Rispoli. Vortex structures and heat transfer in a wall-bounded pin matrix: LES with a RANS wall-treatment. *Int. J. Heat Fluid Flow*, 31:740–753, 2010.

[14] O. Lehmkuhl, A. Baez, I. Rodríguez, and C. D. Pérez-Segarra. Direct Numerical Simulation and Large-Eddy Simulations of the turbulent flow around a NACA-0012 airfoil. *7th International Conference on Computational Heat and Mass Transfer*, 2012.

[15] O. Lehmkuhl, R. Borrell, I. Rodríguez, C.D. Pérez-Segarra, and A. Oliva. Assessment of the symmetry-preserving regularization model on complex flows using unstructured grids. *Computers & Fluids*, 60:108–116, 2012.

[16] R. W. C. P. Verstappen. When does eddy viscosity damp subfilter scales sufficiently? *Journal of Scientific Computing*, 49(1):94–110, 2011.

[17] F. Nicoud and F. Ducros. Subgrid-scale stress modelling based on the square of the velocity gradient tensor. *Flow, Turbulence and Combustion*, 62:183–200, 1999.

[18] T. J. R. Hughes, L. Mazzei, and K. E. Jansen. Large eddy simulation and the variational multiscale method. *Computing and Visualization in Science*, 3:47–59, 2000.

[19] O. Lehmkuhl, C.D. Pérez-Segarra, R. Borrell, M. Soria, and A. Oliva. TERMOFLUIDS: A new parallel unstructured CFD code for the simulation of turbulent industrial problems on low cost PC cluster. *In Proceedings of the Parallel CFD 2007 Conference*, pages 1–8, 2007.

[20] R. W. C. P. Verstappen and A. E. P. Veldman. Symmetry-preserving discretization of turbulent flow. *Journal of Computational Physics*, 187:343–368, 2003.

[21] F. X. Trias and O. Lehmkuhl. A self-adaptive strategy for the time integration of Navier-Stokes equations. *Numerical Heat Transfer*, 60(2):116–134, 2011.

[22] C. M. Rhie and W. L. Chow. Numerical study of the turbulent-flow past an airfoil with trailing edge separation. *AIAA Journal*, 21:1525–1532, 1983.

[23] Y. Morinishi, T. S. Lund, O. V. Vasilyev, and P. Moin. Fully conservative higher order finite difference schemes for incompressible flow. *Journal of Computational Physics*, 143(1):90–124, 1998.

[24] F. N. Felten and T. S. Lund. Kinetic energy conservation issues associated with the collocated mesh scheme for incompressible flow. *Journal of Computational Physics*, 215(2):465–484, 2006.

[25] I. Rodríguez, O. Lehmkuhl, R. Borrell, and A. Oliva. Flow dynamics in the turbulent wake of a sphere at sub-critical Reynolds numbers. *Computers & Fluids*, 80:233–243, 2013.

[26] I. Rodríguez, R. Borrell, O. Lehmkuhl, C.D. Pérez-Segarra, and A. Oliva. Direct numerical simulation of the flow over a sphere at $Re = 3700$. *Journal of Fluid Mechanics*, 679:263–287, 2011.

[27] A. W. Vreman. The adjoint filter operator in large-eddy simulation of turbulent flow. *Physics of Fluids*, 16(6):2012–2022, 2004.

[28] D. E. Metzger, W. B. Shepard, and S. W. Haley. Row resolved heat transfer variations in pin fin arrays including effects of non-uniform arrays and flow convergence. *ASME*, (Paper No. 86-GT-132), 1986.

Chapter 4

Numerical Simulation of Heat Transfer and Fluid Flow Characteristics on Plain Fin and Tube Heat Exchangers

Abstract. In this Chapter, three dimensional fluid flow and conjugated heat transfer parameters over a flat plain fin and circular tube heat exchanger are numerically studied. The industrial problem to solve with three dimensional numerical simulations consists on ten rows of circular tubes in the longitudinal direction of the flow and two columns in the transversal direction with double fin spacing in the normal direction. Non uniform fin spacing is a geometrical characteristic commonly used for the ’no-frost’ evaporators in the refrigeration industry. Conjugated convective heat transfer in the flow field and heat conduction in the fins are considered. When the flow is found to be turbulent, Large Eddy Simulation (LES) methods are applied to solve the fluid characteristics. The numerical method is compared and validated against experimental data from Seshimo and Fujii [1] which correlation is applicable for geometries and flow regimes similar to the one that motivated the present research study.

4.1 Introduction

One of the most common devices used in HVAC&R (Heating, Ventilating, Air Conditioning, and Refrigeration) are the air cooled heat exchangers. Such equipments are frequently made of plain fins and a set of tubes (placed in staggered or inline arrangement) which pass perpendicularly through the plate fins. The heat exchanger can be composed with one or more tube rows and many different fin patterns such as wavy, plain, slit or louver can be used as heat transfer enhancements.

In compact heat exchangers, the thermal resistance is usually higher on the external zone if the fluid moving around the tubes is in gaseous state. It may reach even more than 80% of the total thermal resistance and therefore, the performance of the device is strongly related with the optimal design of this region. The total thermal efficiency of a heat exchanger may be considerably improved when optimizing the geometrical parameters (tube diameter, fin and tube pitches, staggered or inline arrangements, etc.) and the appropriate selection of different operating characteristics, such as fluid properties, inlet velocity, turbulence intensity among others.

The refrigeration power intake represents an important part of the total energy consumption around the world. Even though there are many different possibilities to upgrade the design options of refrigeration evaporators, diverse aspects like pressure drop and heat transfer performance have to be pondered in the conceptualization process.

Many research groups, have extensively studied the operation of these devices because of its great impact on industry. Diverse techniques have been used trying to understand better the flow features and the responsible mechanisms for the heat transfer over heat exchangers. As a result, several experimental and numerical models have been published in the past decades on this topic. Some interesting experimental researches are mentioned hereafter for a better understanding of the problem.

Seshimo and Fujii [1] experimentally studied the air side heat transfer and friction performance of plate fin and tube heat exchangers (mainly used in the region of relatively low Reynolds numbers ranging from 70 to 700). Their experimental results composed by 35 samples were correlated and effective generalized dimensionless correlations of the air side heat transfer and friction factor were obtained. They concluded that for $Re < 400$ for plain fins, the behavior of multiple row heat exchangers was similar to the single row characteristics.

Wang and Chi [2] presented an experimental study of the air side performance of fin and tube heat exchangers with plain fin configurations. They tested a total of 18 samples and examined the effect of the number of tube rows, fin pitch and tube diameter on the thermal hydraulic characteristics. Furthermore, they deeply analyzed previously published experimental data. They concluded that for small number of tube rows and low Reynolds numbers ($300 < Re < 3000$), the heat transfer performance was inversely related with the fin pitch. On a subsequent publication, Wang et al. [3] developed a correlation for fin and tube heat exchanger having plain fin geometry. They used 74 samples of different publications (including their own experiments) to develop a correlation, which had a mean deviation of the heat transfer of 7.51% and the friction correlation deviated up to 8.31%.

An interesting study focused on the data reduction method to obtain the air-side performance of fin and tube heat exchangers was presented by Wang et al. [4] in order to adequately correlate the available information. They recommended a standard procedure for dry surface heat transfer in finned tube heat exchangers having water on the tube side. Their major recommendations include the appropriate selection of the $\varepsilon - NTU$ relationship especially for the 1 row configuration. Also, for the friction factor they propose a correlation which disclaims calculation of the entrance and exit losses.

Moreover, the scientific community devoted to the topic investigated in the present Chapter, has used well known numerical tools such as Computational Fluid Dynamics (CFD), in order to simulate and predict the behavior of the flow and the heat transfer characteristics over heat exchangers. However, the real geometry and operating conditions of the heat exchangers are very complex, therefore many assumptions are usually made in order to develop the many different numerical models. One of the most common hypothesis made, is the constant solid wall temperature on the fin surfaces.

Jang et al. [5] studied both numerically and experimentally the fluid flow and heat transfer over a multi row (1-6 rows) plate fin and tube heat exchanger. They considered a three dimensional, laminar and incompressible flow for their simulations. The effects of different geometrical parameters such as tube arrangement, tube row numbers and fin pitch were investigated in detail for the Reynolds number ranging from 60 to 900. They concluded that the staggered array showed a better thermal performance with higher heat transfer coefficient than the inline arrangement. They also pointed out that the number of tube rows has a small effect on the average heat transfer coefficient if the row numbers are greater than 4.

He et al. [6] performed three dimensional simulations for laminar heat transfer and fluid flow characteristics of plate fin and tube heat exchanger. They examined the effect of different factors such as Reynolds number ($288 \leq Re \leq 5000$), fin pitch, tube row number and transversal or longitudinal tube pitch. Their numerical results were analyzed from the view point of field synergy principle, which according to their definition, says that the reduction of the intersection angle between velocity and fluid temperature gradient is the basic mechanism to enhance convective heat transfer. They recommended the use of enhancement techniques to further improve the convective heat transfer mainly in the rear part of the fin, where synergy between velocity and temperature gradient become worse. The analysis of their results, leads to the conclusion that Reynolds and Nusselt numbers are directly proportional, while Nusselt number and tube row number are inversely related (tube row number less than 3 is recommended).

However, the fin surface temperature is affected by the convection of the fluid around it and by the actual conduction of the fin material exchanging heat not only with the fluid but also with the tubes of the arrangement. By stepping forward in the objective of simulating the heat exchanger as realistic as possible specially in the design process, simulations taking into account convection and conduction for the temperature distributions of the domain are needed, therefore conjugate heat transfer formulations are required.

Jang et al. [7] presented experimental and numerical results for the fluid flow and heat transfer over four row circular finned tube heat exchangers with staggered arrangement. They investigated two types of finned tube configurations under the dry and wet conditions for different values of inlet frontal velocity ranging from 1 to $6m/s$ ($223 < Re < 1342$). In their numerical analysis they assumed laminar flow and solved both domains, i.e. fluid and solid regions.

Comini et al. [8] analyzed numerically the thermal performance for different Reynolds numbers from 250 to 1250 of a typical two row fin and tube heat exchanger, for both inline and staggered arrangements of tubes. In particular, fin performance was investigated in a broad range of operating conditions, both dry and wet. They took into account laminar flows and noticed that the convection coefficients and heat loads on the fins increase with the Reynolds number. Also, they found that fin efficiency decrease with increasing Reynolds number.

Because of the great variety of applications of fin and tube heat exchangers, different inlet velocities are found. In addition, the staggered configuration of the tube arrangement enhance the mixing of the fluid and under certain conditions, turbulent flow regime is commonly present . Some researchers have taken into account the turbulence effects by means of Reynolds Average Navier Stokes (RANS) approximations.

Mon and Gross [9] numerically studied the effects of fin spacing on four row annular finned tube bundles in staggered and inline arrangements. They presented conjugated heat transfer and pressure drop results for various fin spacings for a range of Reynolds number from 8.6×10^3 to 4.3×10^4. They also applied the RNG $\kappa - \varepsilon$ model to solve turbulence in the fluid region and concluded that when fin spacing is enlarged, heat transfer coefficient increases while pressure drop is reduced.

Shaeri and Yaghoubi [10] performed a numerical investigation for three dimensional fluid flow and convective heat transfer from an array of solid and perforated fins that were mounted on a flat plate. They simultaneously solved the conjugated differential equations for both solid and fluid (gas) domains, presenting results for Reynolds number in the range of 2×10^4 - 4×10^4. They used the $\kappa - \varepsilon$ model to solve turbulence in the fluid. They concluded that perforated fins have remarkable heat transfer enhancement in addition to the considerable reduction in weight by comparison with solid fins.

Barbosa et al. [11] performed CFD in order to study tube-fin 'no-frost' heat exchangers with forced convection on the air side and staggered tube configuration. For validation purposes, Barbosa et al. compared their simulations with experiments from Kays and London [12] for Reynolds ranging from 200 to 800. In their application study the volumetric flow rate was varied from 34 to $125m^3/h$. Given the intricated flow features, they also used for the simulations the $\kappa - \varepsilon$ model on the fluid domain. They used their simulations to assess the influence of geometric parameters such as the presence and position of the electrical heater coil relative to the tubes concluding that it strongly affects the main flow features. They also compared their results of continuous fins with an interrupted fin configuration in which the fins encompass two consecutive tube rows. Heat transfer was significantly increased with the interrupted fin configuration.

Perćić et al. [13] presented a numerical analysis of turbulent fluid flow and heat transfer on the air side and water side of plain fin and tube heat exchangers with non constant physical properties. Besides convection heat transfer on water and air sides, the heat conduction through pipe walls and fins was also considered in their study. They presented results for inline and staggered configurations of a three dimensional steady, turbulent (inlet velocity ranging from 10 to $20m/s$), incompressible fluid flow. The turbulence model used was a standard $\kappa - \varepsilon$ model. For the water side they imposed constant inlet parameters, while inlet values of the air side were varied. One of their main conclusion is that the air temperature at the entrance has greater effect on heat transfer than air velocity at the same boundary.

On the exhaustive study of the state of the art done for the present paper, only a few turbulent cases were found and, as mentioned above, those cases were solved by using RANS techniques. The present study uses the subgrid scale (sgs) WALE model for the turbulent cases (based on previous experience when similar geometries presented sufficiently good performance using that particular model [14]). Thus, allowing the analysis to capture in detail the complicated three dimensional structures like horseshoe vortices, and vortex shedding caused by the cylinders, in addition to the mixing of the flow caused by the staggered array and turbulence generated upstream. Large Eddy Simulation (LES) techniques have been used in the past years in order to understand the flow around similar geometries but for different applications such as pin fin matrices used to improve heat transfer over gas turbine blades [14–17]. Similar geometries under turbulent flow regime were presented in Chapter 3.

It is true that there is a large amount of previous publications regarding the study of fin and tube heat exchangers, however the problem within the industrial 'no-frost' applications, involves a very complex flow with many possible variants for the design and analysis. The air entering at the inlet zone of the heat exchanger is usually warm and humid coming from the refrigerator. The high humidity of the incoming air favors the formation of frosting/ice which is a characteristic that should be avoided. For that reason, double fin spacing is a good alternative to prevent frost clogging at the first rows of the evaporator. To the authors knowledge is concerned, there is few evidence that high performance numerical analysis over a geometry with double spaced fins has been performed. Shih [**?**] analyzed double fin spacing configurations although assuming constant temperature boundary conditions at the tubes and at the fins.

The transversal fin length is an important parameter for the design of the evaporator, hence the refrigerator. Any modification of this parameter implies a direct alteration of the useful volume of the device, thus changing the benefits offered to the consumer.

This Chapter focuses on the numerical simulation of conjugate heat transfer and fluid flow for industrial applications (refrigeration sector). LES methods have been applied in order to account for possible turbulence effects which are quantified and discussed. One of the main objectives of the present investigation is to assess the influence of the above mentioned geometric parameters (H and TP) and its behavior under different flow regimes (Reynolds number) on the thermal and hydraulic performance of 'no-frost' type heat exchangers.

4.2 Mathematical and numerical model

In this work, the proposed methodology is based on the numerical simulation of the characteristic domain of the heat exchanger by means of CFD using the inhouse TermoFluids software [18]. The problem is a three dimensional, pseudo-transient, turbulent fluid flow and conjugated heat transfer. Two sub-domains are defined to solve the conjugated problem, the solid sub-domain containing the solid fins; and the fluid sub-domain, which refers to the region where air is flowing around fins and tubes. The buoyancy and radiation effects are neglected in this problem.

4.2.1 Solid sub-domain

The solid sub-domain, is subdivided into multiple control volumes (CV) within which the energy transport equation is written as follows,

$$(\rho c_p)_s \frac{\partial T}{\partial t} + \lambda_s \mathrm{D} T = \mathbf{0} \tag{4.1}$$

where subscript s holds for solid, ρ is the density, c_p the heat capacity, λ the thermal conductivity, T is the temperature field and the diffusive operator for the temperature field is given by $\mathsf{D} = -\nabla^2$. M. Fiebig et al. [19] present the equations on their dimensionless form and report that the temperature distribution of the fin is described by the two dimensional heat conduction equation, which implies small Biot number. Biot number is the ratio of the heat transfer resistances inside of and at the surface of a body. It is used to determine whether or not the temperatures inside a body will vary significantly in space (normal direction in this case). By using this form of the energy equation, one important dimensionless number takes place (Eq. 4.2), it is the fin efficiency parameter.

$$Fi = \frac{\lambda_s}{\lambda_f}\frac{t_F}{P_F} \tag{4.2}$$

where the subscript f holds for fluid, t_F is the fin thickness and P_F is the fin spacing. For $Fi \to \infty$, the fin becomes isothermal and the fin efficiency η_F is unity.

4.2.2 Fluid sub-domain

The fluid sub-domain is divided into multiple CV on which the Navier-Stokes and energy equations (Eqs. 4.3, 4.4 and 4.5) are written and converted into algebraic equations using three dimensional unstructured collocated meshes and symmetry preserving schemes [20] as follows,

$$\begin{aligned}
\mathsf{M}\boldsymbol{u} &= \mathbf{0} && (4.3)\\
\frac{\partial \boldsymbol{u}}{\partial t} + \mathsf{C}(\boldsymbol{u})\,\boldsymbol{u} + \nu \mathsf{D}\boldsymbol{u} + \rho^{-1}\mathsf{G}\boldsymbol{p} &= \mathsf{C}(\boldsymbol{u})\,\boldsymbol{u} - \overline{\mathsf{C}(\boldsymbol{u})\,\boldsymbol{u}} &&\\
&\approx -\mathsf{M}\mathcal{T} && (4.4)\\
\frac{\partial T}{\partial t} + \mathsf{C}(\boldsymbol{u})\,T + \frac{\nu}{Pr}\mathsf{D}T &= \mathsf{C}(\boldsymbol{u})\,T - \overline{\mathsf{C}(\boldsymbol{u})\,T} &&\\
&\approx -\mathsf{M}\mathcal{T}_T && (4.5)
\end{aligned}$$

where $\boldsymbol{u}$ and $\boldsymbol{p}$ are the velocity and pressure fields, respectively. ν is the kinematic viscosity and ρ the density. Convective operator in the momentum equation for the velocity field is given by $\mathsf{C}(\boldsymbol{u}) = (\boldsymbol{u} \cdot \nabla)$. Gradient and divergence operators are given by $\mathsf{G} = \nabla$ and $\mathsf{M} = \nabla\cdot$, respectively. $\mathcal{T}$ is the SGS stress tensor, which is defined as:

$$\mathcal{T} = -2\nu_{sgs}\overline{\mathcal{S}_{\mathsf{ij}}} + (\mathcal{T} : \mathsf{I})\mathsf{I}/3 \tag{4.6}$$

where ν_{sgs} is the subgrid-scale viscosity, and $\mathcal{S}_{\mathsf{ij}}$ is the stress tensor defined as $\overline{\mathcal{S}_{\mathsf{ij}}} = \frac{1}{2}\left[\mathsf{G}(\boldsymbol{u}) + \mathsf{G}^{*}(\boldsymbol{u})\right]$, where G^{*} is the transpose of the gradient operator. $\mathcal{T}_T$ term is evaluated as in $\mathcal{T}$ term, but ν_{sgs} is substituted by ν_{sgs}/Pr_T, where Pr_T is the turbulent Prandtl number (0.4 in this paper).

As aforementioned, numerical schemes used are conservative, i.e., they preserve the kinetic energy equation. These conservation properties are held if and only if the discrete convective operator is skew-symmetric ($\mathsf{C}\left(\boldsymbol{u}\right) = -{\mathsf{C}_{\mathsf{c}}}^{*}\left(\boldsymbol{u}_c\right)$), the negative conjugate transpose of the discrete gradient operator is exactly equal to the divergence operator ($-\left(\Omega_c \mathsf{G}_c\right)^{*} = \mathsf{M}_c$), and the diffusive operator D_c is symmetric and positive-definite (the subscript *c* holds for the cell-centered discretization, and the subscript *s* holds for the staggered faces). These properties ensure both stability and conservation of the kinetic-energy balance even at high Reynolds numbers and with coarse grids.

A fractional-step method is applied to solve the momentum Eq. (4.4). The time-integration method chosen for the convective and diffusive terms is a two-step linear explicit scheme, while for the pressure gradient term an implicit first-order scheme is used [21].

The velocity-pressure coupling is solved by means of a classical fractional-step projection method, $\boldsymbol{u}_c^p = \boldsymbol{u}_c^{n+1} + \mathsf{G}\tilde{\boldsymbol{p}}_c$, where $\tilde{\boldsymbol{p}}_c = \boldsymbol{p}_c^{n+1}\Delta t^n/\rho$ is the pseudo-pressure, $\boldsymbol{u}_c^p$ is the predicted velocity, $n+1$ is the instant where the temporal variables are calculated, and Δt^n is the current time step ($\Delta t^n = t^{n+1} - t^n$). Taking the divergence of $\boldsymbol{u}_c^p$ and applying the incompressibility condition yields a discrete Poisson equation for $\tilde{\boldsymbol{p}}_c$: $\mathsf{L}_{\mathsf{c}}\tilde{\boldsymbol{p}}_c = \mathsf{M}_c\boldsymbol{u}_c^p$. The discrete Laplacian operator L_{c} is, by construction, a symmetric positive definite matrix ($\mathsf{L}_{\mathsf{c}} \equiv \mathsf{M}\Omega^{-1}\mathsf{M}^{*}$).

Finally, the mass-conserving velocity at the faces ($\mathsf{M}_s\boldsymbol{u}_s^{n+1} = 0$) is obtained from the correction, $\boldsymbol{u}_s^{n+1} = \boldsymbol{u}_s^p - \mathsf{G}_s\tilde{\boldsymbol{p}}_c$, where G_s represents the discrete gradient operator at the CV faces. This approximation allows to conserve mass at the faces but it has several implications. If the conservative term is computed using $\boldsymbol{u}_s^{n+1}$, in practice an additional term proportional to the third-order derivative of $\boldsymbol{p}_c^{n+1}$ is introduced. Thus, in many aspects this approach is similar to the popular Rhie and Chow [22] interpolation method and eliminates checkerboard modes.

However, collocated meshes do not conserve the kinetic energy as shown by Morinishi et al. [23] for finite-difference schemes and by Felten and Lund [24] for finite-volume schemes. When the fractional-step method on a collocated arrangement is used, there are two sources of errors in the kinetic energy conservation: i) due to interpolation schemes and, ii) due to inconsistency in the pressure field in order to ensure mass conservation. While the first one can be eliminated through the use of conservative schemes such as those used in the present work, the latter equals to $\epsilon_{\mathbf{ke}} = (\tilde{\boldsymbol{p}}_c)^{*}\mathsf{M}_c(\mathsf{G}_c - \mathsf{G}_s)\tilde{\boldsymbol{p}}_c$. This contribution of the pressure gradient term to the evolution of the kinetic energy can not be eliminated. Felten and Lund [24] have conducted a study to determine its scaling order. They have shown that the spatial term of the pressure error scales as $\mathcal{O}(\triangle x^2)$ and the temporal term scales as $\mathcal{O}(\triangle t)$, i.e., pressure errors are of the order of $\mathcal{O}(\triangle x^2 \, \triangle t)$. However, it has been proved that pressure errors do not have a significant impact on the results at grid resolutions and time-steps used in both LES and Direct Numerical Simulation (DNS) [25–27].

Based on previous experience working with similar geometries [14], authors have found that WALE SGS model has a good performance for predicting the hydrodynamic and thermal fields in configurations of wall bounded pin matrix. For this reason, such closure is used for modeling the small scales of turbulence when the flow structures do not show clear laminar behavior. A brief description of WALE model is given hereafter:

Wall-adapting local eddy viscosity model (WALE)

This model proposed by Nicoud and Ducros [28] is based on the square of the velocity gradient tensor. In their formulation the SGS viscosity accounts for the effects of both the strain and the rotation rates of the smallest resolved turbulent fluctuations. In addition, the proportionality of the eddy viscosity near walls ($\nu_{sgs} \propto y^3$) is recovered without any dynamic procedure.

$$\begin{aligned} \nu_{sgs} &= (C_w \Delta)^2 \frac{(\mathcal{V}_{\mathsf{ij}} : \mathcal{V}_{\mathsf{ij}})^{\frac{3}{2}}}{(\overline{\mathcal{S}_{\mathsf{ij}}} : \overline{\mathcal{S}_{\mathsf{ij}}})^{\frac{5}{2}} + (\mathcal{V}_{\mathsf{ij}} : \mathcal{V}_{\mathsf{ij}})^{\frac{5}{4}}} \qquad (4.7) \\ \mathcal{V}_{\mathsf{ij}} &= \frac{1}{2}[\mathsf{G}(\overline{\boldsymbol{u}_c})^2 + \mathsf{G}^*(\overline{\boldsymbol{u}_c})^2] - \frac{1}{3}(\mathsf{G}(\overline{\boldsymbol{u}_c})^2 \mathsf{I}) \end{aligned}$$

In our studies a value of $C_w = 0.325$ is used according with the procedure recommended by Nicoud and Duros [28].

4.3 Validation of the numerical model

4.3.1 Definition of the validation case

In order to validate the presented conjugated heat transfer framework one independent case for which experimental values are available has been chosen as benchmark. The criteria for choosing the validation problem is based on the coincidence of the dimensionless Reynolds and Prandtl numbers. Also a good approximation of the geometry to the real domestic refrigeration application case is desired. Particularly *"sample No. 35"* from all the geometries included on the experiments from Seshimo and Fujii [1] presents a particularly considered large fin pitch, tube diameter and equilateral triangular tube arrangement which is usually applied on 'no-frost' evaporators for domestic refrigerators. For such reason, and given the relevance of Seshimo's work on this field contributing reliable correlations these experimental data is chosen as benchmark for the simulations performed by the authors. As can be seen from the publication of Wang et al. [3], the chosen correlation for comparison has very acceptable agreement with the results obtained by some other authors (Fig. 4.1).

Seshimo and Fujii [1] experimentally studied 35 plate fin and tube heat exchangers with systematically changed geometrical parameters. Their study included plain fins and fins with ring depression around the tubes. The correlations presented by them are for staggered arrangements composed by one and up to five tube rows. The specific geometry *"sample No. 35"* included by them is formed by 2 rows of cylindrical tubes of $9.52mm$ of diameter, longitudinal tube pitch of $22.0mm$, transversal tube pitch of $25.4mm$, and constant fin pitch of $6.0mm$. The range of applicability of their correlation is $70 < Re < 700$ for fins with ring depression and $Re < 400$ for plain fins, (geometrical details are schematically shown in Fig. 4.2). Experimental results correspond to samples made of copper tubes, with fins of 0.12mm thick aluminum plates joined to the tubes with a mechanical tube expansion which causes a ring depression on the fin around the tubes. However, Seshimo and Fujii present results for both plain fins and with ring depression. Present simulations assumed plain fins.

Based on previous experience for channel flow simulations, extra computational domain at the inlet and outlet regions of the fluid domain is added to the real heat exchanger geometry as shown in Fig. 4.3 in order to avoid numerical uncertainties and possible divergence on the final results. Nevertheless, for the analysis of the steady final results only the domain of the heat exchanger is taken into consideration.

Simulations have been performed for Reynolds numbers of 50, 300 and 550 (definition of Re based on inlet velocity and tube diameter). Homogeneous flow is assumed as the initial condition of all simulations. Boundary conditions are illustrated on Fig. 4.4 and are prescribed as follows: uniform velocity and temperature prescribed at the channel inlet ($T_{in} = T_C$, where T_C holds for cold temperature), pressure based at the outlet, three dimensional periodic conditions are used for the boundary planes at the transversal direction, the tubes and fin solid walls have non-slip conditions for the velocity and constant temperature is imposed at the tube walls ($T_{cyl} = T_H$, where T_H holds for hot temperature). Finally, the fin wall is thermally evaluated with two different treatments. First, constant wall temperature is assumed ($T_{fin} = T_H$) and second, at the solid-fluid interface, heat convection to the fin and heat conduction in the fin are considered, i.e. conjugated heat transfer is evaluated.

The numerical analysis of the present work has been performed in three different stages: a) Air thermophysical fluid properties are used to solve the dimensional Navier Stokes equations with fin wall temperature set constant ($T_{fin} = T_H$). b) Ficti-

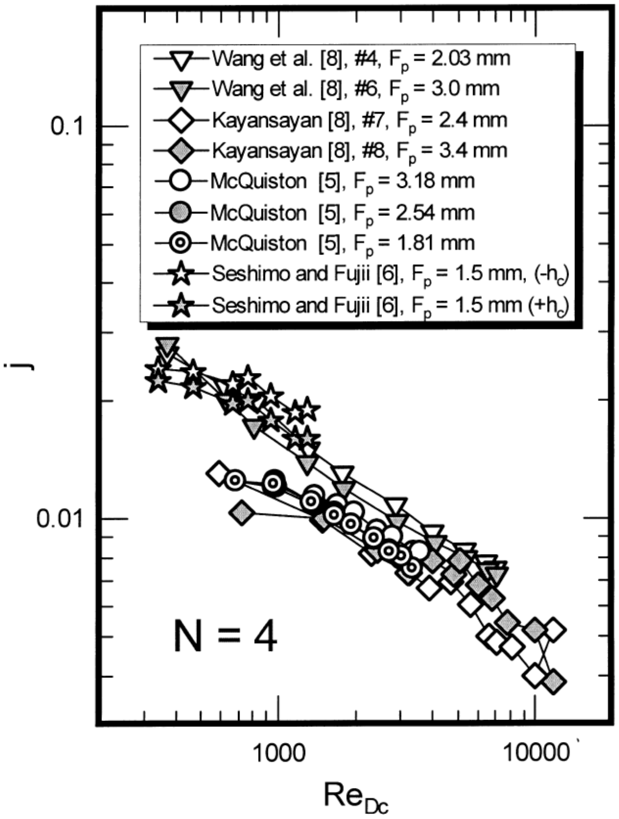

Figure 4.1: Comparison of *j* values between test samples by different authors [3].

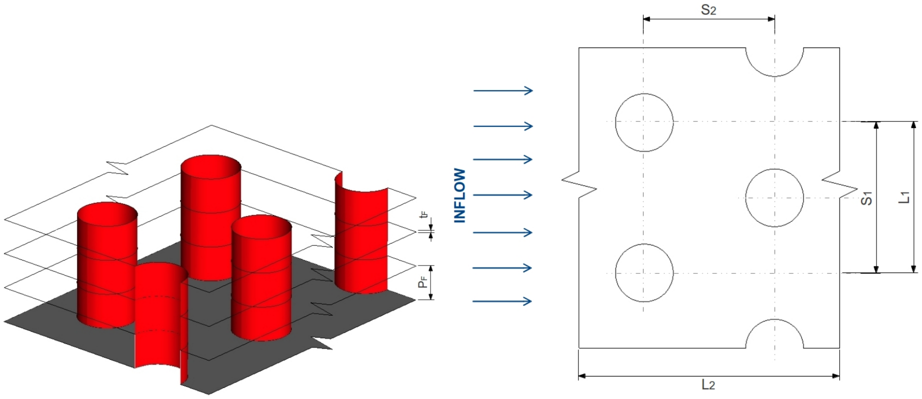

Figure 4.2: Schematic view of the selected sample from experimental data presented by Seshimo and Fujii [1].

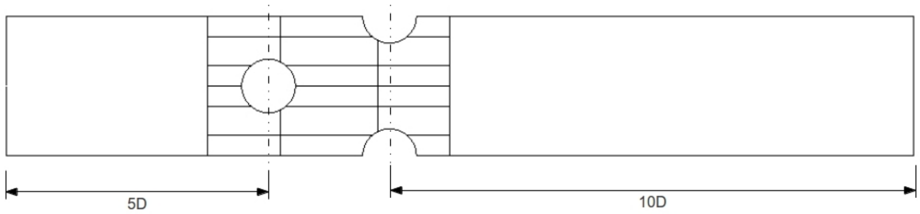

(a)

Figure 4.3: Representation of the used computational domain for all the simulations of the validation cases.

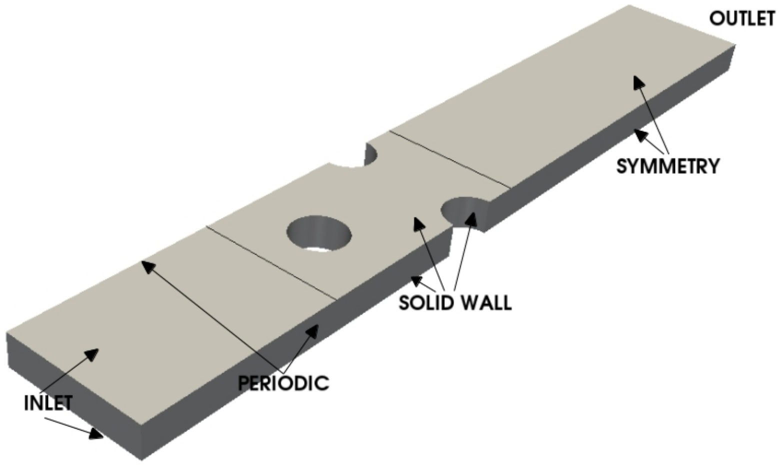

(a)

Figure 4.4: Boundary conditions and geometry of the verification case.

tious fluid and solid thermophysical properties are imposed always maintaining the characteristic dimensionless parameters constant, i.e., Re, Pr, λ_{sf} and α_{sf} (defined by Eqs. 4.8 and 4.9) were kept equal to the ones obtained with air and aluminum physical properties, while new "imaginary" fluid and solid physical properties are recalculated and used on the solution of the Navier Stokes equations (with fin wall temperature set constant, $T_{fin} = T_H$). Finally, a third and final stage is proposed and tested: c) Since the real phenomena occurs with fins exchanging energy with the fluid and the tube solid walls, Navier Stokes equations with properties of "imaginary" fluid and solid are coupled to solve the conjugated heat transfer problem at the shared interface.

$$\lambda_{sf} = \frac{\lambda_s}{\lambda_f} \tag{4.8}$$

$$\alpha_{sf} = \frac{\alpha_s}{\alpha_f} \tag{4.9}$$

As a result from the three stages analyzed, the authors conclusion is that the third alternative is recommended for cases with similar thermal characteristics, i.e. similar applications for refrigeration industry.

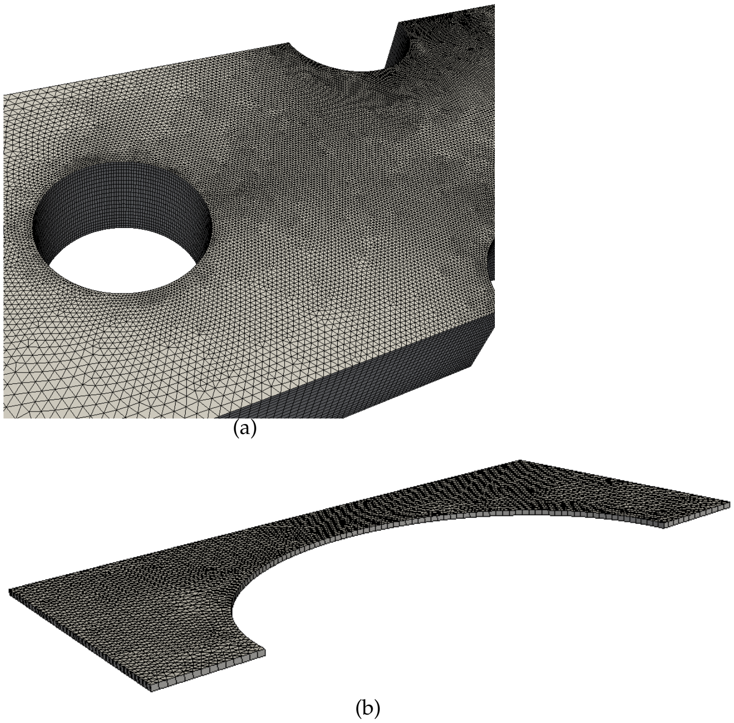

Figure 4.5: Mesh used for the discretization of the 3D domains a) Fluid, and b) Solid fin.

Mesh Information

The mesh for the validation case is designed with the basis of previous experience gained on the solution of similar complex problems like the ones described on Chapters 2 and 3. The same mesh was used for the simulations regardless the Reynolds number under analysis because of the low frontal velocity implied. Designing and building an appropriate mesh requires time and effort, thus if the conditions of the flow are similar between each other one single mesh can be used. Fig. 4.5 illustrates the final mesh applied for the discretization of the domains.

Meshes are unstructured and matched at the interface between solid and fluid. In the regions close to solid walls (fins or tubes) the grid is carefully densified to ensure the correct solution of velocity and temperature boundary layers. In the normal direction (from one fin to the next one), 4CV are placed inside the boundary layer thickness ($Re = 59.8$) while 2CV are found on the same zone for $Re = 359.0$ and 658.1. Experience from previous numerical simulations for similar geometries indicates that the most critical part for heat exchanger analysis are the tubes because of the physics involved around them. Hence, a big part of the available computational resources is used in the discretization of the flow close to the cylinders. For the highest Reynolds number, 3 to 4 CV are placed to solve the boundary layer around the tubes, while for the lower Reynolds case up to 10 CV are counted. The most demanding case is $Re = 658.1$ and mesh is designed in order to obtain sufficiently accurate results for it. The mesh for the solid domain directly applies the thin fin hypothesis neglecting the temperature difference in the normal direction, therefore, only one CV is placed.

4.3.2 Data Reduction

Results obtained from the numerical simulations are analyzed following the same criteria as Seshimo and Fujii [1]. The overall heat transfer coefficient K is defined by Eq. 4.10, where $[LMTD]$ is the logarithmic mean temperature difference on counter flow. Correction factor F is assumed to be one because the tubes are set with constant wall temperature in the simulations. A_0 represents the total air side heat transfer surface and $\dot{Q}$ is the heat transfer rate ($\dot{Q} = \dot{m}c_p(T_{out} - T_{in})$).

$$\dot{Q} = A_0 \cdot K \cdot F \cdot [LMTD] \tag{4.10}$$

The air side average heat transfer coefficient is defined by Eq. 4.11. Where the last two terms from the right hand of the equation are neglected since perfect contact between fin and tubes is assumed and constant wall temperature is imposed at the tube solid walls (subscript i holds for inside of tubes and subscript c holds for contact between fins and tubes). A_F is the area of the fins, η is the fin efficiency, h is the average heat transfer coefficient.

$$\frac{1}{K} = \left(\frac{A_0}{A_T + \eta A_F}\right) \cdot \frac{1}{h} + \frac{A_0}{A_i h_i} + \frac{A_0}{A_c h_c} \tag{4.11}$$

Fin efficiency is obtained by Eq. 4.12 which is based on the assumption of the annular fins with uniform heat transfer coefficient. Df represents the equivalent diameter of the fin and its defined by $Df = (4/\pi S_1 S_2)^{0.5}$, Dc is the fin collar diameter ($Dc = D + 2t_F$, t_F being the fin thickness).

$$\eta = 1 - h \cdot \frac{(Df - Dc)^2}{6\lambda_F t_F} \cdot \left(\frac{Df}{Dc}\right)^{0.5} \tag{4.12}$$

The characteristic parameters for the definition of the dimensionless numbers are not assumed by the means of the velocity at the minimum flow area and tube diameter as usual. In the range of low frontal velocity, Seshimo and Fujii found that consideration of the entrance region is important for processing the characteristics of heat exchangers with small number of tube rows. Following the same criteria used for the analysis of experimental results from Seshimo, imaginary mean velocity v_m (Eq. 4.13), i.e. the velocity of imaginary free flow area A_m (Eq. 4.14) is used as the characteristic velocity, and the hydraulic diameter De_m as a characteristic length (Eq. 4.15).

$$v_m = \frac{A_{fr} v_{fr}}{A_m} \tag{4.13}$$

$$A_m = \frac{A_{fr}(P_F - t_F)(S_1 S_2 - \pi Dc^2/4)}{P_F S_1 S_2} \tag{4.14}$$

$$De_m = \frac{4 A_m L_2}{A_0} \tag{4.15}$$

A_m is the total volume of the heat exchanger minus the volume of the tube bank and divided by fin length L_2, thus expressing an imaginary free flow cross sectional area. Therefore v_m is the characteristic velocity assuming a relatively small influence from the tube bank. With the geometrical characteristic values properly defined, dimensionless numbers are expressed by Eqs. 4.16, 4.17 and 4.18.

$$Nu = \frac{h De_m}{\lambda_{air}} \tag{4.16}$$

$$Re = \frac{v_m De_m}{\nu_{air}} \tag{4.17}$$

$$f = \frac{De_m}{2 L_2 \rho_{air} {v_m}^2} \cdot \Delta P \tag{4.18}$$

4.3.3 Comparison with experiments

With the results of the 35 samples, Seshimo and Fujii [1] obtained their own correlations for the air side heat transfer and pressure drop characteristics for single and two row configurations with a ring depression. The correlations are expressed by Eqs. 4.19 and 4.20 for one row, and for two row configuration Eqs. 4.21 and 4.22 are suggested.

$$\begin{aligned} Nu &= 2.1(Re \cdot Pr \cdot De_m/L_2)^{0.38} && (4.19) \\ f \cdot L_2 De_m &= 0.43 + 35.1(Re \cdot De_m/L_2)^{1.07} && (4.20) \end{aligned}$$

$$\begin{aligned} Nu &= 2.1(Re \cdot Pr \cdot De_m/L_2)^{0.47} \quad (4.21)\\ f \cdot L_2 De_m &= 0.83 + 24.7(Re \cdot De_m/L_2)^{0.89} \quad (4.22) \end{aligned}$$

The range of applicability for those correlations is $70 < Re < 700$ (Re defined by Eq. 4.17). Studying the publication of Seshimo in detail, they found that in the range of low frontal air velocity, the effect of ring depression on the fins is negligible for the heat transfer performance. They also found that in the range of Reynolds number smaller than 400 for plain fins (and 160 with a ring depression) the characteristics of multiple rows devices agree with the single row correlation. The results obtained by the present numerical simulations also confirm this observation. The global data reduction from the present numerical simulation results, with the conjugated stage of analysis mentioned above are compared with the correlations of Seshimo and Fujii in Fig. 4.6 (experimental data points are included on the figure). It is important to point out the good agreement between the results obtained by the author and the experimental data points corresponding to the same case of plain fins with two rows of tubes. Good concordance is visible for the numerical results with the one row correlation. Given this acceptable results, it can be assumed as a good alternative to solve the Navier Stokes equations rearranging the fluid and solid physical properties in convenience attempting to save computational costs that can be harnessed at the extra costs inherent to the domain communications of the conjugated treatment.

The simulations and the experiments cannot reproduce exactly the same case because simulation assumed perfect contact between fins and tubes, neglecting the thermal resistance from the contact area. Also in the numerical study the tube is set at a constant temperature which represents the case of ideal convection between inside fluid (usually water) and the tube surface. Additionally the experimental measurements by themselves have inherent uncertainties that in conjunction with the numerical hypothesis can explain the small discrepancies between both research methods.

For this cases, the analysis of each row was made and the expected tendency of higher Nusselt number for the first row was confirmed.

4.3.4 Detailed analysis of CFD simulations

Local profiles of different important result variables were obtained and compared for three different Reynolds numbers (50, 300 and 550). Dimensionless mean bulk temperature ($T_m^* = \frac{T_m - T_C}{T_H - T_C}$) is shown in Fig. 4.7. T_m is defined by Eq. 4.23.

$$T_m = \frac{\int uTdA}{\int udA} \quad (4.23)$$

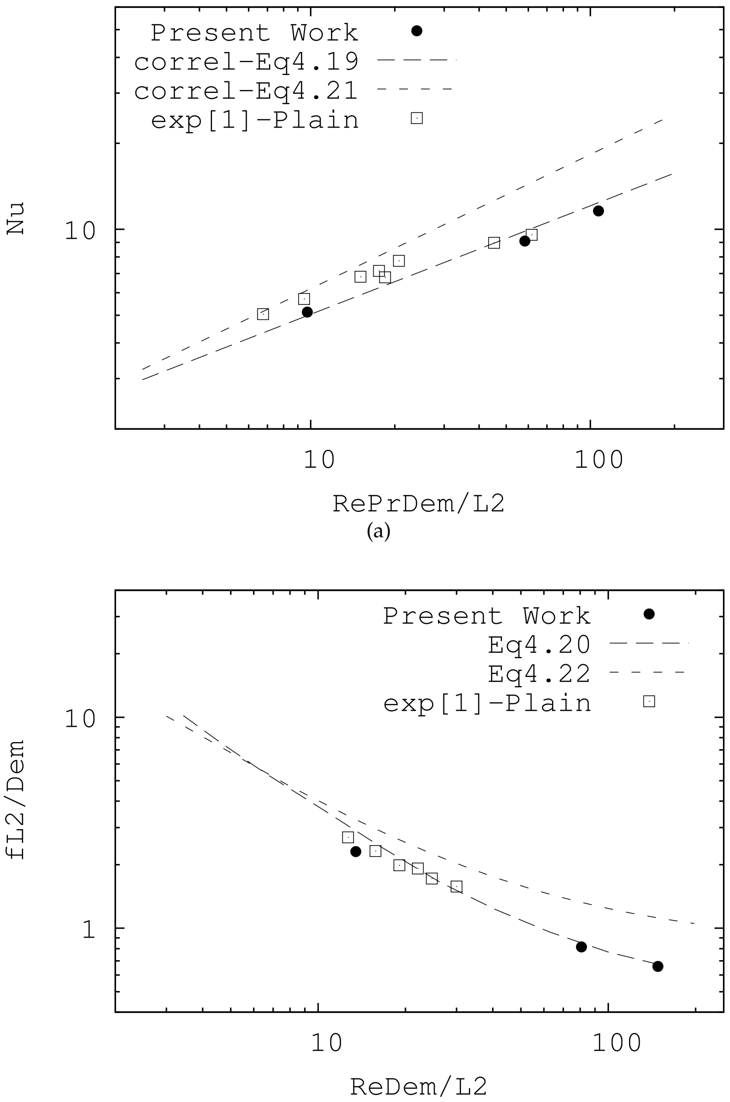

(a)

(b)

Figure 4.6: Friction factor and heat transfer characteristics compared against experimental available data.

The proportional relation between inlet velocity and Reynolds number leads to hotter fluid flow at the lowest Re for steady state results. Thus, higher heat transfer will occur for larger Reynolds numbers given the increased temperature difference between the fluid and the solids. Following the same criteria, higher heat transfer will occur when the fin is assumed to be at a uniform (hot) temperature representing an infinite heat transfer coefficient.

Dimensionless heat transfer rate defined in Eq. 4.24 evaluated at the fin surfaces and at the cylinder solid walls are depicted in Fig. 4.8 and 4.9 respectively. The thermal boundary condition at the cylinders is always set at a constant temperature (T_H), but for the fins there are two different treatments analyzed in order to compare the ideal case of a fin with $Fi \rightarrow \infty$. As expected, higher heat transfer is accounted at the fins with the ideal hypothesis. However the real conditions of finite λ needs to be carefully understood when a good and reliable design is the main purpose.

$$\dot{Q}^* = \frac{\partial T}{\partial n} \frac{De_m}{T_H - T_C} \tag{4.24}$$

Comparison between flow regimes, Fig. 4.8 and 4.9 show the local behavior that justifies the highest Nusselt number at $Re = 550$ in the global analysis. Fig. 4.8 shows very high heat transfer rate at the entrance of the heat exchanger and at the impingement of the cylinders. It is very useful and illustrative to compare the local distribution of diverse heat transfer and flow features for this kind of equipments in order to visualize the regions where the heat transfer is specially enlarged. The wake behind the first row of tubes gets thinner at higher Reynolds number and horseshoe vortex structures are clearly represented in the figure.

The fluid exchanges energy not only with the fins but with the tubes that are set at uniform hot temperature. Heat transfer rate is significantly more important at the impingement zone where the cold fluid hits the bank of tubes. The big temperature difference present between solid tube walls and fluid flow produces elevated heat transfer rates at this region. This effect is represented in Fig. 4.9. In this figure, the thermal boundary layer thickness caused by the fins can be deduced qualitatively at the top and bottom of the tubes. It is definitely much thinner at the highest flow regime which indicates that by the time the flow hits the first tube row is still under development and for that reason higher heat transfer is expected at this point. Such detailed information can only be obtained by this top order simulation techniques, thus the relevance of the motivation for the present research work.

Given the relevance of the information obtained for heat transfer global analysis on the final application, comparison of the total dimensionless heat transfer rate (with all the solids of the domain, fins and tubes) and the heat transfer caused only by the fins is quantified on Table 4.1. Global fin efficiency which is considered to be a very relevant parameter for design purposes is also quantified. For the geometry under analysis, the ratio of fin area against the total heat transfer area $A_F/A_0 = 0.843$,

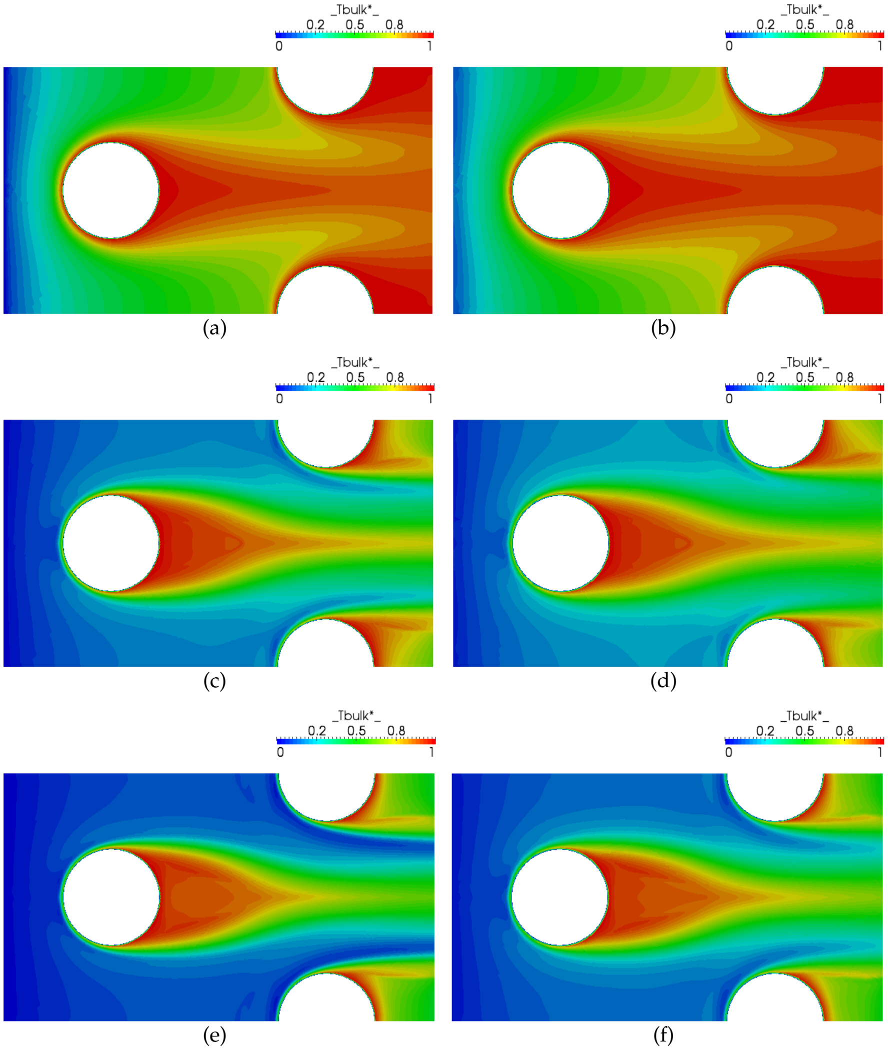

Figure 4.7: Dimensionless mean bulk temperature profiles for top: $Re = 50$, center: $Re = 300$ and bottom: $Re = 550$. Left: conjugated treatment of the heat transfer problem at the interface between solid and fluid. Right: isothermal fin is assumed as boundary condition.

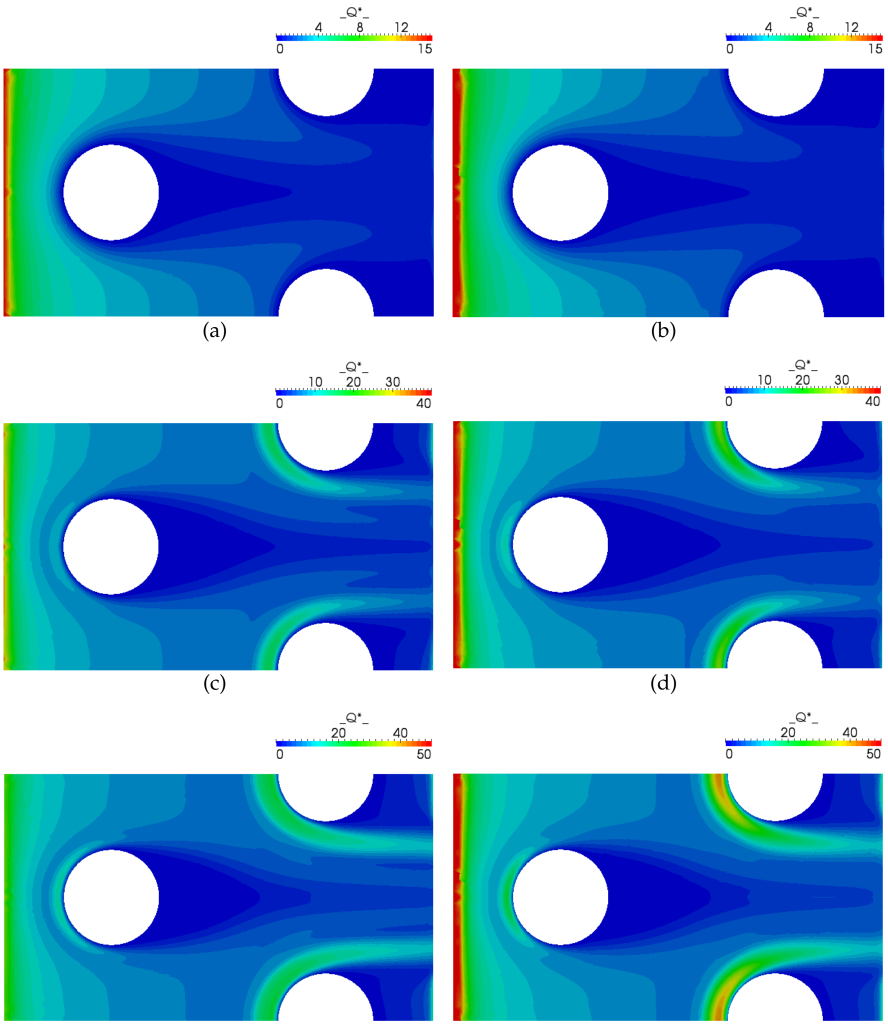

(a) (b)

(c) (d)

(e) (f)

Figure 4.8: Dimensionless heat transfer rate profiles for top: $Re = 50$, center: $Re = 300$ and bottom: $Re = 550$ at the fins surfaces. Left: conjugated treatment of the heat transfer problem. Right: isothermal fin hypothesis is assumed.

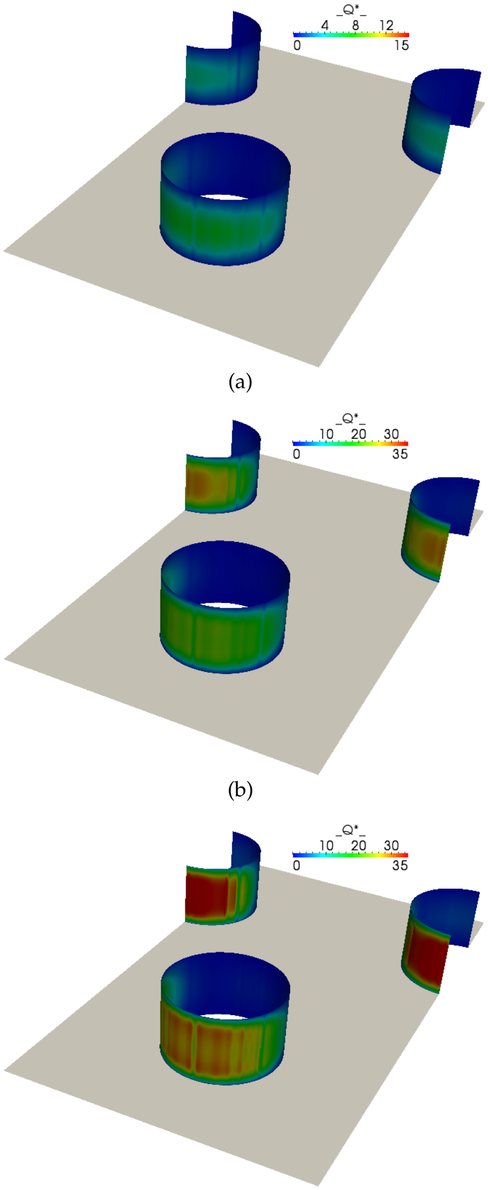

(a)

(b)

(c)

Figure 4.9: Dimensionless heat transfer rate profiles for a) $Re = 50$, b) $Re = 300$ and c) $Re = 550$ at the tubes.

Table 4.1: Fin efficiency and dimensionless heat transfer rate due to all solids and due only to the fins ($Q^*_{ratio} = \frac{Q^*_{fins}}{Q^*_{solids}}$).

	Re	Q^*_{solids}	Q^*_{fins}	Q^*_{ratio}	η_{fin}
Conjugated	59.83	4858.97	4201.45	0.865	0.918
	359.00	14907.55	11660.35	0.782	0.880
	658.17	20350.17	15798.67	0.776	0.815

thus the heat transfer rate due to the fins is expected to be significantly bigger than the one quantified by the tubes surfaces.

It is interesting to analyze the local distribution of the Nusselt number at the plain fin surface in order to understand the physics of the convective heat transfer process under diverse flow regimes. Fig. 4.10 is intended to illustrate such details, namely: a) development of the boundary region at the inlet zone with the highest Nusselt number of the domain, b) tube vortex recirculation behind the tubes with the lowest Nu, and c) the aforementioned horseshoe vortex at the stagnation of each tube row increasing its intensity in proportion with Re.

The local heat transfer coefficient h_{loc} is obtained from the energy balance at each CV of the interface between fluid and solid where the boundary conditions are coupled for both domains. Therefore, convective heat transfer from the fluid is equivalent to the conduction heat transfer to the solid ($\dot{q}_{cond} = \dot{q}_{conv}$), knowing that $\dot{q}_{cond} = -\lambda \frac{\partial T}{\partial n}$ and $\dot{q}_{conv} = h_{loc}(T_m - T_w)$ (T_m is the local bulk temperature and T_w is the wall temperature) it is possible to calculate h_{loc} and Nusselt number calculation is straightforward ($Nu = hD/\lambda$).

In Figs. 4.8, 4.9 and 4.10 when Reynolds number is equal to 300 and 550, higher heat transfer at the stagnation region of the second row of tubes than the one measured on the first row. This effect is due to the horseshoe vortex structures present at this point of the heat exchanger. Similar observations have been made in previous publications at fluid regimes of almost the same range as the present work [5, 29–31].

At the center midplane between two fins, the resulting dimensionless velocity and pressure profiles of the fluid flow are shown in Fig. 4.11. Noticeable acceleration of the flow is observed in the minimum cross sectional area between adjacent tubes while behind them recirculation can be seen from the velocity profiles. On the other hand, pressure loss is evident in the longitudinal direction of the heat exchanger and highest pressure values (and in consequence local pressure coefficient) is located at the stagnation point of the tubes, more evident at the first row and clearly visible at the second row for $Re = 300$ and 550.

As aforementioned the fluid domain consists on a larger geometry than the actual

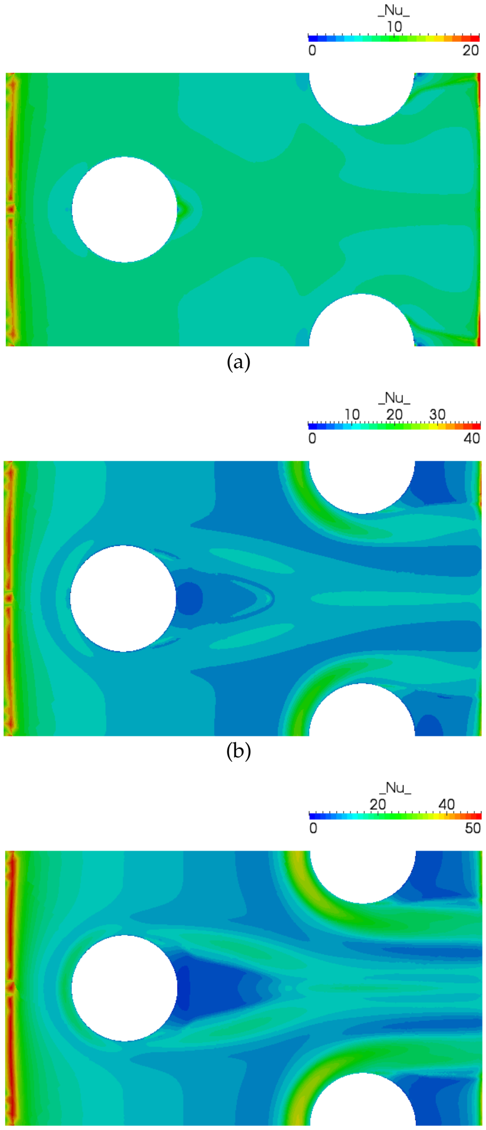

(a)

(b)

(c)

Figure 4.10: Local Nusselt number for a) $Re = 50$, b) $Re = 300$ and c) $Re = 550$ at fins surfaces.

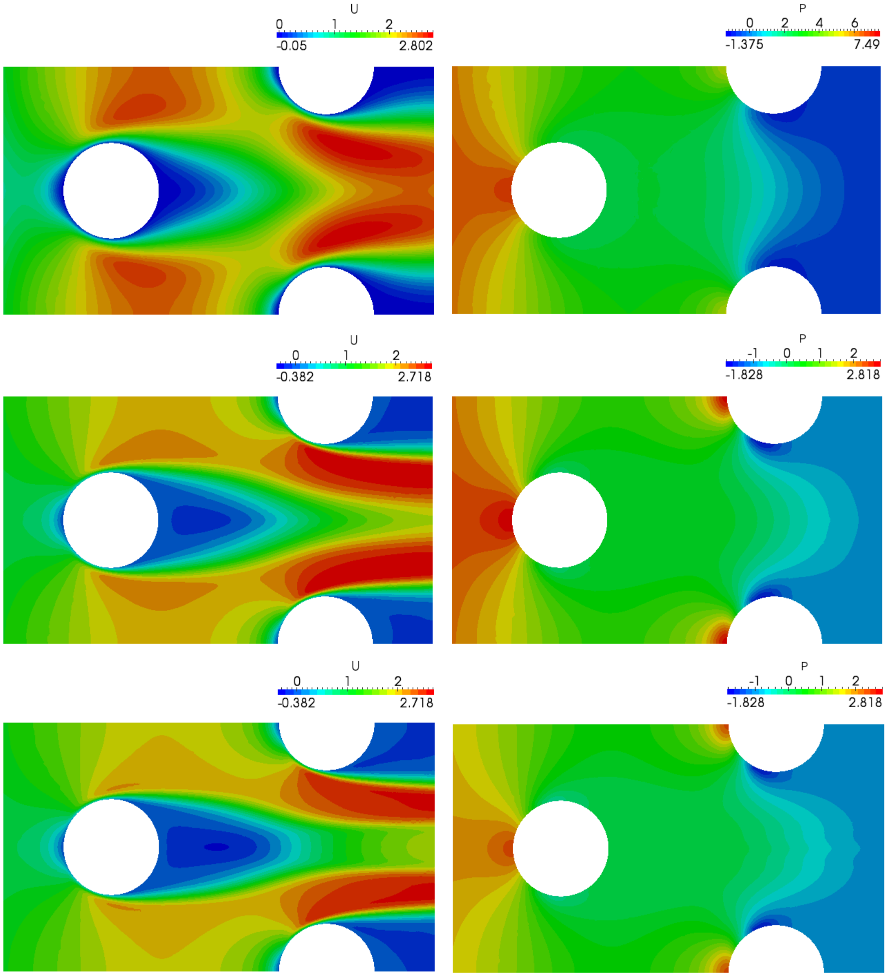

Figure 4.11: Local left: velocity and right: pressure profiles for top: $Re = 50$, middle: $Re = 300$ and bottom: $Re = 550$ at the midplane of the fluid domain.

longitudinal length of the heat exchanger to deal properly with the numerical issues explained above. Fig. 4.12 shows the temperature profile at the midplane ($z = P_F/2$) and at the inlet and outlet cross sections for the entire fluid computational domain.

For the conjugated heat transfer problem, the energy equation was solved at the solid domain of the fins and the corresponding dimensionless temperature profiles are illustrated in Fig. 4.13. In consequence with the heat transfer results previously discussed, the fin temperature distribution is less uniform and colder as the Reynolds number is increased, because of their corresponding higher cooling effect.

As aforementioned, one of the main strengths of such detailed analysis is the great amount of local and global information that can be obtained from each simulation. The velocity and temperature boundary layers formed by the solid fins at the entrance of the heat exchanger have different developments at each Reynolds number. Fig. 4.14 depicts this information at the plane located at the center of the domain in the spanwise direction (*y axis*), midplane between fins is also included on the figure. Both velocity and thermal boundary layers thickness are smaller when Re is increased, which is the typical behavior for a channel flow. On the other hand, the effect of the acceleration of the fluid caused by the presence of the tubes is significantly more perceptible at the lower Reynolds number.

Three dimensional iso-surfaces of temperature contours are plotted on Fig. 4.15 and colored by the magnitude of the velocity vector pattern. From this figure, it can be explained in a good manner the behavior of the flow and specially heat transfer between fluid and solids. The horseshoe structure observed on the local distribution of Nusselt number particularly for the two higher Reynolds numbers (Fig. 4.10) is the reflection of the 3D temperature distribution at the impingement region of the cylinders. It can be seen that the flow hits the rare of the tubes and gets redirected to the fins, this causes the increase on heat transfer at that point of the domain. Also, it can be deduced the thermal drag effect caused by the wake formed behind the tubes, more clearly noticed after the first row.

Finally, fluid-thermal observations are taken from Fig. 4.16 where a combination of velocity, temperature and heat transfer rate is illustrated for half of the computational domain. The fluid temperature profile is illustrated at the *x*-*z* plane positioned at the center of the tube to show the thermal boundary layer at the fins and the temperature distribution near the tubes. The wake behind the second row of tubes has diverse behavior at each Reynolds, causing important differences in the temperature distribution (e.g., much colder fluid for the highest Reynolds number). Fluid streamwise velocity profile is depicted at the *x*-*y* plane located at the centerline between fins to visualize the flow pattern distribution. The presence of the tubes affects the acceleration of the flow depending on the Reynolds number. For the slower case with $Re = 50$ the flow is more affected by this effect, visible even at the first row of tubes. The solid fin domain is included on the figures plotting their temperature

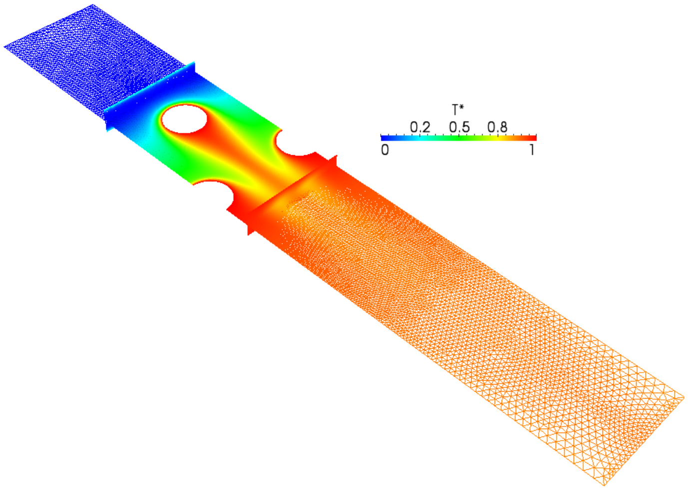

(a)

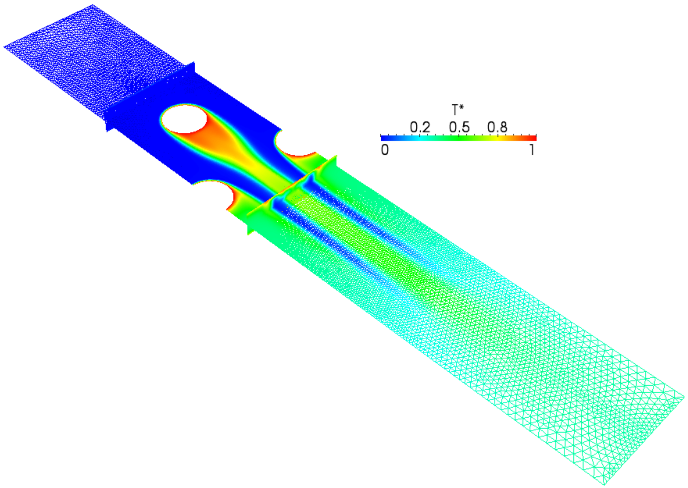

(b)

Figure 4.12: Dimensionless temperature profile for the extreme cases: a) $Re = 50$, and c) $Re = 550$ at the entire fluid domain.

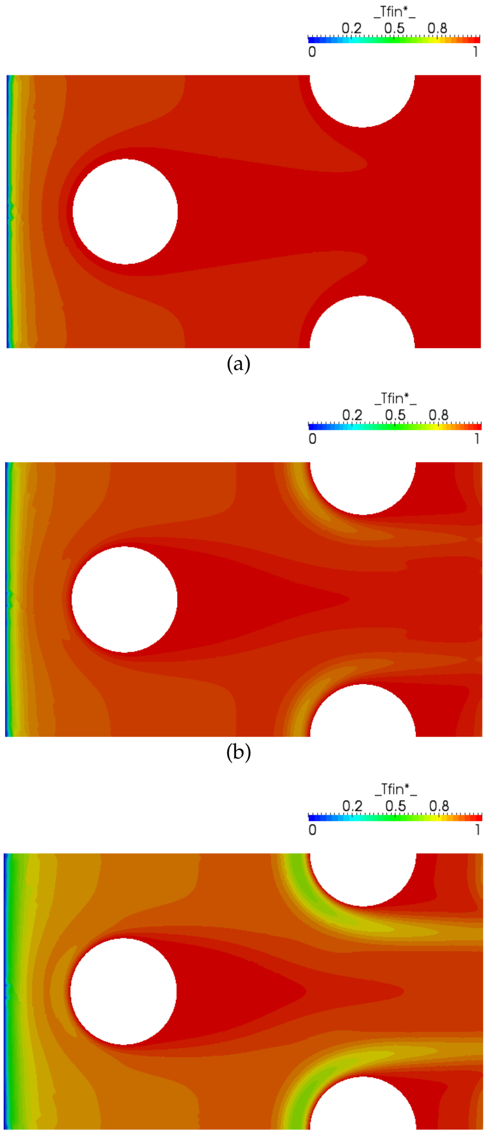

(a)

(b)

(c)

Figure 4.13: Dimensionless temperature profile for a) $Re = 50$, b) $Re = 300$ and c) $Re = 550$ at the solid fin domain.

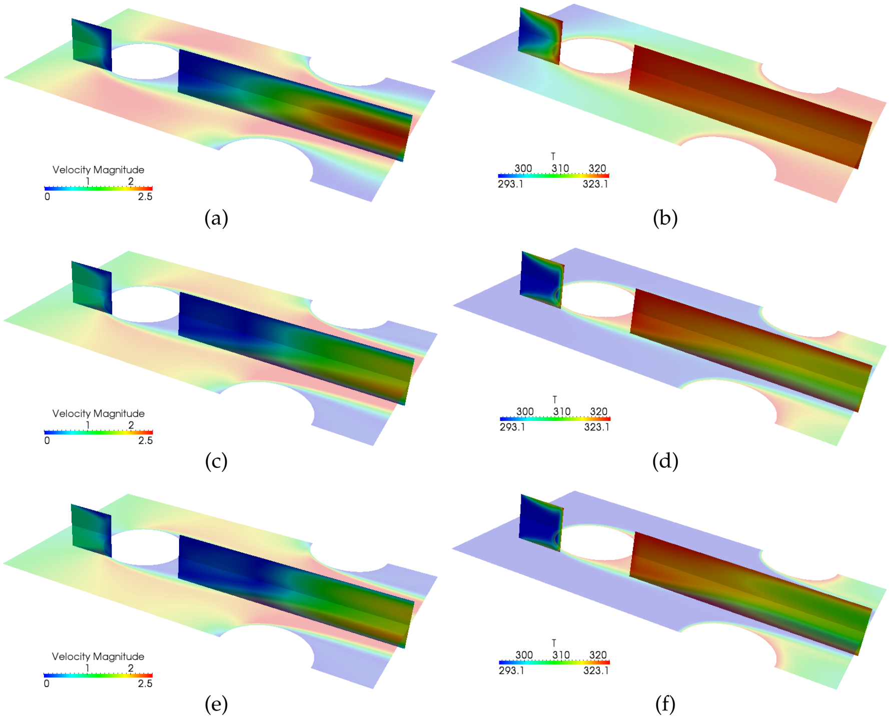

(a) (b) (c) (d) (e) (f)

Figure 4.14: Velocity (right) and temperature (left) boundary layer development for top: $Re = 50$, center: $Re = 300$ and bottom: $Re = 550$ at the spanwise midplane of the fluid domain.

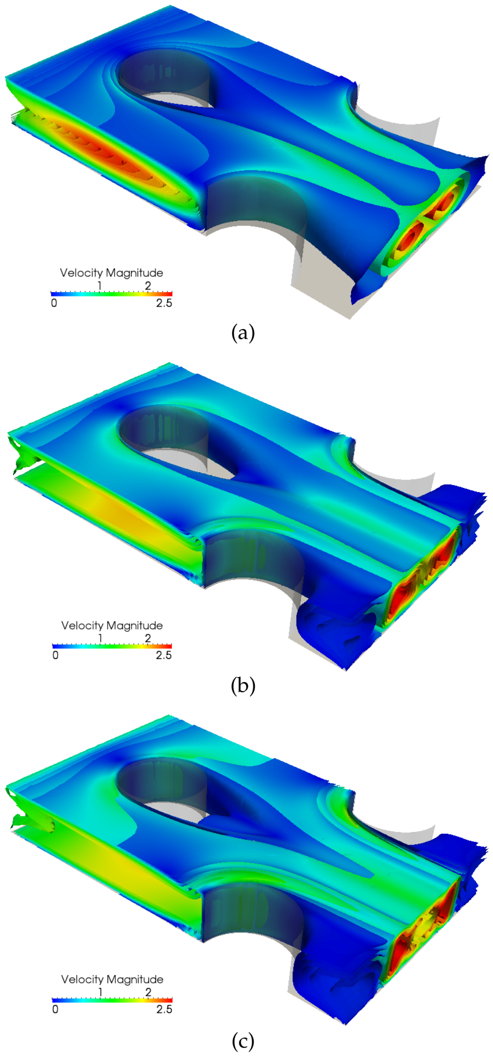

Figure 4.15: 3D temperature iso-surfaces colored with the velocity pattern for a) $Re = 50$, b) $Re = 300$ and c) $Re = 550$.

distribution which is less uniform as Reynolds number augments due to the three dimensionality of the related flow. Then, the dimensionless heat rate is quantified at the tube surfaces. The first important fact to comment is that regardless the flow regime, the useful surface for heat exchange by the tubes is the impingement region because the back of the tube is affected by the trapped flow behind them with almost no heat transfer at all. Nevertheless, the higher the Reynolds number, the highest the heat transfer rate caused by the tubes of the heat exchanger.

4.4 Analysis of 'no-frost' evaporators

Several different geometries are usually employed for 'no-frost' evaporators. In the present research, the characteristic geometry of the baseline case proposed by one industrial partner is composed of 10 rows by 2 columns of circular tubes positioned in staggered arrangement. Across the tube bundle, fins of two different sizes are placed alternating in between. While one fin covers the entire domain of 10 rows, the next fin covers only for the last 8 rows along the flow direction. This fin distribution is continued until the evaporator is fully covered aiming at avoiding frost formation at the entrance of the channels. The fin pitch is P_{F1} for the first two rows and $P_{F2} = P_{F1}/2$ for the last eight rows. However, the present characteristic fluid domain is formed only by one of these channels conformed between two large fins because the thermo hydraulic problem is expected to behave in the same way at every sub-duct if the tube temperature is assumed to be constant. A schematic view of the proposed baseline geometry is shown in Fig. 4.17. The diameter of the tubes is denoted as D and the transversal and longitudinal tube pitches are represented with S_1 and S_2, respectively.

Because one of the main objectives of the present paper is to study the influence of different transversal fin lengths ($L_1 = H$ on Fig. 4.17), this parameter and the corresponding transversal tube pitch (S_1) are modified for the three alternatives referred in Table 4.2. The other geometrical parameters are kept constant for all the cases, i.e., $D = 8.0mm$, $P_{F1} = 10.0mm$, $P_{F2} = 5.0mm$, the longitudinal fin length of the larger fin is $W_{long} = 190.5mm$, the longitudinal fin length of the shorter fin is $W_{short} = 151.5mm$, the longitudinal tube pitch is $S_2 = 18.75mm$, the fin thickness is $t_F = 0.15mm$.

The tube cylinders are considered to be at a constant wall temperature ($T_{cyl} = T_C$) while the temperature profile is calculated for all the sub-domains, the solid sub-domain (meaning the fins) and the fluid sub-domain for the region confined by the fins and tubes (meaning the air region). Reynolds number is based on the tube diameter and the inlet velocity ($Re = \frac{V_{in}D}{\nu}$). Prandtl number is defined as $Pr = \frac{\mu c_p}{\lambda}$. The entering working fluid flow is supposed to be at a uniform constant temperature ($T_{in} = T_H$). As mentioned earlier, the temperature distribution of the

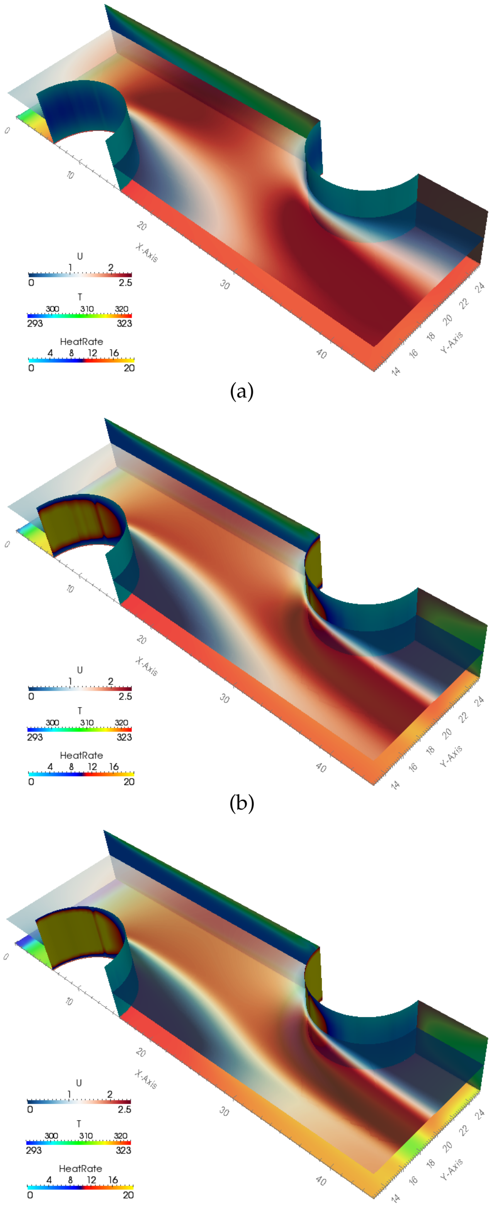

(a)

(b)

(c)

Figure 4.16: Quantification of velocity, temperature and heat transfer rate along the heat exchanger. a) $Re = 50$, b) $Re = 300$ and c) $Re = 550$.

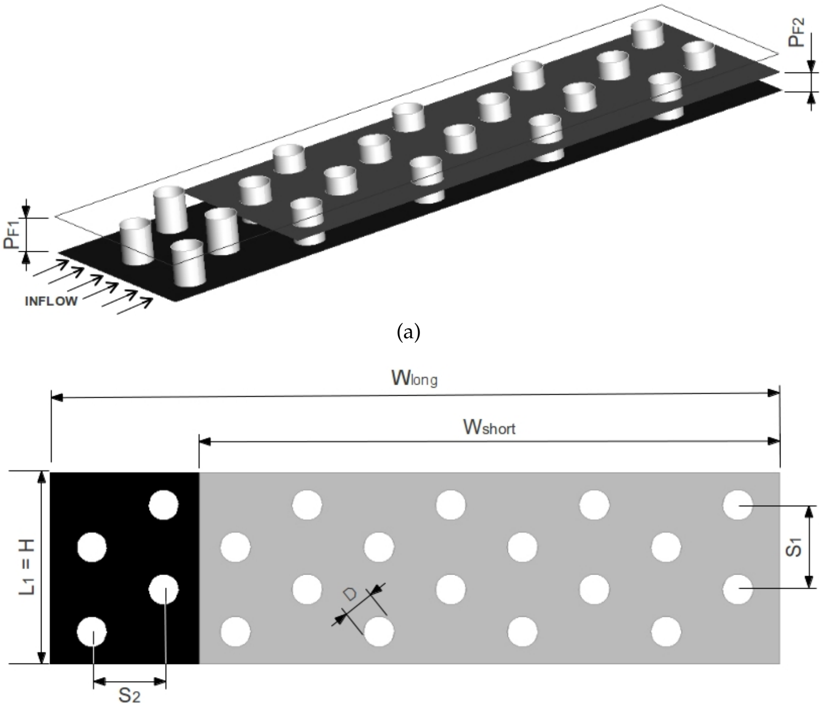

(a)

(b)

Figure 4.17: Schematic view of the baseline case used for the numerical simulations.

Table 4.2: Geometrical parameters of the studied computational domains.

Case	L_1 (mm)	S_1 (mm)
H40	40	17.64
H50	50	22.05
H60	60	26.46

Table 4.3: Inlet volumetric flow rates (measured in m^3/h) for the simulations and corresponding Reynolds number for each geometric case.

$\dot{V}$	H40	H50	H60
0.443	215.85	172.68	143.90
0.886	431.71	345.37	287.80
1.773	863.42	690.74	575.61

fins is simulated.

Regarding to the flow characteristics from previous fluid dynamic analysis of fan-system interaction, it is assumed that the volumetric flow rate is the same for the three geometries, while three levels of flow are considered in this problem. In table 4.3 the different levels of inlet volumetric flow rates are presented. The equivalent Reynolds numbers corresponding to each case are specified also on the table.

4.4.1 Mesh Assessment

Body fitted strategy is used to generate the three dimensional meshes to solve the present problem. In consequence, all meshes are built with prismatic elements. A proper control of grid refinement is carefully applied around the solid walls (fins and cylinders). Three levels of mesh density are used for the baseline case H50 (see Fig. 4.18) in order to determine an appropriate sizing of the CV in the meshes used for all the other analyzed geometries.

First mesh density, consists of 1.3×10^6 CV in the fluid sub-domain and 5.6×10^4 CV in the solid sub-domain (3.1×10^4 at the long fin and 2.5×10^4 at the short fin). This mesh is referred as *Small mesh*. The second level of grid refinement (*Medium mesh*) has 2.8×10^6 CV in the fluid sub-domain and a total of 1.11×10^5 CV in the solid sub-domain, divided in 6.2×10^4 and 4.9×10^4 CV for the long and short fins respectively. Finally, the *Large mesh* consists on 4.2×10^6 CV for the fluid and 1.7×10^5 at the solids (with 9.5×10^4 and 7.5×10^4 CV for long and short fins respectively). Local results for grid independence analysis are plotted over lines A, and B which are schematically represented in Fig. 4.19.

Fig. 4.20 illustrate the local values of velocity, temperature and pressure coefficient (c_p) profiles for case H50 at the highest volumetric flow rate which is the most demanding case in terms of computational power due to the thinner boundary layers. Pressure coefficient is defined as $c_p = [P_\theta - P_0]/(\rho V_{in}^2/2)$, where P_0 is the pressure at the stagnation point in the cylinder, and P_θ is the pressure of the flow at the θ circumferential angle around the pin (with θ ranging from 0 to 180 deg.).

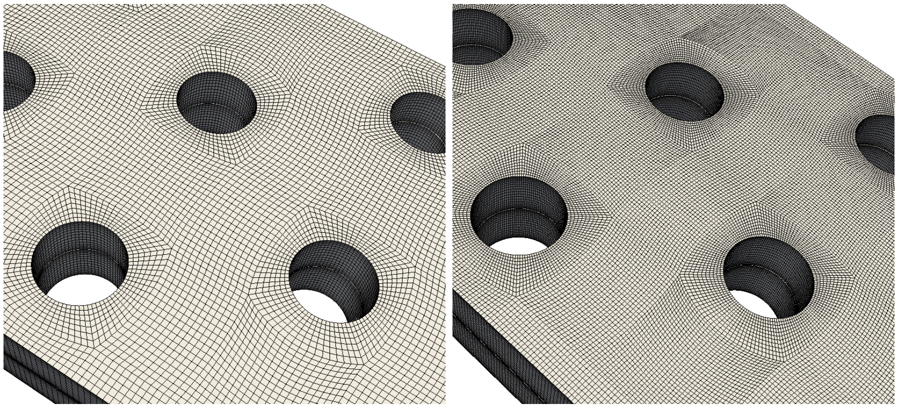

Figure 4.18: Mesh resolution of a)coarse (*small*) and b)fine (*large*) meshes.

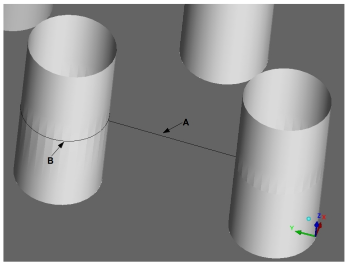

Figure 4.19: Schematic view of the lines where results are ploted.

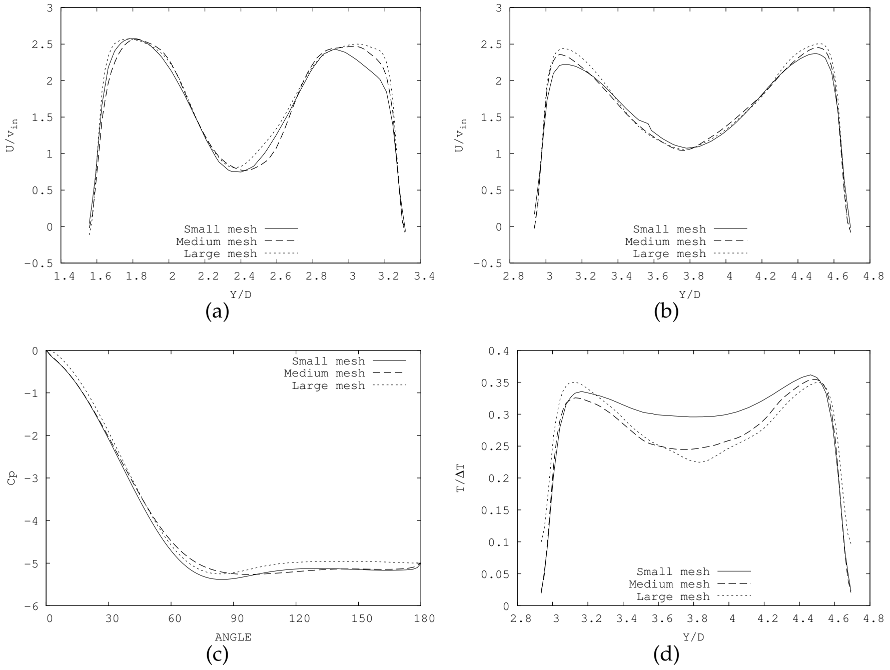

(a)

(b)

(c)

(d)

Figure 4.20: $\dot{V}_3 = 1.773 m^3/h$, top: Horizontal velocity at line A a) third row, b) eighth row. Bottom: c) Pressure coefficient at line B (first row), d) Temperature at line A (eighth row).

Table 4.4: Maximum y^+ values for the cells close to solid walls for the baseline case H50 using three levels of grid refinement.

Mesh	Long Fin	Short Fin	Cylinders
Small	2.78	6.60	5.74
Medium	1.90	5.08	4.29
Large	1.72	4.75	4.03

In general, the results displayed show short differences between *Medium* and *Large* meshes. Despite the sizes of the present meshes are considered to be coarse for what is expected on LES methods, the grid independence is ensured enough for the aim of this Chapter. *Medium* mesh parameters were chosen as the most adequate ones for the mesh design on every other geometries because the differences in the local performance between *Medium* and *Large* meshes were not as relevant as the difference in the computational costs (which is significantly bigger for the *Large* mesh).

The wall y^+ is a non dimensional distance, only technically applicable to parts of the flow that are close to the wall.

$$y^+ = (u_\tau y)/\nu \tag{4.25}$$

The objective of using this parameter is to ensure that the used mesh is appropriately solving the boundary layer of the flow. The maximum values of y^+ for the present research are pointed out on Table 4.4 for the baseline case H50 when the volumetric flow rate is the highest ($\dot{V} = 1.773 m^3/h$), which shows the most turbulent behavior.

On the past, the authors have performed numerical simulations using LES techniques for similar geometries with higher characteristic velocities (Reynolds number) obtaining reasonable good performance of the numerical method with similar maximum y^+ values [14]. Based on previous experience, these meshes can be assumed to have enough quality to use the same closure.

4.4.2 Results and discussion

The simulations are advanced in time until stationary flow conditions are achieved if the flow is laminar, and statistical stationary flow conditions if the flow is considered to be turbulent or in the transition regime. In the last case, 1000 dimensionless time units (TU^*) are simulated ($TU^* = tV_{in}/D$), and only the last 700 are taken into account for the time averaged results.

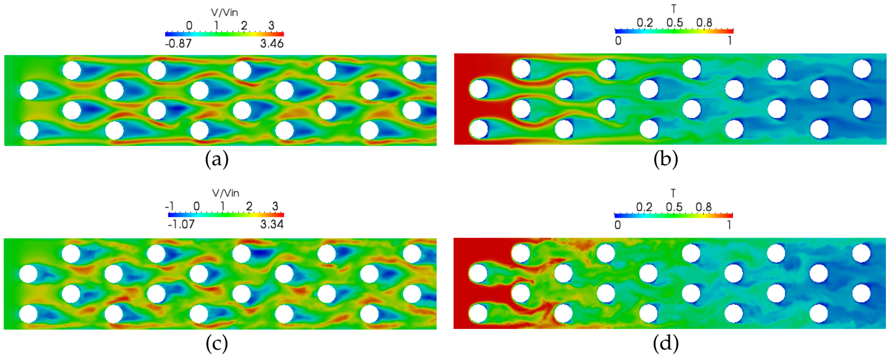

(a) (b)

(c) (d)

Figure 4.21: Instantaneous view of left: dimensionless velocity and right: temperature profiles for top: $\dot{V}_2 = 0.886 m^3/h$ and bottom: $\dot{V}_3 = 1.773 m^3/h$.

Instantaneous flow. Fluid domain

After a first preliminary simulation for all the cases cases studied in the present paper ($H = 40{,}50{,}60\ mm$ for $\dot{V} = 0.443$. And specifically for the case H40 different volumetric flow rates are analyzed and compared $\dot{V} = 0.443{,}0.886{,}1.773\ m^3/h$). Careful analysis of the flow features has been made by the authors and for the highest volumetric flow rate, presence of turbulence is found. For this cases, it is worth to include LES techniques into the governing equations in order to adequately solve all the scales of turbulence by modeling the smaller ones with the WALE model (explained in Sec.4.2.2).

In the case H40, WALE model is used for the two highest volumetric flow rates $\dot{V}_2 = 0.886\ m^3/h$ and $\dot{V}_3 = 1.773\ m^3/h$. $\dot{V}_2$ regime renders some regions under laminar regime and some other zones under turbulent or transition conditions, therefore LES techniques are included to model the turbulence smaller scales of the flow. Fig. **??** shows instantaneous snapshots of the dimensionless velocity and temperature profile for the two higher $\dot{V}$. As can be seen from the figure, $\dot{V}_2$ is laminar at the entrance of the channel and it remains this way until approximately the fifth row where transition to turbulence occurs. For this reason this case is included for the proposed turbulent treatment.

Attempting to quantify the turbulence intensity of the transition or turbulent cases, the Euclidian norm of the Reynolds stress tensor is calculated and it is considered to be a good approximation of the turbulence level present inside the simulated domain. Fig. 4.22 illustrates the turbulence intensity at the midplane located at $z = P_{F2}/2$ for the cases with turbulent flow regime.

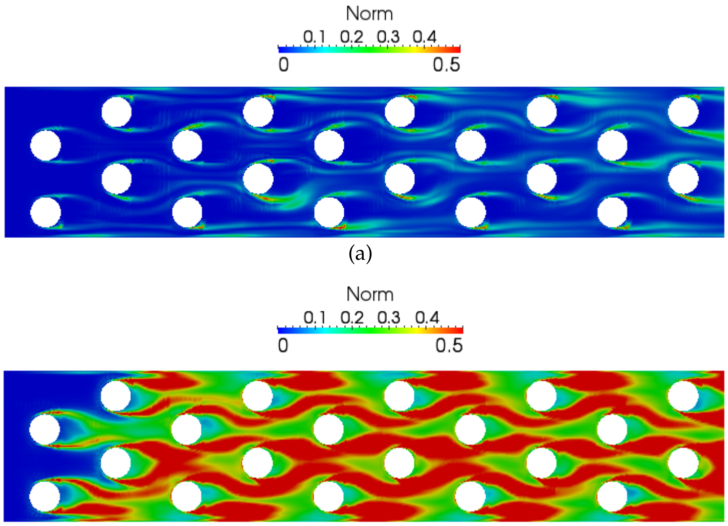

(a)

(b)

Figure 4.22: Instantaneous view of the turbulence intensity for the case H40 a) $\dot{V}_1 = 0.886 m^3/h$, b) $\dot{V}_1 = 1.773 m^3/h$.

The most turbulent regions are, as expected, those coinciding with the zones where the flow is separating from the tube wake. Thus, the staggered array of the tubes placement is important in order to increase the mixing of the flow over the heat exchanger.

Average flow. Fluid Domain

Fig. 4.23 illustrates the stationary dimensionless longitudinal velocity ($\frac{V}{V_{in}}$) profiles at the midplane located at $z = P_{F2}/2$ for the minimum volumetric flow rate ($\dot{V}_1 = 0.443\ m^3/h$) with the three geometrical configurations. Also the dimensionless temperature ($\frac{T-T_C}{T_H-T_C}$) profiles are displayed in Fig. 4.24 for the same flow regime. The flow is clearly accelerated at the minimum flow area between adjacent tubes, and the staggered arrangement force the flow to have oscillations aiming at the increase of heat transfer capacity.

Increasing the transversal fin length L_1 while maintaining the volumetric flux constant, implies an inversely proportional relation between H and inlet velocity. The dimensionless ratio of velocity profile at the midplane normalized with the corresponding inlet velocity keeps the same tendency of decreasing if H is enlarged.

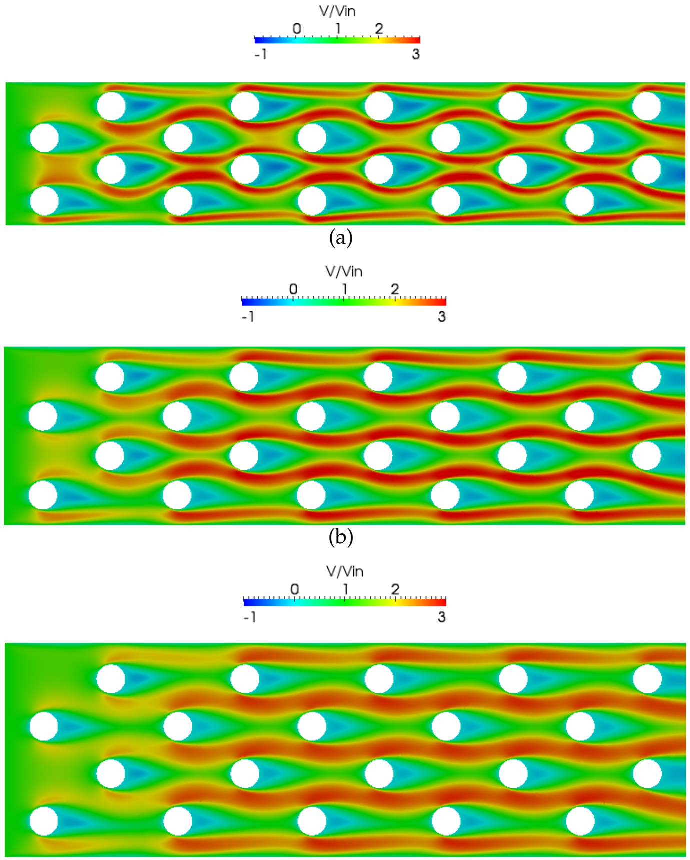

(a)

(b)

(c)

Figure 4.23: Dimensionless airflow velocity contour at $z = P_{F2}/2$ for different transversal fin lengths. Volumetric flow rate is $0.443 m^3/h$. a)H40; b)H50 and c)H60.

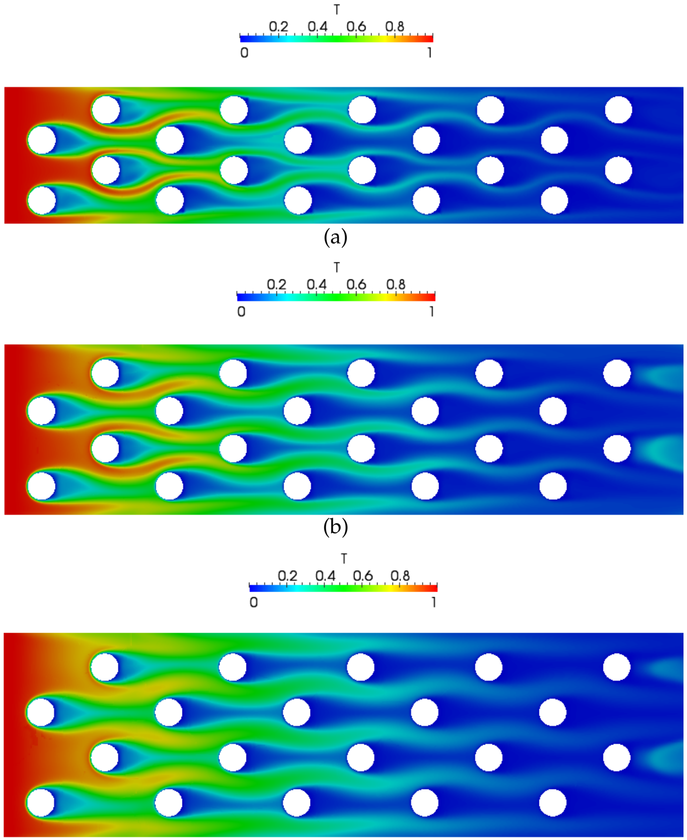

(a)

(b)

(c)

Figure 4.24: Dimensionless airflow temperature contour at $z = P_{F2}/2$ for different transversal fin lengths. Volumetric flow rate is $0.443 m^3/h$. a)H40; b)H50 and c)H60.

If the geometry is kept constant and the parameter under study is the volumetric flow rate, the results are represented in Fig. 4.25 for the dimensionless velocity profile and Fig. 4.26 for the dimensionless temperature distribution, both at the midplane between large and short fins located in $z = P_{F2}/2$. The effect of the staggered arrangement of the tubes is more relevant at the lower $\dot{V}$ because the flow is significantly more accelerated than for the other inlet velocities. This is because when the flow has an already fast velocity at the inlet, the acceleration is not as perceptible as for the lower cases. Hence, the fluid is more cooled by the tubes at this low flow rate. In the end, the heat transfer between fluid and solid is higher when the temperature difference between domains is larger. In this sense, higher heat transfer can be deduced at higher volumetric flow rates (as will be quantified later).

Solid domain

Fig. 4.27 represent the dimensionless temperature profile of the larger fin for the three transversal fin length (L_1) at the lower volumetric flow rate ($\dot{V}_1 = 0.443\, m^3/h$). This figure presents very similar temperature distribution between geometries. The superior left corner (flow is from left to right) is more affected by the hotter fluid in the entrance region because the influence from the closest cold tube is not enough to cool the surface fin. In the rest of the fin downstream the temperature distribution is almost uniform because of the high thermal conductivity of the fin and in general the parameter Fi.

The influence of increasing the volumetric flow rate on the temperature distribution of the solid fin is depicted in Fig. 4.28. On the contrary from variation of transversal fin length, when the solid temperature distribution is very similar from one case to the other. The effect of variation of the inlet volumetric flow rate on the same geometry (H40) is quite important. The temperature distribution of the solid fin is far from constant at the higher $\dot{V}$ when for the lower flow regime, after the fourth row the temperature profile has minor changes.

Conjugated problem (fluid and solid subdomains)

The dimensionless heat transfer defined by Eq. 4.24 is illustrated in Fig. 4.29, the aforementioned horseshoe structures indicating the three-dimensionality of the complex problem are clearly visible at the fin and cylinder surfaces. A significant part of the total amount of energy exchanged is due to the first four rows of the device, this is an observation that many other authors have published ([5–7, 11]). Actually the third row would seem to have less relevance on the total amount of heat exchanged if it was not for the extra fin placed in the center. Because of this change in the geometry (double fin spacing), the third and fourth rows of tubes increase the energy exchanged with the fluid.

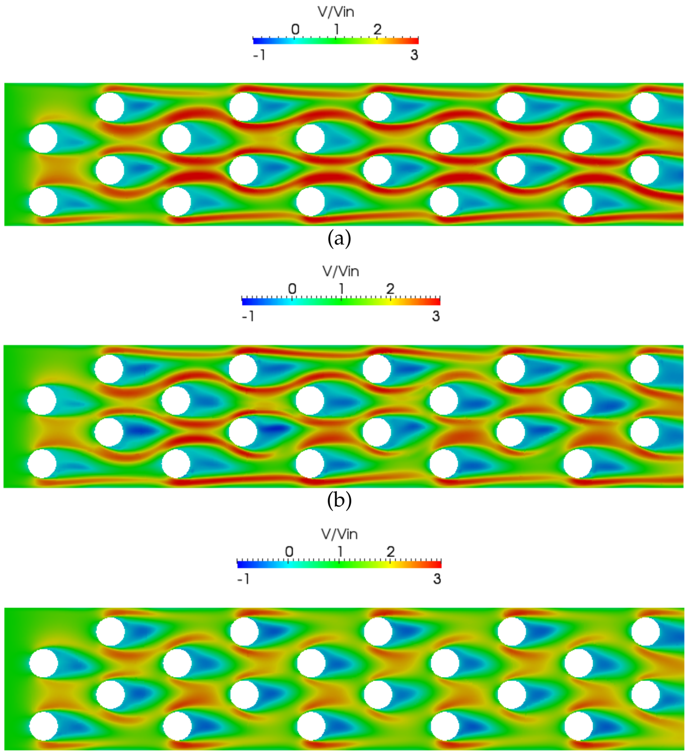

(a)

(b)

(c)

Figure 4.25: Dimensionless airflow velocity contour at $z = P_{F2}/2$ for the geometric case H40 a) $\dot{V} = 0.443 m^3/h$, b) $\dot{V} = 0.886 m^3/h$ and c) $\dot{V} = 1.773 m^3/h$.

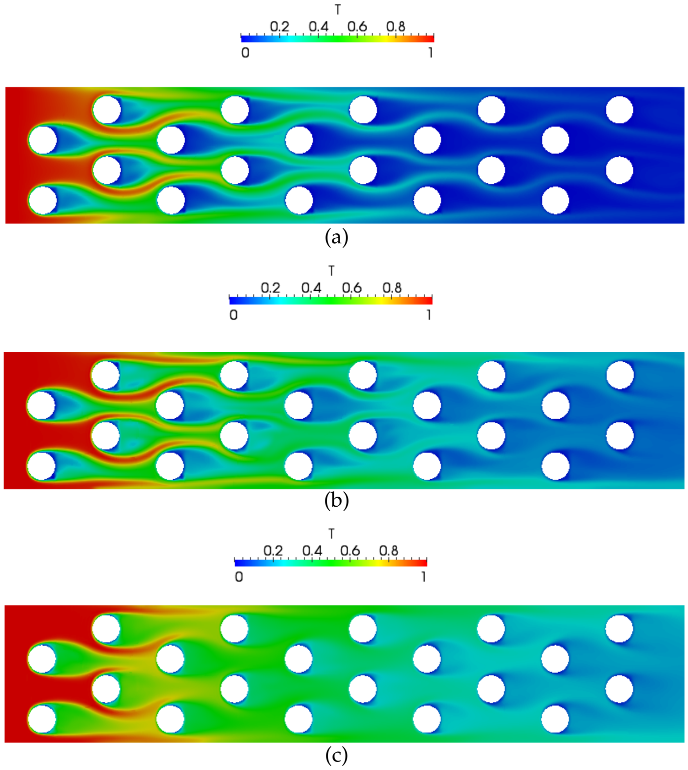

Figure 4.26: Dimensionless airflow temperature contour at $z = P_{F2}/2$ for the geometric case H40 at different volumetric flow rates a) $\dot{V} = 0.443 m^3/h$, b) $\dot{V} = 0.886 m^3/h$ and c) $\dot{V} = 1.773 m^3/h$.

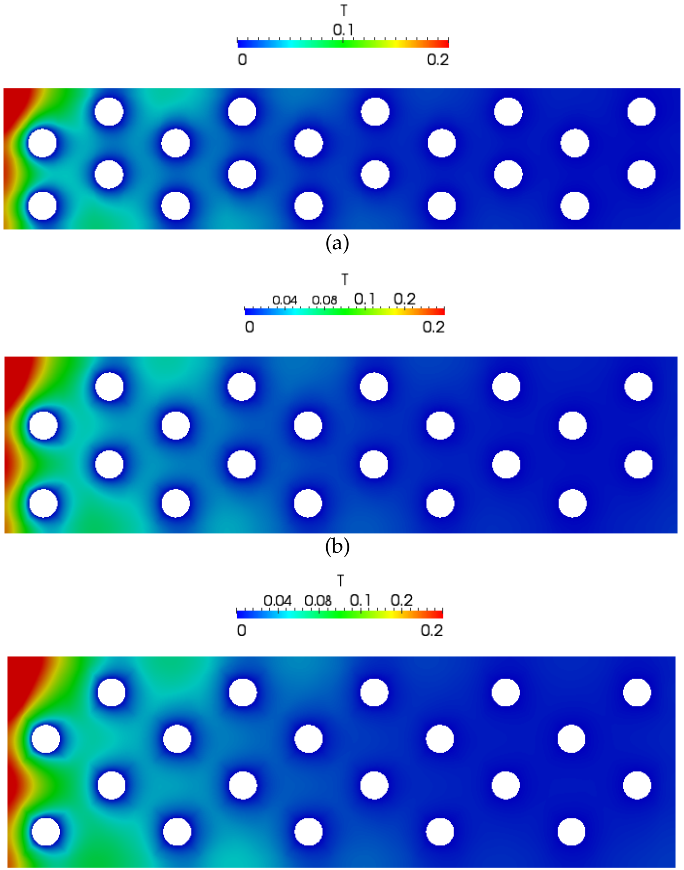

(a)

(b)

(c)

Figure 4.27: Distribution of the dimensionless temperature profile of the larger solid fin for different transversal fin lengths and different transversal tube pitches. Volumetric flux is $0.443\ m^3/h$. a) H40, b) H50, c) H60.

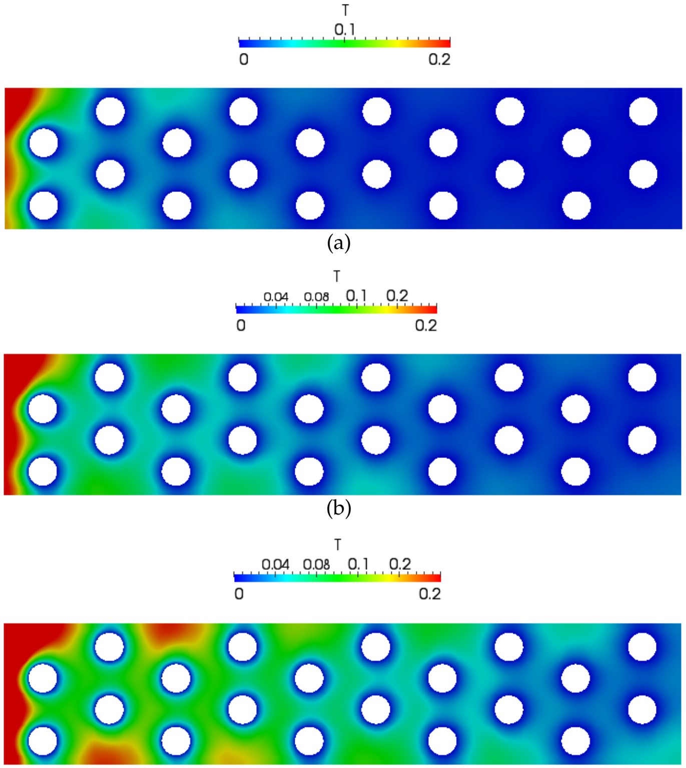

(a)

(b)

(c)

Figure 4.28: Distribution of the dimensionless temperature profile of the larger solid fin for the geometric case of H40 at different volumetric flow rates a) $\dot{V} = 0.443 m^3/h$, b) $\dot{V} = 0.886 m^3/h$ and c) $\dot{V} = 1.773 m^3/h$.

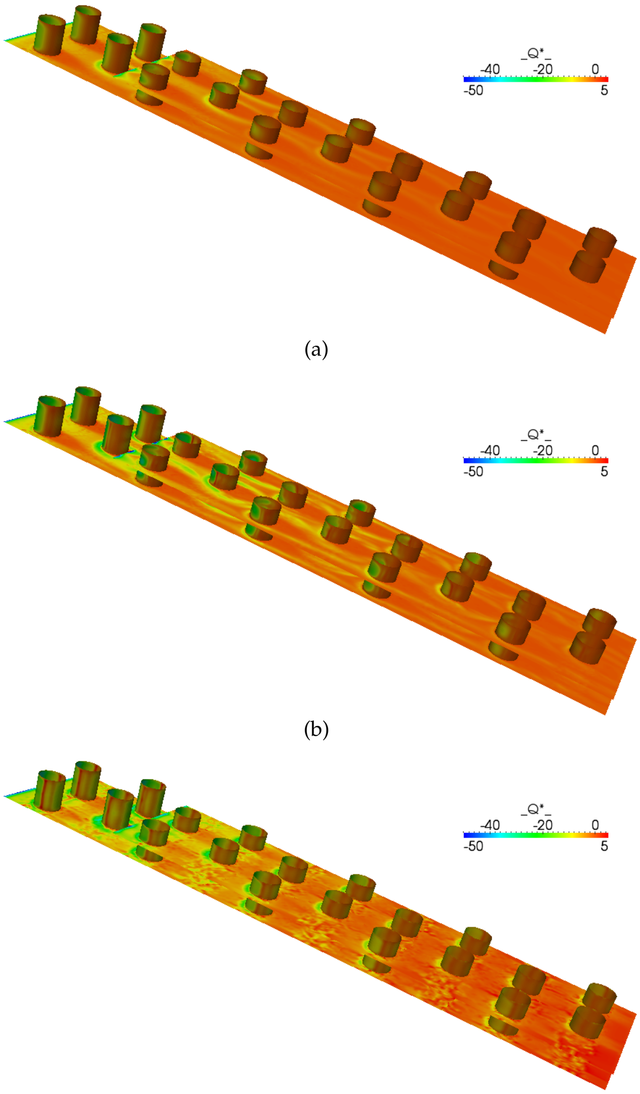

(a)

(b)

(c)

Figure 4.29: Dimensionless heat transfer rate for the case H40 a) $\dot{V} = 0.443 m^3/h$, b) $\dot{V} = 0.886 m^3/h$ and c) $\dot{V} = 1.773 m^3/h$.

As can be see from Fig. 4.29, heat transfer rate is not uniform along the geometry. It is expected that the first rows are responsible for most of the heat exchanged due to the development effect and the direct impingement to the tubes. Moreover, heat transfer from the air is quantified row by row and it is divided by a reference heat (Q_{ref}). Such Q_{ref} is reference heat exchanged defined by Eq. **??**.

$$Q_{ref} = \frac{\lambda_{fluid}(T_H - T_C)A_0}{D_0} \tag{4.26}$$

where A_0 is the area related to H40 case, and D_0 is the diameter of the tube.

Therefore Fig. 4.30 depicts the distribution of the relative heat transfer rate due to the fins and to the tubes at every row of the domain.

As mentioned earlier, the first 4 to 5 rows of tubes are generating most of the heat exchange of the entire domain (see Fig. 4.30b) and the expected decreasing value downstream is observed. On the other hand, Fig. 4.30a, shows noticeable increase of heat transfer rate at the third row due to the addition of a shorter fin in the normal direction after the second row of tubes. The increase of effective heat transfer fin area and the forced generation of a new boundary layer over the shorter fin significantly increases the heat exchanged due to the fins.

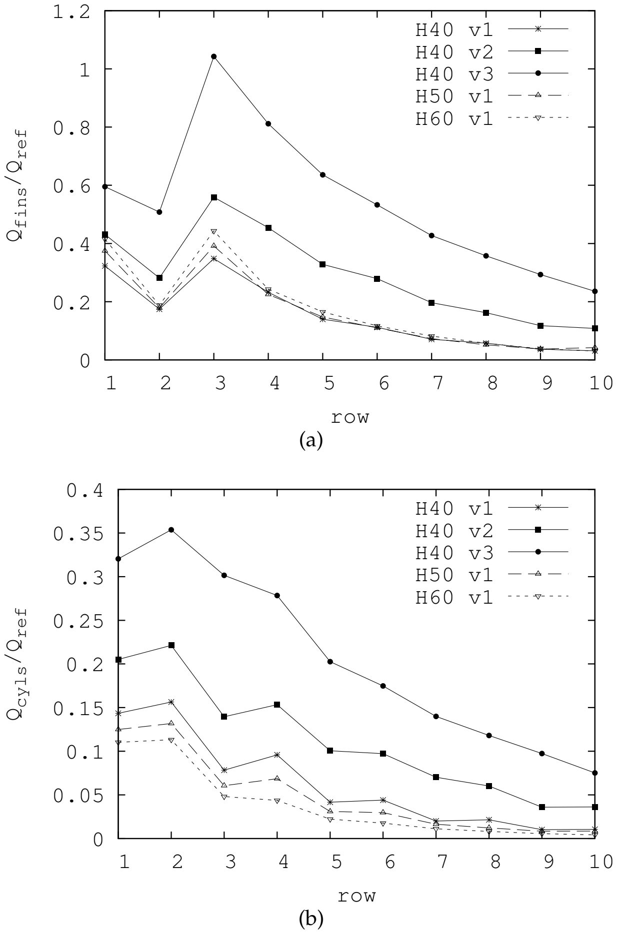

Figure 4.30: Dimensionless heat transfer rate quantified row by row for the five different cases studied. a) at the fins, b) at the tubes.

4.5 Concluding remarks

The present Chapter displayed the results of CFD study on the heat transfer and hydrodynamic characteristics of the flow over plate fin and tube heat exchangers. The modeling approach was verified against available experimental data ([1]). Several tests were carried out in order to evaluate the proper functioning of the methodology for conjugated heat transfer problems. Referring to the validation problem, sufficiently good agreement against experiments was accomplished (for the objective of simulating industrial applications) and further detailed fluid and solid features were discussed.

Some relevant conclusions can be made from the validation case study, namely:

- Some thermophysical properties of the working fluid can force the simulation to higher costs and time consumption. Therefore, it is recommended to preserve the characteristic dimensionless parameters of the problem of interest and recalculate the physical properties for convenience.
- Simulations are intended to behave as realistic as possible, thus conjugated heat transfer should be solved at the fluid-solid interfaces where heat is exchanged as far as the resources permit. Fin surface temperature profiles were illustrated and it was clear that the temperature is not constant specially for higher Reynolds numbers.
- Nevertheless given the high conductance of the fin material the same problem was also studied for constant temperature as boundary condition of the fin surfaces.
- As has been reported on the literature, the first row of tubes has higher Nusselt number than the second row. Which is believed to be due to the influence of the flow development.

For the industrial problem that motivated this investigation, the visualized results of the flow revealed interesting aspects of the local fluid flow features over this kind of heat exchangers. As far as the authors are aware, this is the first research including results to quantify the turbulence intensity. It was clear that the turbulence was higher for smaller transversal fin length. This output has academic interest in order to quantify turbulence and find the location of the higher values, however in practice there is another interest which relates turbulence with noise and for domestic refrigeration it is an aspect to keep in mind.

Detailed analysis and local information of the intricated physics of the flow features was obtained by the present work. The methodology in conjunction with the mathematical models were able to identify the most critical or important regions of the plate fin and tube heat exchanger. The recirculation regions behind the tubes, the vortex wake generated by them and the consequent horseshoe structures created by the heat transfer between fluid and solid were presented and exhaustively studied. Furthermore, it was found that the device had different flow regimes along itself and LES methodology was applied in order to model the small scales of turbulence on the regions were it was required.

This level of detail on the analysis of flow features can only be achieved by top order numerical simulations like the ones here presented. Experimental methods and simple numerical models can answer some direct questions (total heat transfer, pressure drop, device performance). But in order to have a full understanding of the problem and its complexity, numerical simulations allow the user to venture in the physics of the problem. The implemented tools needed for the simulations and the post processing of the obtained results open the gate for further simulations according to the industrial requirements. The local information and conclusions that cannot be deduced from experimental analysis or even harder to explain with more simple modeling tools will be available with the analysis strategy proposed in the present work.

With the information obtained by using the implemented tools, new numerical correlations can be obtained in order to broaden the range of design with different geometries. Generating local correlations for heat transfer coefficients, pressure drop, with many possible modifications to the existing designs.

References

[1] Y. Seshimo and M. Fujii. An experimental study on the performance of plate fin and tube heat exchangers at low Reynolds numbers. *ASME/JSME Thermal Engineering Proceedings*, 4:449–454, 1991.

[2] C. Wang and K. Chi. Heat transfer and friction characteristics of plain fin-and-tube heat exchangers, part I: new experimental data. *International Journal of Heat and Mass Transfer*, 43:2681–2691, 2000.

[3] C. Wang, K. Chi, and C. Chang. Heat transfer and friction characteristics of plain fin-and-tube heat exchangers, part II: Correlation. *International Journal of Heat and Mass Transfer*, 43:2693–2700, 2000.

[4] C. Wang, R. Webb, and K. Chi. Data reduction for air-side performance of fin-and-tube heat exchangers. *Experimental Thermal and Fluid Science*, 21:218–226, 2000.

[5] J. Jang, M. Wu, and W. Chang. Numerical and experimental studies of three-dimensional plate-fin and tube heat exchangers. *International Journal of Heat and Mass Transfer*, 39(14):3057–3066, 1996.

[6] Y. L. He, W. Q. Tao, F. Q. Song, and W. Zhang. Three-dimensional numerical study of heat transfer characteristics of plain fin and tube heat exchangers from view point of field synergy principle. *International Journal of Heat and Fluid Flow*, 26:459–473, 2005.

[7] J. Y. Jang, J. T. Lai, and L. C. Liu. The thermal-hydraulic characteristics of staggered circular finned-tube heat exchangers under dry and dehumidifying conditions. *International Journal of Heat and Mass Transfer*, 41:3321–3337, 1998.

[8] G. Comini, C. Nonino, and S. Savino. Modeling of conjugate conduction and heat and mass convection in tube-fin exchangers. *International Journal of Numerical Methods for Heat & Fluid Flow*, 18(7/8):954–968, 2008.

[9] M. Mon and U. Gross. Numerical study of fin-spacing effects in annular-finned tube heat exchangers. *International Journal of Heat and Mass Transfer*, 47:1953–1964, 2004.

[10] M. R. Shaeri and M. Yaghoubi. Numerical analysis of turbulent convection heat transfer from an array of perforated fins. *International Journal of Heat and Fluid Flow*, 30:218–228, 2009.

[11] J. Barbosa, C. Hermes, and Melo C. CFD Analysis of tube-fin 'no-frost' evaporators. *J. of the Braz. Soc. of Mech. Sci. & Eng.*, 32(4):445–453, 2010.

[12] W. M. Kays and A. L. London. *Compact Heat Exchangers*. McGraw-Hill, 1984.

[13] M. Perćić, K. Lenić, and A. Trp. A three-dimensional numerical analysis of complete crossflow heat exchangers with conjugate heat transfer. *Engineering Review*, 33(1):23–40, 2013.

[14] L. Paniagua, O. Lehmkuhl, C. Oliet, and C. D. Pérez-Segarra. Large Eddy Simulations (LES) on the Flow and Heat Transfer in a Wall-Bounded Pin Matrix. *Numerical Heat Transfer, Part B: Fundamentals: An International Journal of Computation and Methodology*, 65(2):103–128, 2014.

[15] S. Benhamadouche and D. Laurence. LES, coarse LES, and transient RANS comparisons on the flow across a tube bundle. *Int. J. Heat Fluid Flow*, 24:470–479, 2003.

[16] G. Delibra, K. Hanjalić, D. Borello, and F. Rispoli. Vortex structures and heat transfer in a wall-bounded pin matrix: LES with a RANS wall-treatment. *Int. J. Heat Fluid Flow*, 31:740–753, 2010.

[17] M. Labois and D. Lakehal. Very-Large Eddy Simulation (V-LES) of the flow across a tube bundle. *Nuclear Engineering and Design*, 241:2075–2085, 2011.

[18] O. Lehmkuhl, C.D. Pérez-Segarra, R. Borrell, M. Soria, and A. Oliva. TERMOFLUIDS: A new parallel unstructured CFD code for the simulation of turbulent industrial problems on low cost PC cluster. *In Proceedings of the Parallel CFD 2007 Conference*, pages 1–8, 2007.

[19] M. Fiebig, A. Grosse-Gorgemann, Y. Chen, and N. K. Mitra. Conjugate heat transfer of a finned tube. Part A: Heat transfer behavior and occurrence of heat transfer reversal. *Numerical Heat Transfer, Part A*, 28:133–146, 1995.

[20] R. W. C. P. Verstappen and A. E. P. Veldman. Symmetry-preserving discretization of turbulent flow. *Journal of Computational Physics*, 187:343–368, 2003.

[21] F. X. Trias and O. Lehmkuhl. A self-adaptive strategy for the time integration of Navier-Stokes equations. *Numerical Heat Transfer*, 60(2):116–134, 2011.

[22] C. M. Rhie and W. L. Chow. Numerical study of the turbulent-flow past an airfoil with trailing edge separation. *AIAA Journal*, 21:1525–1532, 1983.

[23] Y. Morinishi, T. S. Lund, O. V. Vasilyev, and P. Moin. Fully conservative higher order finite difference schemes for incompressible flow. *Journal of Computational Physics*, 143(1):90–124, 1998.

[24] F. N. Felten and T. S. Lund. Kinetic energy conservation issues associated with the collocated mesh scheme for incompressible flow. *Journal of Computational Physics*, 215(2):465–484, 2006.

[25] O. Lehmkuhl, R. Borrell, I. Rodríguez, C.D. Pérez-Segarra, and A. Oliva. Assessment of the symmetry-preserving regularization model on complex flows using unstructured grids. *Computers & Fluids*, 60:108–116, 2012.

[26] I. Rodríguez, O. Lehmkuhl, R. Borrell, and A. Oliva. Flow dynamics in the turbulent wake of a sphere at sub-critical Reynolds numbers. *Computers & Fluids*, 80:233–243, 2013.

[27] I. Rodríguez, R. Borrell, O. Lehmkuhl, C.D. Pérez-Segarra, and A. Oliva. Direct numerical simulation of the flow over a sphere at $Re = 3700$. *Journal of Fluid Mechanics*, 679:263–287, 2011.

[28] F. Nicoud and F. Ducros. Subgrid-scale stress modelling based on the square of the velocity gradient tensor. *Flow, Turbulence and Combustion*, 62:183–200, 1999.

[29] F. E. M. Saboya and E. M. Sparrow. Local and average heat transfer coefficients for one-row plate fin and tube heat exchanger configuration. *ASME Journal of Heat Transfer*, 96:265–272, 1974.

[30] F. E. M. Saboya and E. M. Sparrow. Transfer characteristics of two-row plate fin and tube heat exchanger configuration. *Int. Journal of Heat and Mass Transfer*, 19:41–49, 1976.

[31] F. E. M. Saboya and E. M. Sparrow. Experiments on a three-row fin and tube heat exchanger. *ASME Journal of Heat Transfer*, 98:26–34, 1976.

Chapter 5

Conclusions and further work

A general approach for the high-end numerical simulation of heat transfer and turbulent flow features in heat exchanger devices used on the refrigeration industry has been presented. Large-eddy simulation techniques were used to predict the turbulent flow and conjugated heat transfer characteristics present on compact heat exchangers for different applications like pin fin matrix for gas turbine blade cooling (Chapter 3) and 'no-frost' fin and tube domestic evaporators (Chapter 4).

This thesis has proposed a methodology for the CFD simulation procedure when treating with complex flows that are usually found in industrial challenges for rating, design or optimization purposes. The success of a high level numerical simulation depends on the adequate discretization of the geometrical domain (mesh generation), proper definition of the boundary and initial conditions, good selection and implementation of the general formulation (and SGS models for the turbulent cases under LES enclosure) and of course, efficient post processing tools. All those aspects have been analyzed and discussed in detail within the contents of this thesis.

In Chapter 2, it has been clarified that due to the complicated geometry of fin and tube heat exchangers, the recommended type of mesh for its discretization is the structured body fitted mesh. It has shown to better adjust specially to the curved surfaces and allow a smooth grow of the CV sizes at the same time. Sufficiently good results compared to the available literature data, have been found when using this kind of mesh in the present thesis. However if good mesh for the prismatic boundary layer is built, unstructured meshes can present good results at describing the flow features near curved surfaces while the rest of the mesh can be coarsened as needed and fit for more complex geometries as explained on the Chapter contents. Moreover, for the conjugated heat transfer problem it has been proved that using dimensionless parameters at the convenience of the user, physical properties for the governing equations should be readjusted in order to increase the time step for the explicit model implemented. By increasing the required time step, the global time of the simulation had been significantly reduced making a complex turbulent simulation affordable for heat exchanger applications. Also, treating the equations with such 'fictitious' physical properties, let the user to adjust the numerical behavior of the simulation leading to possible faster convergence.

Inasmuch as turbulence plays an important role on engineering flows, Chapter 3 has presented the detailed analysis of the performance of different SGS models used on a compound geometry (pin-fin matrix) similar to a heat exchanger configuration but mostly applied for gas turbine airfoil cooling purposes. It can be said that despite the coarse meshes used for LES expectations, the three models namely WALE, QR and VMS were capable to reproduce the bulk unsteady nature of the flow caused by vortex shedding downstream the pins. The simulation results were validated using experimental and numerical data found on the scientific literature and good agreement was found for the averaged values even when coarser meshes were being used. For the hydrodynamic features, WALE SGS model seemed to have a slightly better performance. Thermal field was carefully studied and quantitative and qualitative results were presented. The results showed that for the average Nusselt number at the endwalls, the three models were able to adequately predict the heat transfer, however when the same parameter was depicted locally the limitations of LES treatment using such coarse meshes were revealed. These results were published on the International Journal of Numerical Heat Transfer: Part B.

Finally, Chapter 4 was intended to include on the study different flow regimes, because on refrigeration problems laminar, turbulent and transition to turbulent flow can be distinguished even on one single device. The chapter displayed the results of a detailed CFD study on the heat transfer and hydrodynamic characteristics of the flow over plate fin and tube heat exchangers. Interesting local results have been depicted and shed some light on the behavior of the flow and its relation with the performance of this kind of devices. Local distributions of mean bulk temperature, heat transfer rate and Nusselt number were depicted which is believed to be a very important contribution to the available tools on our research group allowing the industrial problem analysis to take one step forward and give accurate point by point data of the flow physics that can be used for design and optimization purposes. As far as the author is aware, this is the first research including results to quantify the turbulence intensity for ′no-frost′ evaporators. This Chapter allowed the author also to compare results between isothermal and conjugated thermal boundary condition at the fluid-solid interfaces (fins of the heat exchanger). Even for high conductance materials on the solid domain, the temperature distribution for the conjugated heat transfer problem is not uniform at all (at least for low Reynolds number applications). From the complete qualitative and quantitative analysis represented in this Chapter, interesting understanding of the flow characteristics was acquired. The variation in space of the convective heat transfer and mean bulk temperature of the fluid was illustrated and discussed. This information led to the conclusion that depending on the requirements of the problem it might be important to take into consideration the local distribution of such parameters as a complement to the calculated mean values. The analysis of the obtained results allowed the author to show important flow structures like horseshoe vortices behind the tubes and developing regions at the leading edge of the fins.

Transversal fin length was chosen for the parametric study while the other geometric values were kept constant. The volumetric flow rate was set to be in the range of $0.25\ m/s < \dot{V} < 1.0\ m/s$ and results were presented for the different proposed configurations. It is believed that the results displayed on the present work would help the 'no-frost' refrigeration sector not only to select a better design option, but to actually understand the physics of the convoluted flow inside the evaporator device. This level of local accuracy and detailed information about the fluid-dynamic and thermal behavior can only be achieved by using this high-end simulation strategies.

Further Work

As a future work, the presence of dry and wet conditions on the heat and mass exchange should be taken into account, and the tools developed for the present thesis may be combined with new techniques to solve this complex problem. Once the developed tools have been validated, new correlations should be obtained for heat and mass transfer coefficients and pressure drop measurements. These new data will provide the research group interesting enhanced design tools for academic and industrial interests.

Moreover, different enhanced geometries can be studied with the available and in continuous update tools developed by the CTTC researchers, and new reliable information can be obtained in accordance to the necessities of the group and the industrial partners. Such local and detailed correlations will supply the low order numerical models with data in order to obtain faster and reliable results for a wide range of applications. A list of some of the possible configurations for heat exchangers suitable for the numerical tools developed by the present work could contain among others: i) wavy fins, ii) louvered fins, iii) annular fins, iv) interrupted fins, v) fins with vortex generators, vi) squared tubes, vi) oval tubes or vii) inline arrangement. Those examples are just a few to mention the possible alternatives of future work because each type of heat exchanger has different usages.

Also to take one step beyond, the study of different inlet conditions should be included. In reality inlet conditions may have some turbulence intensity and normally the inlet profiles are non uniform because of the positioning of the device and the location of the fan. On this regard, another kind of heat exchangers such as refrigerator condensers can be placed vertically. Such condition could lead to the introduction of natural or mixed convection that would require some modifications to the numerical code.